Measurement of the relative width difference of the $B^0 - \bar{B}^0$ system with the ATLAS detector

Malcolm Skinner

This thesis is submitted for the degree of Doctor of Philosophy.

· October 2016 ·

"I mean the word proof not in the sense of the lawyers, who set two half proofs equal to a whole one, but in the sense of a mathematician,where half proof = 0, and it is demanded for proof that every doubt becomes impossible."

- Johann Carl Friedrich Gauss

Acknowledgements

I would like to thank the following:

- The Science and Technology Facilities Council for funding my research.
- My supervisor Guennadi Borissov for his continual guidance and insight.
- My deputy supervisor Roger Jones for providing his assistance when needed.
- James Walder and Eva Bouhova-Thacker for the numerous hours spent helping me with my analyses.
- All of the other staff of the Lancaster University EPP group for their help and expertise.
- My family for their support, even when I didn't think I needed it.

Abstract

The measurement of the relative width difference $\Delta\Gamma_d/\Gamma_d$ of the B^0–$\bar{B}^0$ system using 25.2 fb^{-1} of integrated luminosity collected by the ATLAS detector at the LHC in pp collisions at $\sqrt{s} = 7$ TeV and $\sqrt{s} = 8$ TeV is presented. The analysis described in this thesis incorporates results previously published by the ATLAS collaboration while providing greater detail and additional studies. The measured value is $\Delta\Gamma_d/\Gamma_d = (-0.1 \pm 1.1\ (\text{stat.}) \pm 0.9\ (\text{syst.})) \times 10^{-2}$. Currently, this is the most precise single measurement of $\Delta\Gamma_d/\Gamma_d$. It agrees with the Standard Model prediction and measurements by other experiments.

Contents

List of Figures

List of Tables

Chapter 1

Introduction

The Standard Model of particle physics has shown its great quality many times since its inception. Not least in its accolades are the successful predictions of the discoveries of the W and Z bosons in 1983; the top quark in 1995; the τ neutrino in 2000; and the Higgs boson in 2012. There are, however, still a number of questions that are not yet answered by the Standard Model, such as the origin of mass and matter-antimatter asymmetry. It is therefore important to continue to study the Standard Model and there are still many ongoing studies, including those of CP violation. Detailed descriptions of the Standard Model, CP violation and B meson decays are given in chapter 2.

The design objectives of the Large Hadron Collider (LHC) can be summarized by the following two statements [1]:

- To perform high precision measurements of Standard Model parameters.
- To search for new physics beyond the limitations of the Standard Model.

Construction of the LHC began at the European Organization for Nuclear Research (CERN) in 1998 with performance goals of a nominal centre of mass energy of 14 TeV and a luminosity of $10^{-34}\text{cm}^{-2}\text{s}^{-1}$. A description of the LHC is given in chapter 3. The data used for this thesis was taken by the general purpose detector ATLAS in 2011 and 2012. ATLAS is one of seven experiments that measure the products of collisions generated by the LHC. The ATLAS detector is described in chapter 4.

A measurement of the width difference of the B^0 meson ($\Delta\Gamma_d$) can be considered as satisfying both of the given LHC objectives. The Standard model predicts a small value of $\Delta\Gamma_d$ [2] and so any new physics contribution within $\Delta\Gamma_d$ would be readily observable over the low Standard Model value. It has been demonstrated [3] that such a contribution would not contradict other existing tests of the Standard Model, even if $\Delta\Gamma_d$ is several times larger than the Standard Model value. A precise experimental measurement of $\Delta\Gamma_d$ and its comparison to to the Standard Model expectation would therefore provide a stringent test of the underlying theory [4], along with some other prominent quantities such as the branching ratio $\mathrm{Br}(B_s^0 \to \mu^+\mu^-)$ [5] or the CP violating phase of the $B_s^0 \to J/\psi\phi$ decay [6], which have attracted much more experimental and theoretical attention.

The current experimental uncertainty on $\Delta\Gamma_d$ is much larger than the SM central value, preventing a meaningful test of the Standard Model prediction. Furthermore, the measurements of $\Delta\Gamma_d$ made by the Belle [7] and LHCb [8] experiments differ between them by more than 1.5 standard deviations. Therefore, more precise measurements of $\Delta\Gamma_d$ are necessary to confirm its value and to perform a significant "null test" of the SM. A detailed description of the measurement of $\Delta\Gamma_d$ performed by the ATLAS collaboration is given in chapter 6 to chapter 9. The measurement was published in 2016 [9] and has been presented at several international conferences, including The 16th International Conference on B-Physics at Frontier Machines [10].

In addition to the measurement of $\Delta\Gamma_d$, this thesis includes a description of the techniques used by the ATLAS collaboration to measure the initial flavour of the B_s^0 meson in the analysis of the $B_s^0 \to J/\psi\phi$ decay. This description is presented in chapter 10.

Chapter 2

Theory

This chapter will introduce and explain the essential theoretical concepts needed for the measurement of $\Delta\Gamma_d$. First, the Standard Model is outlined, followed by the introduction of the CKM matrix, after which the oscillations of the B^0 meson are explained, and finally the time dependent decay rates of the B^0 meson for CP and flavour specific final states are derived.

2.1 The Standard Model

The Standard Model of particle physics is the best established description of the electromagnetic, strong and weak forces and the fundamental bosons (particles with integer spin) that mediate them. It additionally defines all of the observed fundamental fermions (particles with half-integer spin) - the constituent particles of matter. Also included in the Standard Model is the newly discovered Higgs boson, which is required to explain why certain fundamental particles are not massless.

2.1.1 Fermions

The fundamental fermions are point-like particles with spin of one half. They can be subdivided into two types: quarks and leptons. The properties of the quarks and leptons are given in tables 2.1 and 2.2 respectively.

Quarks

Quarks have an intrinsic property known as colour charge, through which they are able to interact via the strong force. Quarks exist in nature within colourless bound states called hadrons. Hadrons are classified by their quark content and can be separated into two main types: Mesons which have one valence quark and one valence antiquark; and baryons which have three valence quarks. The much rarer tetraquark, comprised of two valence quarks and two valence antiquarks, was recently observed by the LHCb collaboration [11]. Also, the combination of 4 valence quarks and one valence antiquark, known as the pentaquark, was discovered by the LHCb collaboration in 2015 [12].

There are six quarks: The down quark d, the up quark u, the strange quark s, the charm quark c, the bottom quark b and the top quark t. The down, strange and bottom quarks have an electric charge of -1/3 and the up, charm and top quarks have an electric charge of +2/3. Quarks are therefore able to interact with the electromagnetic force. Quarks are grouped in three generations: The first generation consists of the up and down quarks, the second is comprised of the strange and charm quarks and the third contains the bottom and top quarks. A quark is able to change flavour, for example $s \to u$, via the weak interaction.

Quark	Charge	Mass
d	-1/3	$4.8^{+0.5}_{-0.3}$ MeV/c^2
u	+2/3	$2.3^{+0.7}_{-0.5}$ MeV/c^2
s	-1/3	95 ± 5 MeV/c^2
c	+2/3	1.275 ± 0.025 GeV/c^2
b	-1/3	4.18 ± 0.03 GeV/c^2
t	+2/3	$173.21 \pm 0.51 \pm 0.71$ GeV/c^2

Table 2.1: Properties of the quarks [2]

Leptons

Unlike quarks, leptons exist independently. There are six fundamental leptons: The electron e^-, the muon μ^-, the tau τ^-, the electron neutrino ν_e,

the muon neutrino ν_μ and the tau neutrino ν_τ. All fundamental leptons experience interactions with the weak force, through which their flavour can change, for example $\mu \to \nu_\mu$.

The e^-, μ^- and τ^- have an electric charge of -1 and therefore undergo interactions with the electromagnetic force. Their corresponding anti-particles are the positron e^+, the anti-muon μ^+, the anti-tau τ^+, which have a charge of $+1$ but are otherwise identical to the respective leptons. The neutrinos have no electric charge and thus do not interact with the electromagnetic force. In the limit where the neutrinos are massless, the anti-neutrinos ($\bar{\nu_e}$, $\bar{\nu_\mu}$ and $\bar{\nu_\tau}$) have right handed chirality and the neutrinos have left handed chirality. In the high energy limit ($E \gg m$), the chirality of a particle is equivalent to its helicity, which is defined as the projection of a particle's spin onto its direction of momentum.

Lepton	Charge	Mass
e	-1	$0.510998928 \pm 0.000000011$ MeV/c^2
μ	-1	$105.6583715 \pm 0.0000035$ MeV/c^2
τ	-1	1776.82 ± 0.16 MeV/c^2
ν_e	0	< 2.05 eV/c^2
ν_μ	0	< 0.19 MeV/c^2
ν_τ	0	< 18.2 MeV/c^2

Table 2.2: Properties of the leptons [2]

2.1.2 Bosons

Interactions between the fermions in the Standard Model are defined by a Lagrangian, which is dependent on the local gauge symmetry of the $SU(3) \times SU(2) \times U(1)$ group. The 8 generators of the $SU(3)$ group represent the gluons g, which mediate the interactions of the strong force. Two of the generators of $SU(2)$ represent the $W^\pm$ bosons while the Z boson and the photon γ are represented by linear combinations of $SU(2)$ and $U(1)$. The $W^\pm$ and Z bosons mediate the weak force. Electromagnetism is mediated by the photon. The properties of the gauge bosons are given in table 2.3.

The gauge invariance of the Standard Model Lagrangian requires that the gauge bosons are massless. However, the consideration of a spontaneous

breakdown of the gauge symmetry of the SM Lagrangian resulted in the prediction of massive $W^{\pm}$ and Z bosons and the Higgs boson H^0 [13] [14]. The Higgs boson was discovered at the LHC in 2012 [15] [16].

Boson	Charge	Mass	Force
γ	0	$< 10^{-18}$ eV/c^2	Electromagnetism
g	0	0	Strong
$W^{\pm}$	± 1	80.385 ± 0.015 GeV/c^2	Weak
Z	0	91.1876 ± 0.0021 GeV/c^2	Weak
H^0	0	125.7 ± 0.4 GeV/c^2	

Table 2.3: Properties of the gauge bosons [2]

2.1.3 Symmetries

Charge conjugation

In quantum mechanics, the charge conjugation operator C reverses the sign of the static quantities of a particle, such as electric charge, magnetic moment, baryon number and lepton number. The dynamical quantities such as energy, momentum and helicity are not changed. Therefore, if C operates on the wavefunction of a particle, the wavefunction will be transformed to that of the anti-particle. It is important to note that this is not the case for all particles: for example, if C acts on the wavefunction of a neutrino, the chirality will not change and the resulting wavefunction will not be that of an antineutrino. Thus, charge conjugation is violated in weak interactions.

Parity

The parity operator P inverts the spatial coordinates of a wavefunction ψ: $P\psi(\boldsymbol{r}, t) = \psi(-\boldsymbol{r}, t)$. It was initially assumed that parity would be conserved in all interactions. However, an experiment was proposed by Lee and Yang and performed by Wu [17] in which ^{60}Co nuclei were oriented parallel or anti-parallel to a magnetic field, which provides the reference direction to which the emitted beta electron trajectory can be measured. Reversing the magnetic field direction (and hence the ^{60}Co alignment) is equivalent to a parity inversion. The angular distribution of the electrons was observed to

change after the magnetic field flip, which showed that parity is violated in weak interactions.

CP

With the observation that both charge conjugation and parity are violated individually, it was proposed that the combination CP would be a fundamental symmetry for all interactions, including the weak interaction [18]. However, CP violation was observed in neutral kaon decays [19], where the CP-violating decay $K_2^0 \to \pi^+\pi^-$ was measured to have a branching ratio of $(2.0 \pm 0.4) \times 10^{-4}$ relative to all charged decay modes of the K_2^0. CP violation has also been observed in the neutral B meson system [20] [21].

2.2 The CKM matrix

2.2.1 Four-quark model

Weak decays involving a $W^\pm$, known as charged current decays, are able to change quark flavour and generation. For example, the decays $u \to W^+ d$ and $u \to W^+ s$ are both seen to occur. $c \to W^+ d$ and $c \to W^+ s$ are also observed to exist. Figure 2.1 shows the charged current decay of an up type quark $u_i = u, c$ or t to a down type quark $d_j = d, s$ or b and a W^+ boson. The matrix elements that govern each of these decays are V_{ij}. Cabibbo proposed that linear combinations of the mass eigenstates d and s form weak eigenstates d' and s', as defined in Eq. 2.1, and that only the decays $u \to W^+ d'$ and $c \to W^+ s'$ are allowed [22].

$$\begin{pmatrix} d' \\ s' \end{pmatrix} = \begin{pmatrix} V_{ud} & V_{us} \\ V_{cd} & V_{cs} \end{pmatrix} \begin{pmatrix} d \\ s \end{pmatrix} \tag{2.1}$$

2.2.2 Six-quark model

Kobayashi and Maskawa identified that the quark quartet model could not explain the CP violation observed in weak interactions [23]. Although the bottom quark had not yet been discovered, they proposed a quark six-plet model in which the weak eigenstates d', s' and b' are related to the mass

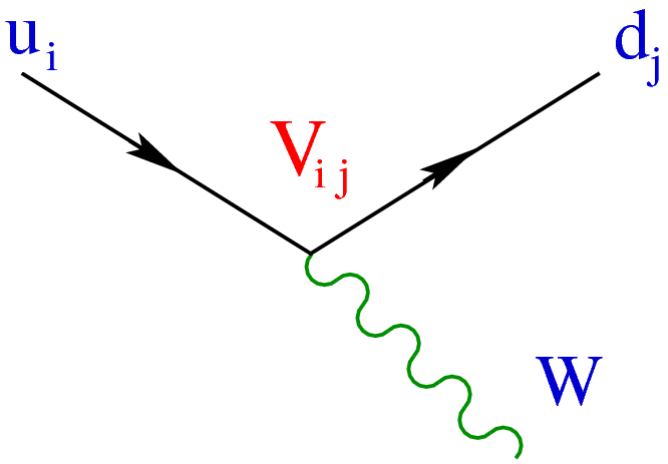

Figure 2.1: Charged current decay of an up type quark u_i to a down type quark d_j and a W^+ boson [24].

eigenstates d, s and b by a 3×3 matrix, known as the Cabibbo-Kobayashi-Maskawa (CKM) matrix:

$$\begin{pmatrix} d' \\ s' \\ b' \end{pmatrix} = \begin{pmatrix} V_{ud} & V_{us} & V_{ub} \\ V_{cd} & V_{cs} & V_{cb} \\ V_{td} & V_{ts} & V_{tb} \end{pmatrix} \begin{pmatrix} d \\ s \\ b \end{pmatrix} \tag{2.2}$$

The CKM matrix can be parameterized by three mixing angles $(\theta_{12}, \theta_{23}, \theta_{13})$ and a phase δ, with a non-zero δ representing CP violation in the Standard Model:

$$\begin{pmatrix} d' \\ s' \\ b' \end{pmatrix} = \begin{pmatrix} c_{12}c_{13} & s_{12}s_{13} & s_{13}e^{-i\delta} \\ -s_{12}c_{23} - c_{12}s_{23}s_{13}e^{i\delta} & c_{12}c_{23} - s_{12}s_{23}s_{13}e^{i\delta} & s_{23}c_{13} \\ s_{12}s_{23} - c_{12}c_{23}s_{13}e^{i\delta} & c_{12}s_{23} - s_{12}c_{23}s_{13}e^{i\delta} & c_{23}c_{13} \end{pmatrix} \begin{pmatrix} d \\ s \\ b \end{pmatrix} \tag{2.3}$$

where $c_{ij} = \cos\theta_{ij}$ and $s_{ij} = \sin\theta_{ij}$.

2.2.3 Wolfenstein parameterization

Another convenient representation of the CKM matrix is the Wolfenstein parameterization [25]. Wolfenstein noted that if $|V_{us}|$ is of order $\lambda \ll 1$ then, numerically, $|V_{cb}|$ will be of order λ^2 and $|V_{ub}|$ will be of order λ^3. The

following values are therefore assigned:

$$|V_{us}| = \lambda \tag{2.4}$$

$$|V_{cb}| = A\lambda^2 \tag{2.5}$$

$$|V_{ub}| = A\lambda^3(\rho - i\eta) \tag{2.6}$$

where A is a constant to be determined empirically and ρ and η account for the CP-violating phase.

The unitarity of the CKM matrix determines the remaining parameters to order λ^3:

$$\begin{pmatrix} d' \\ s' \\ b' \end{pmatrix} = \begin{pmatrix} 1 - \frac{1}{2}\lambda^2 & \lambda & A\lambda^3(\rho - i\eta) \\ -\lambda & 1 - \frac{1}{2}\lambda^2 & A\lambda^2 \\ 0 & -A\lambda^2 & 1 \end{pmatrix} \begin{pmatrix} d \\ s \\ b \end{pmatrix} \tag{2.7}$$

The best fit for the Wolfenstein parameters are: $\lambda = 0.22537 \pm 0.00061$, $A = 0.814^{+0.023}_{-0.024}$, $\bar{\rho} = \rho(1-\lambda^2/2) = 0.117 \pm 0.021$ and $\bar{\eta} = \eta(1-\lambda^2/2) = 0.353 \pm 0.013$ [2]. It can clearly be seen that the diagonal elements of the CKM matrix are close to one and the off-diagonal elements are much smaller. Decays that change quark generations are therefore suppressed, and decays that change two generations such as $b \to W^- u$ suffer much greater suppression that those that change a single generation such as $b \to W^- c$.

2.2.4 Unitarity relations

The CKM matrix is a unitary matrix and it therefore satisfies the following condition:

$$V^\dagger V = V V^\dagger = I_3 \tag{2.8}$$

where V is the CKM matrix, $V^\dagger$ is its Hermitian conjugate and I_3 is the 3×3 identity matrix. From the diagonal terms of this relation, weak universality is obtained:

$$\sum_j |V_{ij}|^2 = \sum_i |V_{ij}|^2 = 1 \tag{2.9}$$

where $i = u, c, t$ and $j = d, s, b$. Weak universality demonstrates that the sum of all of the couplings of the u, c or t to the d, s and b quarks are equal to one.

The off-diagonal terms of the unitarity relation result in the six orthogonality relations:

$$V_{ud}V_{cd}^* + V_{us}V_{cs}^* + V_{ub}V_{cb}^* = 0 \tag{2.10}$$

$$V_{ud}V_{td}^* + V_{us}V_{ts}^* + V_{ub}V_{tb}^* = 0 \tag{2.11}$$

$$V_{cd}V_{td}^* + V_{cs}V_{ts}^* + V_{cb}V_{tb}^* = 0 \tag{2.12}$$

$$V_{ud}V_{us}^* + V_{cd}V_{cs}^* + V_{td}V_{ts}^* = 0 \tag{2.13}$$

$$V_{ud}V_{ub}^* + V_{cd}V_{cb}^* + V_{td}V_{tb}^* = 0 \tag{2.14}$$

$$V_{us}V_{ub}^* + V_{cs}V_{cb}^* + V_{ts}V_{tb}^* = 0 \tag{2.15}$$

Each orthogonality relation can be illustrated by a *unitiary triangle* in the complex plane. The unitarity triangles all have the same area which depends on the CP-violating phase of the CKM matrix. Figure 2.2 shows the unitarity triangle produced by equation 2.14. From the Wolfenstein representation, the vertices of this triangle are $(0, 0)$, $(0, 1)$ and $(\bar{\rho}, \bar{\eta})$, and, because of its relative simplicity, it is the most widely used unitarity triangle. It is therefore oftentimes known as *The Unitarity Triangle*. The current world average

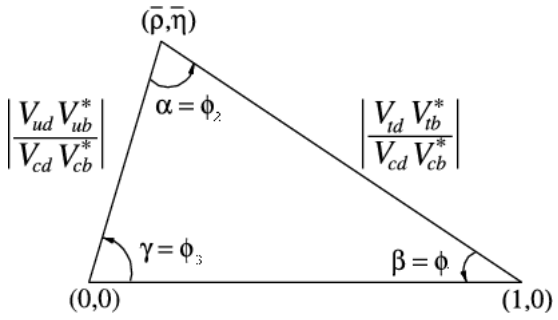

Figure 2.2: The Unitarity Triangle [2].

measurement of the angle β [6] is shown in Fig. 2.3 and is given by:

$$\sin 2\beta = 0.682 \pm 0.019 \tag{2.16}$$

Since the measured quantity is $\sin 2\beta$, there is an ambiguity because β has two possible values (β or $\frac{\pi}{2} - \beta$). This ambiguity can be resolved through the analysis of the $B^0 \to J/\psi K^{*0}$ and $B^0 \to D^{*+}D^{*-}K_S$ channels in which $\cos 2\beta$ is measured [6].

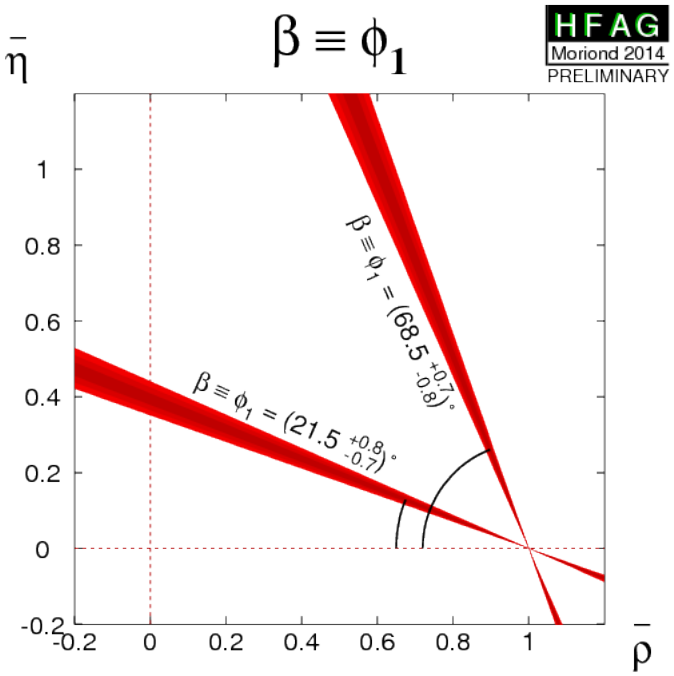

Figure 2.3: Constraints of β in the $\bar{\rho} - \bar{\eta}$ plane [6].

2.3 Oscillations of the B^0 meson

The valence composition of the B^0 meson is $\bar{b}d$. The flavour changing ability of weak interactions allows for the transition $B^0 \leftrightarrow \bar{B}^0$, where the composition of $\bar{B}^0$ is $b\bar{d}$. The Feynman diagrams for this transition is shown in Fig. 2.4.

The diagram with internal top quarks is dominant over those with internal

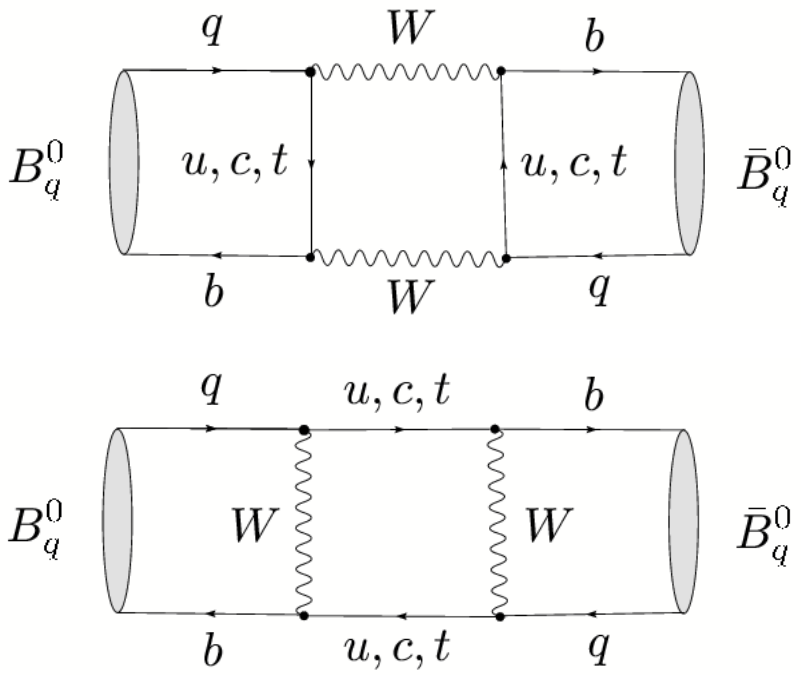

Figure 2.4: Feynman box diagrams for $B^0 \leftrightarrow \bar{B}^0$ transitions [26]. The label q represents either a u or c quark.

u or c quarks because the contribution to the transition increases with the mass of the internal quarks.

The existence of $B^0 \leftrightarrow \bar{B}^0$ transition means that B^0 and $\bar{B}^0$ are not mass eigenstates. The light and heavy mass eigenstates of the B^0 system are denoted by B_L and B_H respectively, and are linear combinations of B^0 and $\bar{B}^0$:

$$\begin{aligned} |B_L\rangle &= p\,|B^0\rangle + q\,|\bar{B}^0\rangle \\ |B_H\rangle &= p\,|B^0\rangle - q\,|\bar{B}^0\rangle \end{aligned} \tag{2.17}$$

where $|p|^2 + |q|^2 = 1$. A produced B^0 meson will therefore propagate in time as a superposition of B^0 and $\bar{B}^0$. The time evolution of B_L and B_H is given by:

$$|B_j(t)\rangle = e^{-iM_j t} e^{-\Gamma_j t/2}\,|B_j\rangle \tag{2.18}$$

where $j = L, H$ and M_j and Γ_j are ,respectively, the mass and width of B_j.

The time dependent Schrodinger equation that represents the evolution

of B^0 and $\bar{B}^0$ is

$$i\frac{d}{dt}\begin{pmatrix}|B^0(t)\rangle\\|\bar{B}^0(t)\rangle\end{pmatrix} = \mathbf{H}\begin{pmatrix}|B^0(t)\rangle\\|\bar{B}^0(t)\rangle\end{pmatrix} \tag{2.19}$$

where $\mathbf{H}$ is a 2×2 matrix which represents the $B^0 \leftrightarrow \bar{B}^0$ transition and can be written as the sum of two Hermitian matrices, $\mathbf{M}$ and $\mathbf{\Gamma}$:

$$\mathbf{H} = \mathbf{M} - \frac{i}{2}\mathbf{\Gamma} = \begin{pmatrix}M_{11} & M_{12}\\ M_{12}^* & M_{22}\end{pmatrix} + \frac{i}{2}\begin{pmatrix}\Gamma_{11} & \Gamma_{12}\\ \Gamma_{12}^* & \Gamma_{22}\end{pmatrix} \tag{2.20}$$

Inserting Eqs. 2.17 and 2.18 into 2.19 allows $\mathbf{H}$ to be diagonalized:

$$\mathbf{H'} = \mathbf{Q^{-1}HQ} = \begin{pmatrix}M_L - i\Gamma_L/2 & 0\\ 0 & M_H - i\Gamma_H/2\end{pmatrix} \tag{2.21}$$

where

$$\mathbf{Q} = \begin{pmatrix}p & p\\ q & -q\end{pmatrix} \quad \text{and} \quad \mathbf{Q^{-1}} = \frac{1}{2pq}\begin{pmatrix}q & p\\ q & -p\end{pmatrix} \tag{2.22}$$

and M_L, M_H and Γ_L, Γ_H are, respectively, the masses and widths of the light and heavy mass eigenstates of the B^0 meson. Using Eqs. 2.20, 2.21 and 2.22, the relation between p and q therefore is:

$$\left(\frac{q}{p}\right)^2 = \frac{M_{12}^* - \frac{i}{2}\Gamma_{12}^*}{M_{12} - \frac{i}{2}\Gamma_{12}} = \frac{M_{12}^*\left(1 + \frac{i}{2}\left|\frac{\Gamma_{12}}{M_{12}}\right|e^{i\phi}\right)}{M_{12}\left(1 + \frac{i}{2}\left|\frac{\Gamma_{12}}{M_{12}}\right|e^{-i\phi}\right)} \tag{2.23}$$

where the phase ϕ is given by:

$$\frac{M_{12}}{\Gamma_{12}} = \left|\frac{M_{12}}{\Gamma_{12}}\right| e^{i\phi} \tag{2.24}$$

The expression for the time evolution of B^0 and $\bar{B}^0$ is then

$$\begin{pmatrix}|B^0(t)\rangle\\|\bar{B}^0(t)\rangle\end{pmatrix} = \mathbf{Q}\begin{pmatrix}e^{-iM_Lt-\Gamma_Lt/2} & 0\\ 0 & e^{-iM_Ht-\Gamma_Ht/2}\end{pmatrix}\mathbf{Q^{-1}}\begin{pmatrix}|B^0\rangle\\|\bar{B}^0\rangle\end{pmatrix} \tag{2.25}$$

It is now useful to define the mean mass M_d and mass difference ΔM_d of the mass eigenstates, as well as the mean width Γ_d and width difference $\Delta\Gamma_d$:

$$\begin{aligned} M_d &= \frac{M_H + M_L}{2} \\ \Delta M_d &= M_H - M_L \end{aligned} \tag{2.26}$$

$$\begin{aligned} \Gamma_d &= \frac{\Gamma_L + \Gamma_H}{2} \\ \Delta \Gamma_d &= \Gamma_L - \Gamma_H \end{aligned} \tag{2.27}$$

With these definitions, the time evolution of B^0 and $\bar{B}^0$ can be expressed as:

$$\begin{pmatrix} |B^0(t)\rangle \\ |\bar{B}^0(t)\rangle \end{pmatrix} = \begin{pmatrix} g_+(t) & \frac{q}{p} g_-(t) \\ \frac{p}{q} g_-(t) & g_+(t) \end{pmatrix} \begin{pmatrix} |B^0\rangle \\ |\bar{B}^0\rangle \end{pmatrix} \tag{2.28}$$

where

$$g_+ = e^{-iM_d t} e^{-i\Gamma_d t/2} \left[\cosh \frac{\Delta\Gamma_d t}{4} \cos \frac{\Delta M_d t}{2} - i \sinh \frac{\Delta\Gamma_d t}{4} \sin \frac{\Delta M_d t}{2} \right] \tag{2.29}$$

$$g_- = e^{-iM_d t} e^{-i\Gamma_d t/2} \left[-\sinh \frac{\Delta\Gamma_d t}{4} \cos \frac{\Delta M_d t}{2} + i \cosh \frac{\Delta\Gamma_d t}{4} \sin \frac{\Delta M_d t}{2} \right] \tag{2.30}$$

2.4 Time dependent decay rate of the B^0 meson

The time dependent decay rate of a B^0 meson decaying to final state f can be defined as:

$$\Gamma(B^0(t) \to f) = \mathcal{N}_f |\langle f| \mathbf{S} |B^0(t)\rangle|^2 \tag{2.31}$$

where $\mathcal{N}_f$ is the time independent normalization and $\mathbf{S}$ is the S-matrix for the $B^0 \to f$ decay.

Using the expression for $B^0(t)$ from Eq. 2.28, $\Gamma(B^0(t) \to f)$ can be rewritten as:

$$\Gamma(B^0(t) \to f) = \mathcal{N}_f |g_+(t) A_f + g_-(t) \bar{A}_f|^2 \tag{2.32}$$

where $A_f = \langle f| \mathbf{S} |B^0\rangle$ and $\bar{A}_f = \langle f| \mathbf{S} |\bar{B}^0\rangle$.

Applying the definitions of $g_+(t)$ and $g_-(t)$ and defining

$$\lambda_f = \frac{q}{p}\frac{\bar{A}_f}{A_f} \tag{2.33}$$

yields the following equation for $\Gamma(B^0(t) \to f)$:

$$\Gamma(B^0(t) \to f) = \mathcal{N}_f |A_f|^2 e^{-\Gamma_d t}\left[\frac{1+|\lambda_f|^2}{2}\cosh\frac{\Delta\Gamma_d t}{2} + \frac{1-|\lambda_f|^2}{2}\cos\Delta M_d t - \mathrm{Re}(\lambda_f)\sinh\frac{\Delta\Gamma_d t}{2} - \mathrm{Im}(\lambda_f)\sin\Delta M_d t\right] \tag{2.34}$$

The equivalent expression for the decay $\bar{B}^0(t) \to f$ is:

$$\Gamma(\bar{B}^0(t) \to f) = \mathcal{N}_f |A_f|^2 \frac{1}{1-a} e^{-\Gamma_d t}\left[\frac{1+|\lambda_f|^2}{2}\cosh\frac{\Delta\Gamma_d t}{2} - \frac{1-|\lambda_f|^2}{2}\cos\Delta M_d t - \mathrm{Re}(\lambda_f)\sinh\frac{\Delta\Gamma_d t}{2} + \mathrm{Im}(\lambda_f)\sin\Delta M_d t\right] \tag{2.35}$$

where $a = 1 - |q/p|^2$. Using Eq. 2.23 and that $\Gamma_{12} \ll M_{12}$ such that terms $\mathcal{O}\left(\left|\frac{\Gamma_{12}}{M_{12}}\right|^2\right)$ can be neglected, a can be expressed as:

$$a = \left|\frac{\Gamma_{12}}{M_{12}}\right| \sin\phi \tag{2.36}$$

The total untagged time dependent decay rate for a B^0 meson decaying to state f is obtained by combining $\Gamma(B^0(t) \to f)$ and $\Gamma(\bar{B}^0(t) \to f)$:

$$\Gamma(f,t) \equiv \frac{\sigma(B^0)}{\sigma(B^0)+\sigma(\bar{B}^0)}\Gamma(B^0(t) \to f) + \frac{\sigma(\bar{B}^0)}{\sigma(B^0)+\sigma(\bar{B}^0)}\Gamma(\bar{B}^0(t) \to f)$$

$$\Gamma(f,t) = \mathcal{N}_f |A_f|^2 e^{-\Gamma_d t}\frac{1+|\lambda_f|^2}{2}\left[\cosh\frac{\Delta\Gamma_d t}{2} + A_{\mathrm{P}} A_{\mathrm{CP}}^{\mathrm{dir}}\cos\Delta M_d t + A_{\Delta\Gamma}\sinh\frac{\Delta\Gamma_d t}{2} + A_{\mathrm{P}} A_{\mathrm{CP}}^{\mathrm{mix}}\sin\Delta M_d t\right] + \mathcal{O}(a) \tag{2.37}$$

where

$$A_{\mathrm{CP}}^{\mathrm{dir}} = \frac{1-|\lambda_f|^2}{1+|\lambda_f|^2} \qquad A_{\Delta\Gamma} = \frac{-2\mathrm{Re}(\lambda_f)}{1+|\lambda_f|^2} \qquad A_{\mathrm{CP}}^{\mathrm{mix}} = \frac{-2\mathrm{Im}(\lambda_f)}{1+|\lambda_f|^2} \tag{2.38}$$

$$|A_{\mathrm{CP}}^{\mathrm{dir}}|^2 + |A_{\Delta\Gamma}|^2 + |A_{\mathrm{CP}}^{\mathrm{mix}}|^2 = 1 \tag{2.39}$$

$\sigma(B^0)$ and $\sigma(\bar{B}^0)$ are the respective production cross-sections for B^0 and $\bar{B}^0$ in pp collisions. The production asymmetry A_{P} of the B^0 meson is defined as:

$$A_{\mathrm{P}} = \frac{\sigma(B^0) - \sigma(\bar{B}^0)}{\sigma(B^0) + \sigma(\bar{B}^0)} \tag{2.40}$$

2.5 B^0 decaying to a CP eigenstate

If the final state f is an eigenstate of CP conjugation, the following relation is satisfied:

$$CP\,|f\rangle = \eta_f\,|f\rangle \tag{2.41}$$

where $\eta_f = \pm 1$ is the CP eigenvalue of f.

A property of a CP specific f is that $|A_f| = |\bar{A}_f|$, meaning that the decays $B^0 \to f$ and $\bar{B}^0 \to f$ have the same decay rate. An example of such a state is $J/\psi K_S$ ($\eta_f = -1$) which is shown in the Feynman diagram of Fig. 2.5.

The relation between the decay amplitudes is:

$$\frac{\bar{A}_f}{A_f} = \eta_f e^{2i\phi_f} \tag{2.42}$$

where $\phi_f = \arg(V_{cb}V_{cs}^*)$, due to the $b \to c\bar{c}s$ transition.

Equations 2.23 and 2.36 give the following expression for the ratio q/p:

$$\frac{q}{p} \approx \frac{M_{12}^*}{|M_{12}|}\Big(1 + \mathcal{O}(a)\Big) \approx e^{-i\phi_M} \tag{2.43}$$

where $\phi_M = \arg(M_{12})$. Therefore, using Eqs. 2.33, 2.42 and 2.43, for a CP specific f:

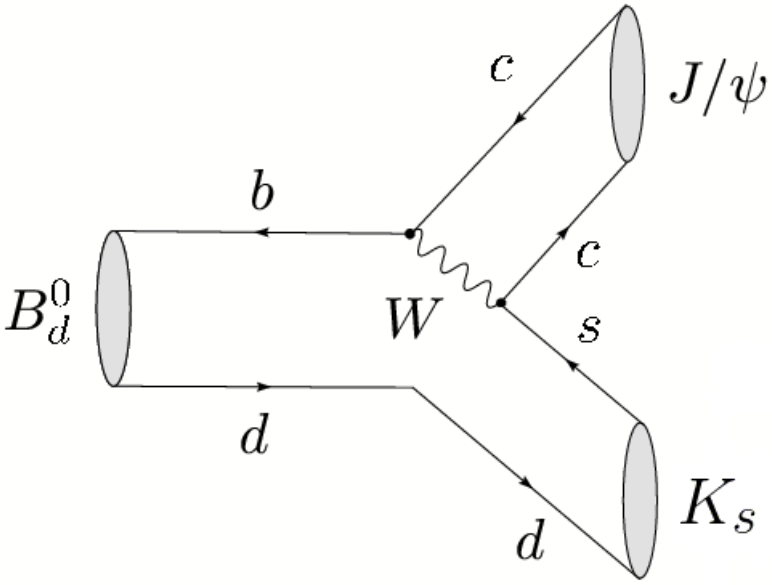

Figure 2.5: Feynman tree diagram for the $B^0 \to J/\psi K_S$ decay [26]. For the $\bar{B}^0 \to J/\psi K_S$ decay, the arrows on the fermion lines are reversed.

$$\lambda_f = \eta_f e^{-i(\phi_M - 2\phi_f)} \tag{2.44}$$

In the Wolfenstein interpretation of the CKM matrix, $\arg(V_{cb}V_{cs}^*) = \mathcal{O}(\lambda^6)$ [27] and so $\phi_M \gg \phi_f$ such that $\lambda_f \approx \eta_f e^{-i\phi_M}$. Inspecting the Feynman box diagrams in Fig. 2.4 gives the following value for ϕ_M:

$$\phi_M = \arg(V_{tb}V_{td}^*)^2 = \arg\left(\frac{V_{tb}V_{td}^*}{V_{tb}^*V_{td}}\right) = 2\beta \tag{2.45}$$

where β is the angle of the unitarity triangle shown in Fig. 2.2.

The expression for λ_f in Eq. 2.42 then reduces to:

$$\lambda_f = \eta_f e^{-2i\beta} \tag{2.46}$$

Therefore, for the decay $B^0 \to J/\psi K_S$, the values of the coefficients defined in Eq. 2.38 are:

$$A_{\mathrm{CP}}^{\mathrm{dir}} = 0 \qquad A_{\Delta\Gamma} = -\eta_f \cos 2\beta \qquad A_{\mathrm{CP}}^{\mathrm{mix}} = \eta_f \sin 2\beta \tag{2.47}$$

The untagged time dependent decay rate for the $B^0 \to J/\psi K_S$ decay is then given by:

$$\Gamma(J/\psi K_S, t) = \mathcal{N}_f |A_f|^2 e^{-\Gamma_d t} \Bigg[\cosh \frac{\Delta\Gamma_d t}{2} - \eta_f \cos 2\beta \sinh \frac{\Delta\Gamma_d t}{2} + A_{\mathrm{P}} \eta_f \sin 2\beta \sin \Delta M_d t \Bigg] \tag{2.48}$$

2.6 B^0 decaying to a flavour specific final state

For a flavour specific f, $\bar{A}_f = 0$, which means that the decay $\bar{B}^0 \to f$ does not occur. Only $B^0 \to f$ and $\bar{B}^0 \to \bar{f}$ are possible. Such a state is $J/\psi K^{*0}$ which is shown in the Feynam diagram of Fig. 2.6.

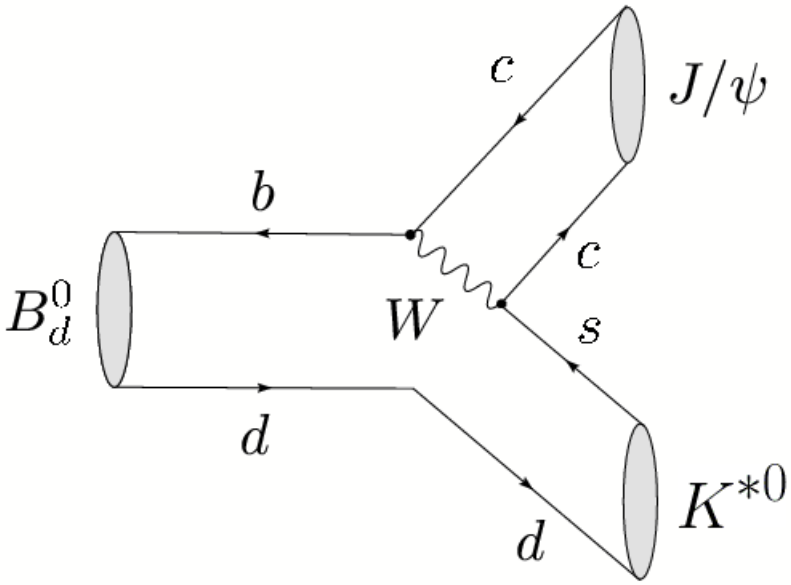

Figure 2.6: Feynman tree diagram for the $B^0 \to J/\psi K^{*0}$ decay [26]. For the $\bar{B}^0 \to J/\psi \bar{K}^{*0}$ decay, the arrows on the fermion lines are reversed.

An obvious consequence of $\bar{A}_f = 0$ is that, from its definition in Eq. 2.33, $\lambda_f = 0$. The coefficients defined in Eq. 2.38 therefore have the following values:

$$A_{\mathrm{CP}}^{\mathrm{dir}} = 1 \qquad A_{\Delta\Gamma} = 0 \qquad A_{\mathrm{CP}}^{\mathrm{mix}} = 0 \tag{2.49}$$

Accordingly, the untagged time dependent decay rate for the $B^0 \to J/\psi K^{*0}$ decay is:

$$\Gamma(J/\psi K^{*0}, t) = \mathcal{N}_f |A_f|^2 \frac{e^{-\Gamma_d t}}{2} \left[\cosh \frac{\Delta\Gamma_d t}{2} + A_{\rm P} \cos \Delta M_d t \right] \tag{2.50}$$

For the charge conjugate final state $\bar{f} = J/\psi \bar{K}^{*0}$, it follows that $A_{\bar{f}} = 0$ and $\bar{A}_{\bar{f}} = A_f$, thus:

$$\lambda_{\bar{f}} = \frac{q}{p} \frac{\bar{A}_{\bar{f}}}{A_{\bar{f}}} \to \infty \tag{2.51}$$

and the coefficients in Eq. 2.38 are therefore:

$$A_{\rm CP}^{\rm dir} = -1 \qquad A_{\Delta\Gamma} = 0 \qquad A_{\rm CP}^{\rm mix} = 0 \tag{2.52}$$

The equivalent decay rate for $\bar{B}^0 \to J/\psi \bar{K}^{*0}$ is then:

$$\Gamma(J/\psi \bar{K}^{*0}, t) = \mathcal{N}_f |A_f|^2 \frac{e^{-\Gamma_d t}}{2} \left[\cosh \frac{\Delta\Gamma_d t}{2} - A_{\rm P} \cos \Delta M_d t \right] \tag{2.53}$$

2.7 Determining $\Delta\Gamma_d/\Gamma_d$

The obtained expressions for the untagged time dependent decay rates for a B^0 decaying to $J/\psi K_S$ and $J/\psi K^{*0}(\bar{K}^{*0})$ (given by Eqs. 2.48, 2.50 (2.53) respectively) are used to determine $\Delta\Gamma_d/\Gamma_d$. The decay rate to the CP eigenstate $J/\psi K_S$ contains the $\Delta\Gamma_d$ dependence, while the decay rate to the flavour specific eigenstate $J/\psi K^{*0}$ provides normalization. By measuring the ratio of these two decay rates the factor $e^{-\Gamma_d t}$ is cancelled, which allows the value of $\Delta\Gamma_d/\Gamma_d$ to be measured precisely.

Chapter 3

The Large Hadron Collider

The Large Hadron Collider (LHC) is a dual-beam hadron accelerator and collider. It was initially approved by the CERN council in 1994 [28, 29] and construction was completed in 2008. The LHC was installed in the circular 26.7 km tunnel, originally used for LEP (Large Electron-Positron collider) , which lies between 45 m and 175 m underground near Geneva, Switzerland. The LHC is linked to the CERN accelerator complex, which provides particle injection, by two 2.5 km transfer tunnels. The geographical and schematic layouts of the LHC at CERN are shown in Figs. 3.1 and 3.2 respectively.

3.1 Performance

The principal aim of the LHC is to probe physics beyond the Standard Model using collisions with centre-of-mass energies ($\sqrt{s}$) of up to 14 TeV at a peak luminosity of $10^{34}\text{cm}^{-2}\text{s}^{-1}$. The number of events per second produced by collisions in the LHC is given by:

$$\frac{dN}{dt} = L\sigma_{Event} \tag{3.1}$$

where L is the LHC luminosity and σ_{Event} is the production cross section for the particular event under study. The luminosity is the number of particles per second that pass through a unit area of the bunch-crossing region:

$$L = f\frac{n_1 n_2}{4\pi\sigma_x\sigma_y} \tag{3.2}$$

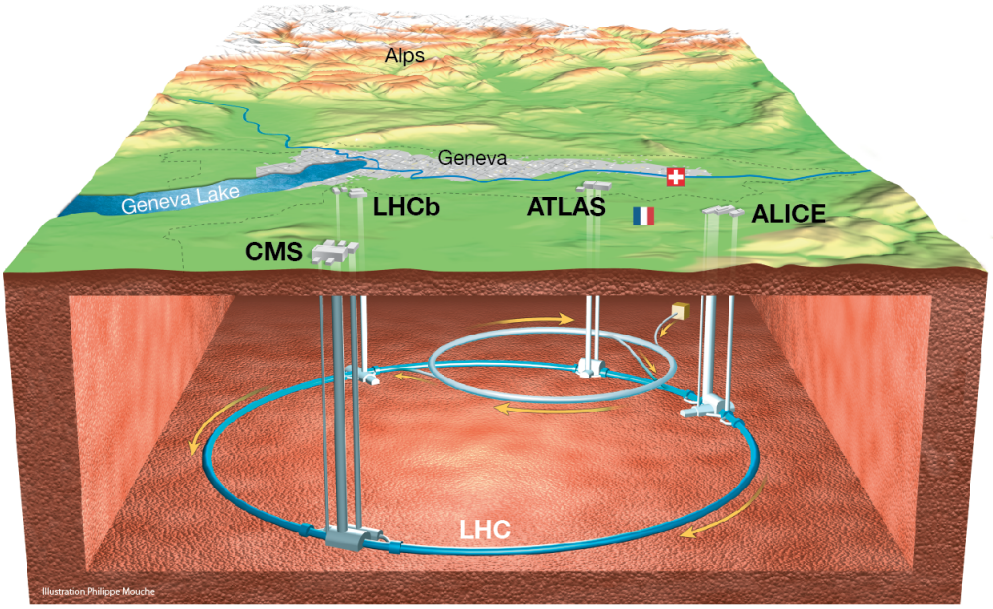

Figure 3.1: Geographic layout of the LHC at CERN [32].

where f is the bunch-crossing frequency, n_1 and n_2 are the number of particles in each bunch, σ_x and σ_y are, respectively, the horizontal and vertical beam profiles, such that the cross-sectional area of the beam is given by $4\pi\sigma_x\sigma_y$. The luminosity delivered by the LHC, as measured by the ATLAS detector, is shown in Fig. 3.3.

The integrated luminosity ($\int Ldt$) therefore signifies the total number of events that have been delivered in a given time span. The integrated luminosity is measured in units of inverse area, such as inverse femtobarns, where 1 $\text{fb}^{-1} = 10^{-43}$ m^{-2}.

The LEP/LHC tunnel has an internal diameter of 3.7 m, which is too small to contain two separate proton rings. Due to this limitation, the LHC uses twin bore magnets that consist of two beam channels contained within the same mechanical structure and cryostat. The disadvantage of this design is that the rings are magnetically coupled, which reduces beam flexibility. Other performance limitations are detailed in Refs. [28, 29] and include the following:

- Beam-beam limits.

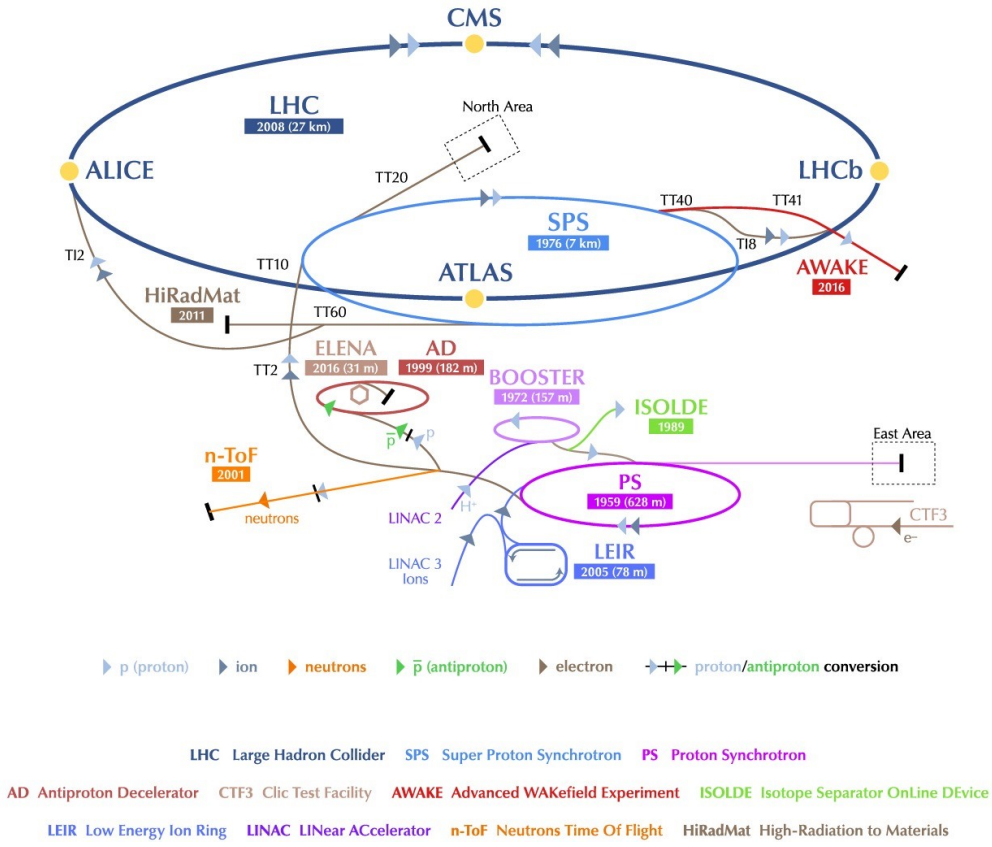

Figure 3.2: Schematic layout of the LHC accelerator complex [32].

- Mechanical aperture size.
- Maximum dipole and magnet quench limits.
- Energy stored in the circulating beams and in the magnetic fields.
- Heat load limits.
- Field quality and dynamic aperture limits.
- Collective beam instabilities.

The luminosity and centre-of-mass energy are dependent on the characteristics of the accelerator and so these performance limitations can affect them

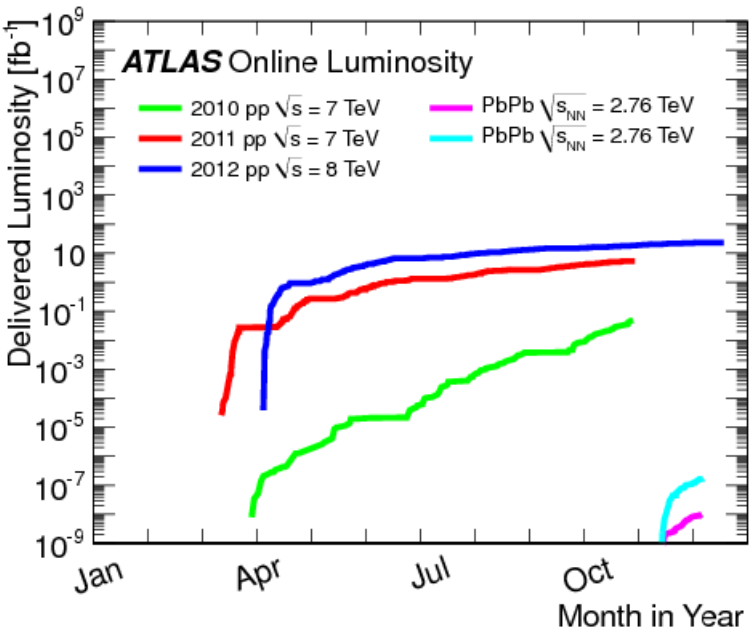

Figure 3.3: Delivered luminosity versus time for 2010, 2011, 2012 (including both p-p and Pb-Pb data), as measured by ATLAS [33].

as well as the interaction cross sections, which depend on $\sqrt{s}$, as shown in Fig. 3.4

3.2 Proton production and acceleration

The LHC proton bunches are produced by ionizing hydrogen gas using a magnetic field. The protons are then accelerated by the injector chain, which is shown in Fig. 3.2 and has four main sections:

- Linac2
- The Proton Synchrotron Booster (PSB)
- The Proton Synchrotron (PS)
- The Super Proton Synchrotron (SPS)

The proton beam is then injected into the LHC where it is captured, accelerated and stored using a superconducting cavity system that consists of:

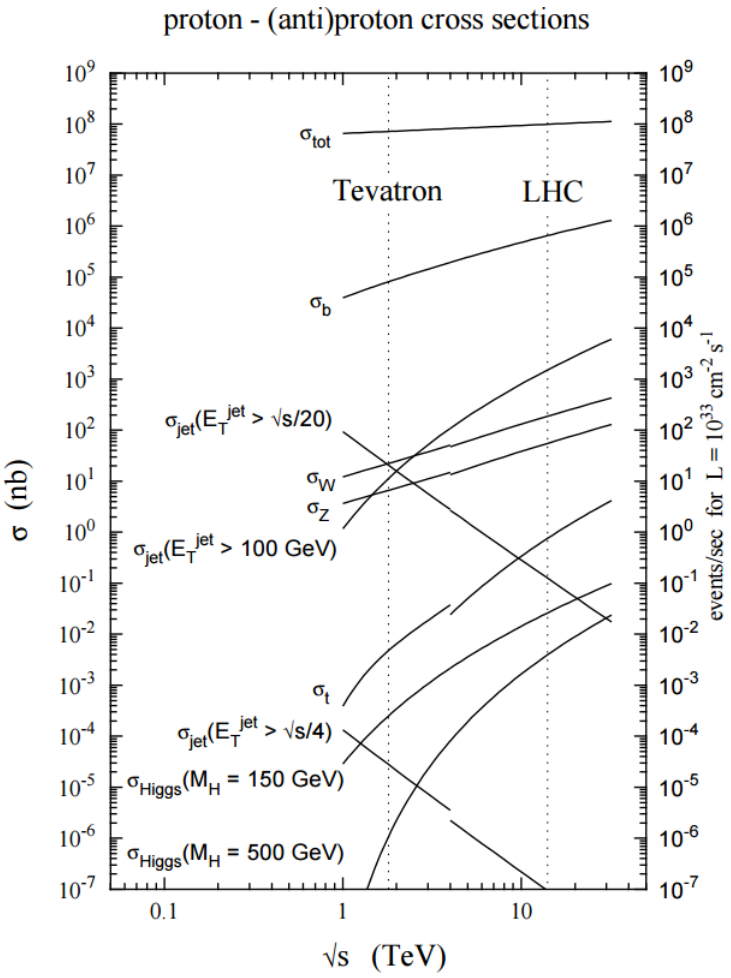

Figure 3.4: Various production cross sections for centre-of-mass energies corresponding to the LHC and the Tevatron [30].

- Radio-frequency oscillators the accelerate the proton beam.
- Dipole magnets that manoeuvre the beam into its circular path.
- Quadrupole magnets that focus the beam to maintain the size of the beam envelope.

The LHC has more than 1600 superconducting magnets in total, each of which typically weighs around 27 tonnes. The magnets are cooled to their operating temperature of 1.9K by liquid helium.

3.3 Beam properties

The high design luminosity of the LHC requires that both beams have a large number of bunches, with a high bunch crossing frequency. Nominally, the proton beams have 2808 bunches, each of which contains 1.1×10^{11} protons. The gap between bunches was 50 ns during Run 1 of the LHC, corresponding to a maximum bunch crossing frequency of 20 MHz. The beams are designed to collide an angle of $150 - 200$ μm, which reduces the number of unwanted collisions near the interaction point.

The region in which the proton-proton collisions occur is known as the "beam spot". The beam and magnet conditions of the LHC determine, to a great extent, the size, position and shape of the beam spot [31]. The transverse dimensions of the beam spot are determined by how the beams are focussed near the bunch crossing region and the spread of positions and momenta of the protons in the colliding bunches. Beam focussing is described by the β-function [31], which has a minimum value of β^*. The longitudinal size of the beam spot is determined by the length of the bunches and the angle at which the bunches collide.

In ATLAS, the beam spot is monitored continuously and is reconstructed at regular intervals using several thousand interactions collected from many events. The average size of the beam spot, measured by the ATLAS detector, for different β^* settings, in 2010, 2011 and 2012, is given in table 3.1.

Year	β^*	$\sigma_{\mathcal{L}x}(\mu\text{m})$	$\sigma_{\mathcal{L}y}(\mu\text{m})$	$\sigma_{\mathcal{L}z}(\mu\text{m})$
2010	11	48 ± 8	60 ± 12	29 ± 3
2010	2	30 ± 5	39 ± 12	36 ± 3
2010	3.5	41 ± 4	44 ± 6	63 ± 3
2011	1.5	26 ± 2	24 ± 2	57 ± 3
2011	1.0	20 ± 1	20 ± 1	56 ± 3
2012	0.6	15 ± 2	15 ± 1	48 ± 2

Table 3.1: Average size of the beam spot for different β^* settings. The errors given in the table are the RMS spread of the parameters during the corresponding time period [31].

Chapter 4

The ATLAS detector

ATLAS (A Toroidal LHC ApparatuS) is general purpose detector designed to study *pp* collisions in the LHC. The overall design requirements were defined in accordance with the physics targets for the LHC [1] and are as follows:

- A wide pseudorapidity acceptance and complete coverage of azimuthal angle.
- An inner detector with excellent momentum resolution and reconstruction efficiency for charged particles as well as vertex detectors near the interaction zone to identify secondary vertices.
- Electromagnetic calorimetry capable of identification and energy measurements of photons and electrons.
- Hadronic calorimetry which can accurately measure jet energy and missing transverse energy.
- Muon detection which is effective at both low and high momentum and is able to explicitly determine the charge of high transverse momentum muons.
- Low transverse momentum triggers with effective background rejection.

The general design of the ATLAS detector is shown in Fig. 4.1.

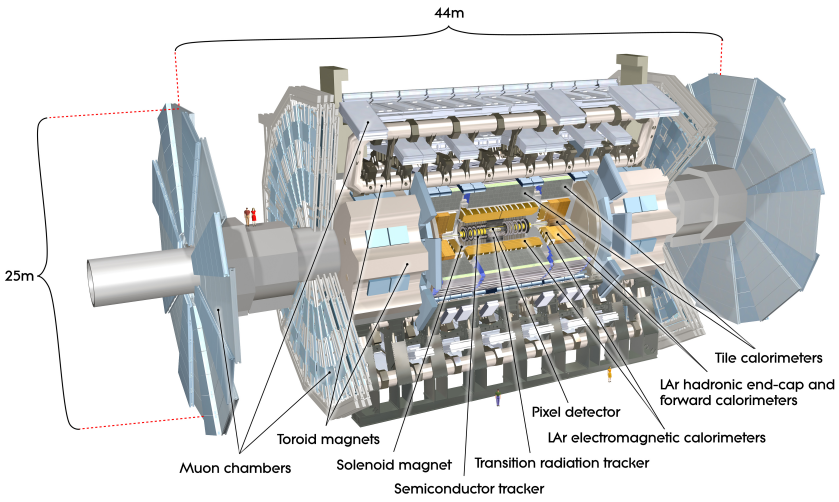

Figure 4.1: The layout of the ATLAS detector. [32].

4.1 Coordinate system

The origin of the ATLAS coordinate system is defined to be the nominal interaction point. The z-axis is defined by the beam line, the x-axis is defined to point towards the centre of the LHC ring and the y-axis is defined to point upwards, as shown in Fig. 4.2. The azimuthal angle ϕ has its usual definition of being the angle around the z-axis in the $x - y$ plane. The radial distance $R = \sqrt{x^2 + y^2}$ is the distance from the z-axis in the $x - y$ plane. The polar angle θ is defined as the angle from the z-axis in the $R - z$ plane.

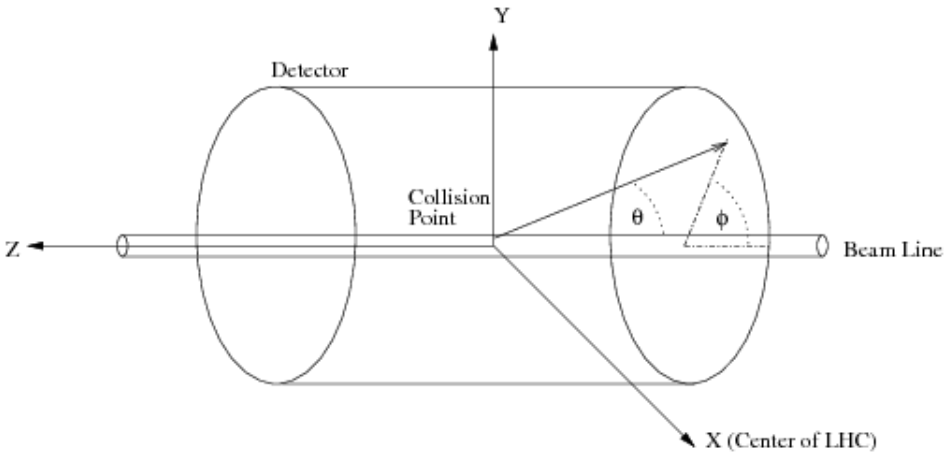

Figure 4.2: The Cartesian coordinate system of the ATLAS detector.

The pseudorapidity is defined as:

$$\eta = -\ln\left(\tan\frac{\theta}{2}\right) \tag{4.1}$$

The transverse momentum of a particle is defined as the component of its momentum in the $x-y$ plane.

4.2 Magnet system

A charged particle travelling through a magnetic field will have a curved trajectory. A measurement of the curvature allows the particle's momentum to be determined. ATLAS uses a magnet system that consists of a central solenoid, a barrel toroid and two end-cap toroids. The layout of the magnets is shown in Fig 4.3

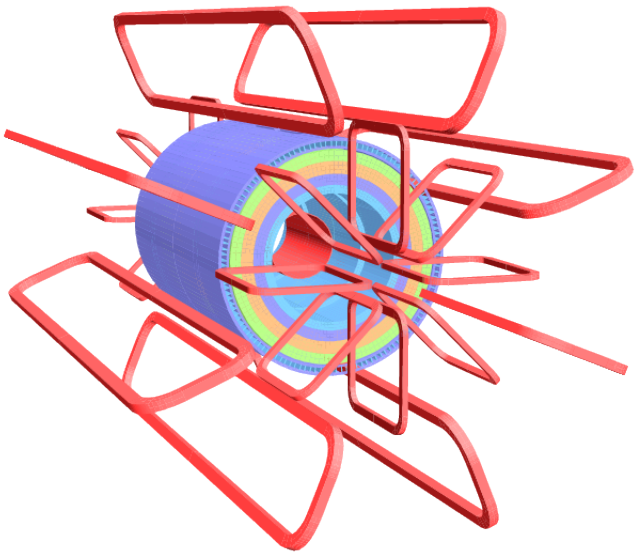

Figure 4.3: The magnet system of the ATLAS detector [1].

4.2.1 The central solenoid

The central solenoid provides an axial field of 2 T in the inner detector. It has inner and outer diameters of 2.46 m and 2.56 m, respectively, and it is 5.3 m long, with a mass of 5.7 tonnes. The physical arrangement of the solenoid was chosen to minimise the amount of material between the inner

detector and the liquid-argon calorimeter. The resulting solenoid system has a normal thickness of approximately 0.66 radiation lengths at $|\eta| = 0$.

4.2.2 The barrel toroid

The barrel toroid produces a toroidal field of 0.5 T in the central region of the muon spectrometer. It consists of eight coils arranged in a torus. Each coil is 25.3 m long and 5.4 m wide. The complete barrel toroid has an inner diameter of 9.4 m and an outer diameter of 25.3 m. It has a total mass of 830 tonnes.

4.2.3 The end-cap toroids

The end-cap toroids provide a toroidal field of 1T in the end-cap region of the muon spectrometer. Each is a single cold mass of 240 tonnes comprised of eight square coils.

4.3 Beam pipe

The ATLAS beam pipe is 38m long and is made from seven pipes which are bolted together such that an ultra-high vacuum system is obtained. The central of the seven pipes is composed of 0.8 mm beryllium and has an inner diameter of 58 mm. It is positioned with its centre on the nominal interaction point and is combined with the inner pixel detector. Beryllium is used here because its low radiation length means that high energy particles are not likely to interact with the pipe, which reduces the chances of multiple scattering. The remaining six pipes are composed of stainless steel and are placed symmetrically on both sides of the central beryllium pipe.

4.4 Inner detector

The purpose of the ATLAS inner detector is to provide high quality momentum resolution and measurements of primary and secondary vertices for charged tracks which have pseudorapidity $|\eta| < 2.5$. The inner detector cylinder is shown in Fig. 4.4. It is 7 m long and has a radius of 1.15 m.

The inner detector contains three complementary sub-detectors which are detailed in the following sections. The dimensions and properties of the sub-detectors are given in tables 4.1 and 4.2. The innermost sub-detector is the pixel detector, followed by the semiconductor tracker (SCT), and the transition radiation tracker (TRT).

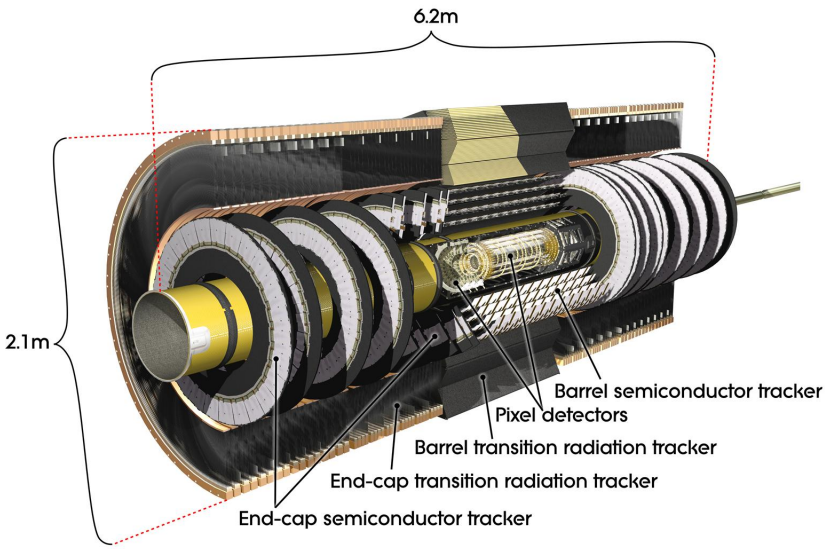

Figure 4.4: The layout of the ATLAS inner detector. [32].

4.4.1 Pixel detector

The pixel detector is formed by 80.4 million identical channels, each of which has an area of 50×400 μm^2 in $R-\phi \times z$, which provides high granularity near the vertex region. The pixel layers are positioned in the $R-\phi$ plane along the z-axis such that each charged track will usually cross three pixel layers. There are three layers in the barrel and four in the end-caps. The barrel section covers the range $0 < |\eta| < 1.7$ and the end-caps provide coverage for $1.7 < |\eta| < 2.5$ The intrinsic resolution of the pixel detector in the barrel is 10 μm in $R-\phi$ and 115 μm in z. In the end-caps, the resolution is 10 μm in $R-\phi$ and 115 μm in R.

Item		Radial Extension (mm)	Length (mm)
Overall		$0 < R < 1150$	$0 < \|z\| < 3512$
Beam-pipe		$29 < R < 36$	
Pixel	Overall envelope	$45.5 < R < 242$	$0 < \|z\| < 3092$
3 cylindrical layers	Sensitive barrel	$50.5 < R < 122.5$	$0 < \|z\| < 400.5$
2×3 disks	Sensitive end-cap	$88.8 < R < 149.6$	$495 < \|z\| < 650$
SCT	Overall envelope	$255 < R < 549$ (barrel)	$0 < \|z\| < 805$
		$251 < R < 610$ (end-cap)	$810 < \|z\| < 2797$
4 cylindrical layers	Sensitive barrel	$299 < R < 514$	$0 < \|z\| < 749$
2×9 disks	Sensitive end-cap	$275 < R < 560$	$839 < \|z\| < 2735$
TRT	Overall envelope	$554 < R < 1082$ (barrel)	$0 < \|z\| < 780$
		$617 < R < 1106$ (end-cap)	$827 < \|z\| < 2744$
73 straw planes	Sensitive barrel	$563 < R < 1066$	$0 < \|z\| < 712$
160 straw planes	Sensitive end-cap	$644 < R < 1004$	$848 < \|z\| < 2710$

Table 4.1: Dimensions of the inner sub-detectors [1]

4.4.2 Semiconductor Tracker (SCT)

There are 6.3 million readout channels of the SCT, which have a total surface area of 61 m^2. The barrel region of the SCT is made up of stereo strips that have an angular size of 40 mrad. These strips are used to measure both the $R - \phi$ and z coordinates. The barrel SCT covers the range $0 < |\eta| < 1.4$. Each module in the barrel SCT has intrinsic resolutions of 17 μm in $R - \phi$ and 580 μm in z. The SCT end-cap section has two sets of stereo strips: one that runs radially and one that runs an angle of 40 mrad. The sets of strips have a mean pitch of 80 μm. The pseudorapidity coverage of the SCT end-caps is $1.1 < |\eta| < 2.5$. The modules in the SCT end-caps have intrinsic resolutions of 17 μm in $R - \phi$ and 580 μm in R. Each track should interact with eight of the SCT strip layers, which corresponds to four spatial points.

4.4.3 Transition Radiation Tracker (TRT)

The TRT has approximately 351,000 readout channels and provides many more hits than the pixels or SCT: typically 36 per track. It consists of straw tubes of 4 mm diameter, which are positioned parallel to the beam axis in the

System	Position	Area (m^2)	Resolution $\sigma(\mu m)$	Channels (10^6)	$\lvert\eta\rvert$ coverage
Pixels	B layer	0.2	$R\phi = 12, z = 66$	16	2.5
	Other 2 barrel layers	1.4	$R\phi = 12, z = 66$	81	1.7
	4 end-cap disks	0.7	$R\phi = 12, z = 77$	43	$1.7 - 2.5$
SCT	4 barrel layers	34.4	$R\phi = 16, z = 580$	3.2	1.4
	9 end-cap wheels	26.7	$R\phi = 16, z = 580$	3.0	$1.4 - 2.5$
TRT	Axial barrel straws		170 per straw	0.1	0.7
	Radial end-cap straws		170 per straw	0.32	$0.7 - 2.5$

Table 4.2: Properties of the inner sub-detectors [1]

barrel and have a length of 144 cm. In the end-caps, the tubes are in a radial wheel arrangement and are 37 cm long. The TRT provides a pseudorapidity coverage of $0 < |\eta| < 2.0$.

Each straw tube houses a tungsten wire of 31μm diameter that is plated with gold. The 70% Xe, 27% CO_2, 3% O_2 gas mixture that fills the remaining volume is contained by the tube walls, which are comprised of two 35 μm multi-layer films. The tubes have a typical electron collection time of 48 ns and an intrinsic resolution of 130 μm in $R - \phi$, which is the only direction for which the TRT contributes.

4.5 Calorimetry

Figure 4.5 shows the calorimetry system the ATLAS detector. It consists of two main sub-systems:

- The electromagnetic calorimeter, which has fine granularity appropriate for measuring the energy and momentum of electrons and photons with high precision.

- The hadronic calorimeter, which has coarser granularity suitable for jet construction and measurements of missing transverse energy.

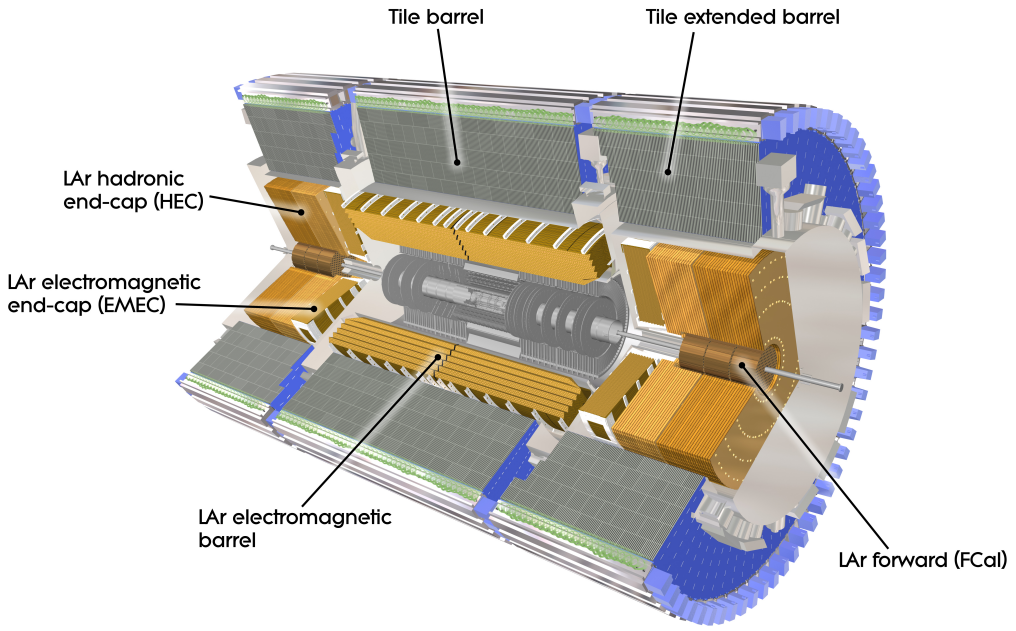

Figure 4.5: The layout of the ATLAS calorimetry system. [32].

4.5.1 The LAr electromagnetic calorimeter

Liquid Argon is used as the active sampling material in the EM calorimeter and lead plates are used as the absorber. The barrel part of the EM calorimeter covers the pseudorapidity range $0 < |\eta| < 1.475$. It is made of two identical half-barrels that are separated by a 4 mm gap at $z = 0$. The accordion geometry of the barrel section provides full coverage and isotropy in ϕ. The end-caps have outer and inner coaxial wheels which provide coverage for $1.375 < |\eta| < 2.5$ and $2.5 < |\eta| < 3.2$ respectively. The barrel and outer wheel end-cap sections are used for high precision physics analyses and thus have finer lateral granularity than the inner wheel end-caps. The depth of the EM calorimeter must be sufficient to contain electromagnetic showers and limit the number of stray particles that enter the muon system. To this end, the EM calorimeter is more than 22 radiation lengths ($X_0 = 140$ mm [2]) thick in the barrel region and is greater than 24 X_0 in the end-caps.

4.5.2 The hadronic calorimeter

The hadronic calorimeter is divided into three separate parts which can be seen in Fig. 4.5.

First, the tile calorimeter which uses scintillating tiles as the active sampling material and steel as the absorber. It has a barrel that covers the pseudorapidity range $0 < |\eta| < 1.0$ and two extended barrels that cover $0.8 < |\eta| < 1.7$. The barrel and extended barrels each have 64 modules which are positioned azimuthally. The tile calorimeter has a total thickness of 9.7 interaction lengths ($\lambda = 204$ mm for pions [2]) at $\eta = 0$ which provides sufficient containment for hadronic showers and good resolution of hadronic jets.

Second, the Hadronic End-cap Calorimeter (HEC) which has two independent wheels in each end-cap that are positioned directly behind the end-cap wheels of the EM calorimeter. It uses copper plates as the absorbing material which are interleaved with 8.5 mm gaps within the liquid Argon cryostat, which it shares with the EM calorimeter end-caps. The HEC covers the range $1.5 < |\eta| < 3.2$ and therefore intentionally overlaps the tile and forward calorimeters to ensure that there is sufficient material density in the transition regions.

Third, the Forward Calorimeter (FCal) is incorporated in the end-cap liquid Argon cryostats. It helps to provide uniform calorimetric coverage and reduce background radiation in the muon system. The FCal has three modules in each end-cap, each of which contains a metal matrix that has gaps for the liquid Argon sampling material. The first module is designed for electromagnetic measurements and uses copper for its metal matrix. The remaining two modules are optimized for hadronic measurements and use tungsten. The FCal provides coverage for $3.1 < |\eta| < 4.9$ and has a total thickness of 10λ.

4.6 Muon system

High energy muons are indicative of B meson decays, which makes good muon detection essential for the study of the B^0 width difference. Muons are highly penetrative and thus are not absorbed in the calorimeters. A dedicated muon

detector is therefore needed. Figure 4.6 shows a schematic of the ATLAS muon system. The muon system measures the momentum of muons through

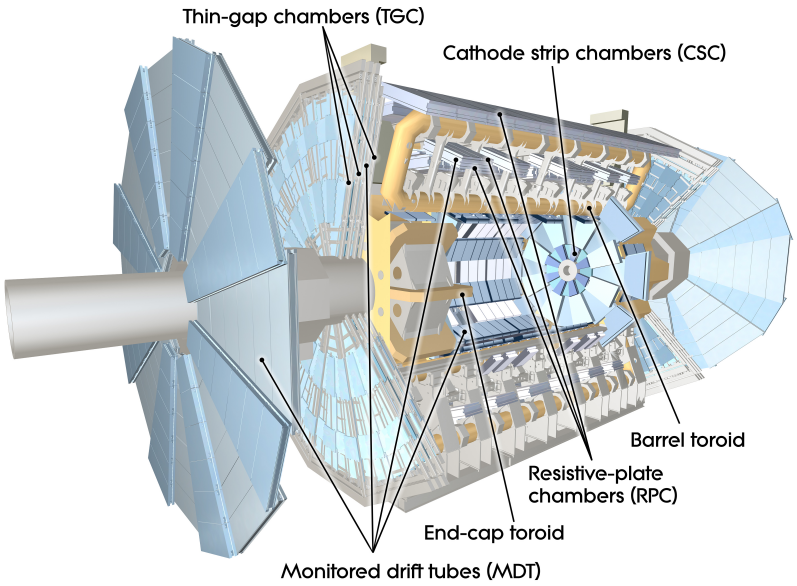

Figure 4.6: The layout of the ATLAS muon system. [32].

the use of large superconducting air-core toroid magnets, which bend the muon tracks. The large barrel toroid provides magnetic deflection for the pseudorapidity range $0 < |\eta| < 1.4$ and coverage for $1.6 < |\eta| < 2.7$ is provided by two end-cap magnets. The transition region $1.4 < |\eta| < 1.6$ is covered by a combination of the barrel toroid and the end-cap magnets.

Monitored Drift Tubes (MDT's) provide high precision measurements of the muon tracks for the majority of the pseudorapidity range. The MDT's are composed of a 50μm diameter Tungsten-Rhenium wire contained within a 30 mm diameter Aluminium tube. The gas inside the tubes is a mixture of Argon and CO_2. The MDT's in the barrel region are laid out in three cylindrical layers. In the end-caps the MDT's are positioned in three planar layers perpendicular to the beam.

Cathode Strip Chambers (CSC's) are used in the high pseudorapidity region ($2 < |\eta| < 2.7$) as they are able to cope with the extreme rate and background environment. CSC's are multiwire proportional chambers divided into three strips and thus have much finer granularity that the MDT's.

The muon detector also has a trigger system which has three main pur-

poses:

- To provide bunch-crossing identification.
- To provide precise transverse momentum thresholds.
- To measure the coordinate of muon tracks complementary to the coordinate measured by the high precision tracking chambers.

The barrel section of the muon trigger system covers the range $0 < |\eta| < 1.05$ and consists of Resistive Plate Chambers (RPC's). The end-cap sections cover $1.05 < |\eta| < 2.4$ and use Thin Gap Chambers.

4.7 Trigger system

The LHC produces a $p-p$ bunch crossing every 25 ns, which is an event rate of 40 MHz. A typical event has a size of 1.3 Mbytes and so storing anywhere close to the full number of events would be completely infeasible. To reduce the event rate to a manageable level, the ATLAS trigger system must have an event rejection factor of order 10^5 but the number of important physics events that are discarded should be minimized. To this end, the trigger system is separated into three subsequent levels. Each level improves on the choices made by the previous level and applies any further selection cuts that are needed. Figure 4.7 shows a diagram representing the ATLAS trigger system.

The first trigger level (L1) uses information from a subset of the ATLAS detectors. The trigger system of the muon detector selects high energy muons. Selections are also made by 7000 reduced granularity towers in the electromagnetic and hadronic calorimeters, each of which covers approximately 0.1×0.1 in $\Delta\eta \times \Delta\phi$. This allows Regions of Interest (RoI's) in $\eta \times \phi$ to be defined, which are passed on to the next trigger level. The L1 trigger reduces the event rate to approximately 75 kHz.

The second trigger level (L2) analyses the RoI's, defined by the L1 trigger, using the full granularity and precision of the calorimeters, the muon system and the inner detector. The selections performed by the L2 trigger reduce the event rate to approximately 3.5 kHz.

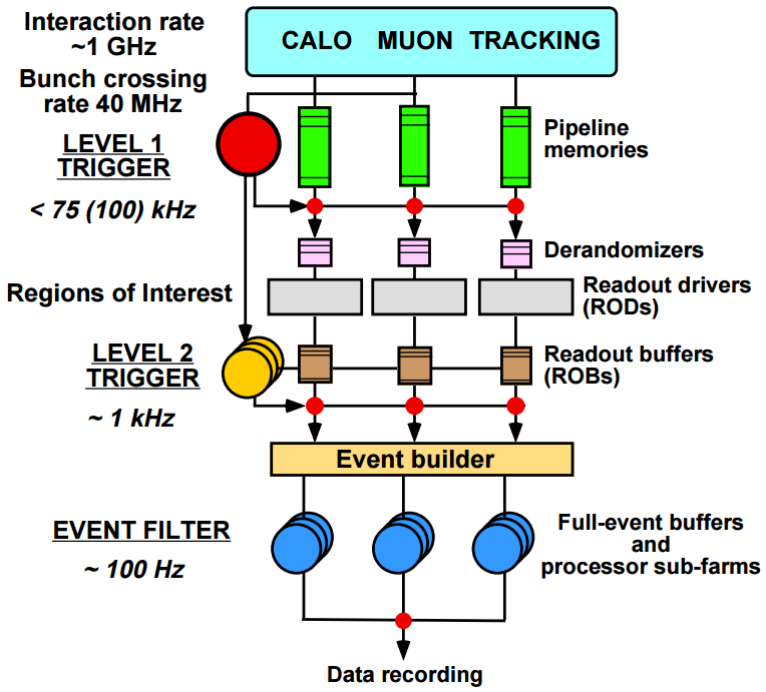

Figure 4.7: Diagram of the ATLAS trigger system [34].

The third trigger level, known as the event filter (EF), applies topological selections to events that are sent from the L2 trigger. The EF also organizes the events using a given assortment of event streams. Events that pass the topological selections are sent to output nodes and are stored in a local file system based on which stream the events are sorted into. The EF reduces the event rate to its final value of 200 Hz.

4.7.1 B-physics trigger system

The goal of the B-physics trigger system is to distinguish the decay channels of B hadrons, such as $B^0 \to J/\psi K_S$ and $B^0 \to J/\psi K^{*0}$, from the vast $b\bar{b}$ background.

The main triggers used for these channels are the di-muon triggers, which require two muons coming from a common vertex at L1, with a transverse momentum threshold of 4 or 6 GeV. The L2 trigger then attempts to eliminate muons from π and K decays using the precision of the inner detector. The EF performs a more precise fit of the muon tracks and applies invariant mass selection cuts.

Other useful triggers for B-physics channels are the single muon triggers. At L1, these triggers have various transverse momentum thresholds for the required muon in the muon trigger system. There should also be a corresponding RoI in the electromagnetic and hadronic calorimeters. The L2 trigger and the EF then use information from the inner detector to reconstruct the muon track within the RoI.

Of course, the di-muon triggers are much more effective at identifying $J/\psi \to \mu^+\mu^-$ decays, which is why they are the principal triggers used for the $B^0 \to J/\psi K_S$ and $B^0 \to J/\psi K^{*0}$ channels.

Chapter 5

ATLAS computing and software

The ATLAS computing model must be able to manage the $\mathcal{O}(10PB)$ of information in the RAW data collected by the ATLAS detector each year [35] and provide proper data access to collaboration members all around the world. To achieve this, ATLAS makes use of a variety of event data formats which are detailed in Section 5.1. ATLAS also employs a Computational Grid [36] which allows the computing assets to be distributed to and shared by the off-site resources of the institutions in the collaboration. Section 5.2 describes the Computational Grid used by ATLAS.

Simulated Monte Carlo data of ATLAS events must be produced and provided to the collaboration, in a similar way to real data. Monte Carlo data is created using a well-defined chain of independent processes. The simulation full chain is described in Section 5.3. Section 5.4 explains how the raw output from the detector or the simulation chain is converted into usable physics information. Physics analyses utilize this information through the procedure described in Section 5.5.

5.1 Data types

To cope with the extremely large volume of data, ATLAS employs a number of different data formats. The various data types have distinct purposes and their size varies such that they contain all of the information required

for their task, but they must not be unnecessarily large. The following list details the data types used by ATLAS:

- **RAW data** consists of events directly produced by the Event Filter. The events are expected to have a size of 1.6 MB and an output rate of 200 Hz. The event filter produces events in "byte-stream" format, which is similar to the format delivered by the detector, and so is not an object-oriented representation. Each RAW data file contains events corresponding to a single run of data taking. However, the events will be unordered. A typical RAW data file has a size of 2 GB.

- **Event Summary Data (ESD)** is produced from the RAW data and the full output of the detector reconstruction. The information held by ESD allows algorithms for particle identification, track re-fitting and jet reconstruction to be run and calibrated. ESD events have a typical size of 500 kB.

- **Analysis Object Data (AOD)** contains a more concise version of the reconstructed events, which should be sufficient for most analyses. AOD can be produced using ESD which eliminates the need to reprocess RAW data, increasing efficiency. Events in the AOD format are typically 100 kB in size.

- **Derived Physics Data (DPD)** contains event data presented in the style of a ntuple. Users utilize this format to analyse and histogram data via standard analysis tools such as ROOT [37]. ROOT is an object oriented framework designed for large scale physics data analysis, written in C++. It provides tools for advanced statistical analysis including histogramming, fitting and minimization. There are several different DPD sub-types whose details and purpose are dependent on the requirements of the physics working groups that utilize them.

- **Simulated Data (SIM)** is produced by the simulation chain described in Section 5.3. Simulated Data refers to a variety of data that can be RAW data or DPD or anywhere in between. Simulated Data also contains Monte Carlo truth information about events, which increases file size, often exceeding that of RAW data.

5.2 The Computational Grid

The LHC Computational Grid, henceforth referred to as the Grid, is a worldwide collaboration consisting of hundreds of computing sites distributed throughout dozens of countries. The computing sites are separated into three tiers:

- Tier-0 is responsible for the primary event processing and is based at CERN and an expansion site in Budapest, Hungary. Tier-0 provides reconstruction of primary RAW data which is then archived and distributed to Tier-1 sites.

- Tier-1 is responsible for long term storage of RAW data and providing access to it. ATLAS is served by about ten Tier-1 sites, each of which accounts for an approximately equal share of the data. The Tier-1 sites must facilitate access and analysis of the data they host in order to provide some of the calibration processing capacity.

- Tier-2 sites are plentiful and provide a number of different functions in ATLAS such as calibration, simulation and analysis facilities for physics working groups and subgroups. Each Tier-2 site is associated to a Tier-1 site to form a cloud, which usually consist of the sites from a single country.

- Tier-3 sites are local resources, usually used within a single institution. They are able to submit and retrieve jobs from the Grid and are generally used by an institution to proceed with work "off the Grid".

Data stored on the Grid can be accessed using the software DQ2 [38], which is a series of Python tools used by ATLAS to copy, move or delete data files. A typical ATLAS member will use DQ2 to find and obtain data sets required for their analysis via elementary commands such as `dq2-ls` or `dq2-get`. Although DQ2 was used for the analyses described in this thesis, it has now been replaced by Rucio [39].

Data sets can also be searched for using the ATLAS metadata interface (AMI), which is essentially a web based version of DQ2. AMI provides a more user-friendly interface for accessing useful information about a data

set, such as the number of events, the geometry version used in the event reconstruction and the Monte Carlo version, if applicable.

ATLAS Grid users can submit jobs to the Grid through the Ganga [40] or PanDA [41] interfaces. These methods of job submission allow analysis code to be sent to the data sets such that large, cumbersome files do not have to be downloaded to the user's local computer. Furthermore, the submitted jobs can be divided and distributed among the extensive number of Grid sites, reducing the time needed to run the job.

5.3 The simulation full chain

Simulated Monte Carlo data is produced via a series of processes known as the full chain. An overview of the steps of the full chain is shown in Fig. 5.1. The main steps of the chain will be detailed in this section based on information from Ref. [42]. The chain outputs Raw Data Objects (RDOs), which are equivalent to the output of the ATLAS detector. This allows the same reconstruction algorithms to be applied to both real and simulated data. The full chain is implemented using the ATLAS software framework, Athena, which is also used for the processing of ATLAS data.

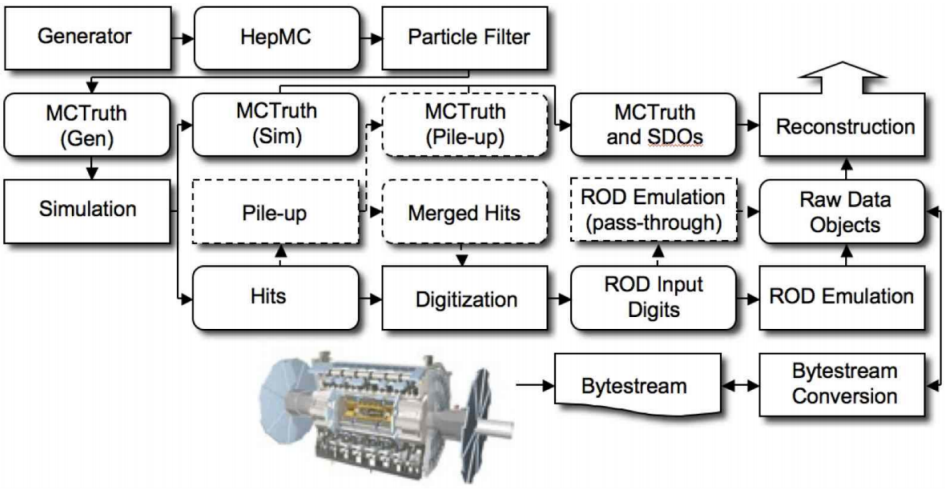

Figure 5.1: Overview of the ATLAS simulation full chain. [42].

5.3.1 The Athena framework

Athena is based on Gaudi [43], which is an adaptable C++ framework, developed originally by the LHCb collaboration, designed for physics data processing. Athena is an enhanced version of Gaudi that consists of algorithms and tools written in C++ which are configured and loaded by Python scripts known as "job options".

One of the major design principles of Athena is that data and algorithms should be clearly separated. This means that the complex algorithmic code responsible for building the components of event data, such as tracks and vertices, is separated from the interface that allows access to the physical variables describing such components. The benefit of this principle is that users analysing physics objects are not reliant on the algorithms that produced those objects. Moreover, upgrades or modifications made to a particular Athena algorithm are less likely to affect physics users' specialized analysis code.

Athena has many different versions, known as releases, which are divided into major projects based on their functionality. The entirety of the ATLAS simulation software is contained in a single project. The "simulation" project has two main dependencies. The first is the"core" project which contains the Athena framework and projects used for the description of the ATLAS detector, which are named "conditions" and "detector description". The second dependency is the "event" project which describes persistent objects.

5.3.2 Generation

The first step of the simulation full chain is event generation. Here, a set of simulated particles is produced using, in ATLAS, the modelled interaction of two partons from a proton-proton collision. The generated event includes the hadronization and decays of the produced particles. It does not contain the interaction between the particles and the detector: this is done at a later stage.

The software used for event generation are known as "generators". Most generators are developed externally to ATLAS, but are still used within the Athena framework. The most relevant generators are Pythia [44] and its AT-

LAS variant PythiaB [45], used for generating events containing B hadrons, which are written in FORTRAN; and the newer generators Pythia 8 [46] and Pythia 8B, written in C++.

PythiaB

The production probability of a $b\bar{b}$ pair in a proton-proton collision is approximately 1%, which makes the generation of such events (required for the measurement of $\Delta\Gamma_d$) using Pythia alone very inefficient.

PythiaB was therefore developed by ATLAS to reduce the processing time needed to generate B hadron events in the numbers required for B physics analyses. This is achieved by interrupting each event generation just after the parton interaction, before any hadronization, to check if a $b\bar{b}$ pair is present. If found, the simulated hadronization of the same $b\bar{b}$ pair can be repeated independently many times (the number of repetitions is defined by the user) to efficiently produce a sizable sample of generated events. Typically, the b quark is required to decay to a specified decay channel of interest, while the $\bar{b}$ quark decays freely, although the opposite can also be done.

5.3.3 Simulation

Once the generation stage is completed, the generated events are sent to the next step in the chain known as "simulation". Before simulation begins, selection cuts (such as p_T or η requirements) can be applied to the generated events to remove any unneeded particles. The particles are then passed through a full simulation of the ATLAS detector using the Geant4 toolkit [47], which provides a framework for performing detector simulation. Geant4 has an extensive range of capabilities including the description of the detector geometry, the propagation of particles through the detector, and the modelling of physics processes within the detector, such as ionization and multiple scattering. These capabilities allow Geant4 to produce simulated trajectories of the particles in an event, which are compared to the position of the sensitive regions of the detector. The energies deposited by the particles in these regions are recorded as "hits", which contain the position, time and amount of energy deposited. The output of the simulation stage is a file

containing the hits of the simulated events.

5.3.4 Truth information

The generation and simulation stages produce a history of the generated particles and interactions, and of the particle tracks and decays, respectively. This is known as the "truth" information. A comparison of the truth information to the fully reconstructed Monte Carlo output can be used to ensure that the output sample only contains signal events. Additionally, detector efficiencies and resolutions can be determined from the difference between the reconstructed output information and the truth.

5.3.5 Pile-up

The hits file from the simulation step contains a record of the particle interactions from each generated signal event. However, at the high luminosity of the LHC, there are multiple $p-p$ interactions at each beam crossing such that each signal event is accompanied by several background events, known as pile-up. The number of simulated pile-up events is defined as a function of the simulated luminosity. They usually consist of several event types such as minimum-bias, cavern background, beam gas and beam halo. The pile-up events are read in and overlaid with the signal event. Pile-up is an optional stage in the full chain and so not all hits files contain pile-up information.

The signal plus pile-up events are contained within an event collection and each event is assigned a numerical index called the generated event number. Later stages of the full chain rely on the signal event being the first in the event collection (index 0). Checks were therefore emplaced to ensure that the signal event is indeed the first, without which some of the branches of the Monte Carlo AODs and DPDs could be incomplete or empty.

5.3.6 Digitization

The digitization stage of the full chain is where the hits produced by simulation, with or without pile-up, are converted into the output format actually produced by the ATLAS detector. The hits are turned into detector responses known as "digits".

Each subdetector has its own digitization package which accounts for the different characteristics of the separate detector subsystems and allows digitization to be implemented modularly. There is an additional top-level digitization package which coordinates all of the digitization packages and ensures that they are configured consistently. The digitization algorithms are tuned to reproduce the detector response observed in tests of the real detector. The digits produced by the subdetector packages are written out as RDOs.

5.4 Reconstruction

Reconstruction is where the raw data, from the detector or digitization, is translated into recognizable physics objects such as vertices, tracks and jets. The information from all of the subdetectors is combined into algorithms to provide optimal reconstruction of the particle parameters. The physics information output by reconstruction defines the content of the ESD.

Reconstruction also provides particle identification for photons, electrons, muons and tau-leptons. In the case of muon identification, the algorithm uses information from the inner detector and the muon system to produce combined muon tracks. This kind of muon identification is employed by many B-physics analyses.

Additional optimization and validation of the reconstruction algorithms is performed using Monte Carlo truth information.

5.5 Analysis

Physics analyses require that the ESD is transformed into AOD. This is done by applying loose selection criteria on some of the reconstructed objects in the ESD. Additionally, some physics objects that are specific to AOD, such as jet tagging, are added.

5.5.1 B-physics analysis

The ATLAS B-physics group has developed a number of analysis tools [48] which extract B-decay candidates from AOD and produce ntuples that can

be analysed within the ROOT framework. The B-physics analysis tools have the following capabilities:

- Selecting tracks that match kinematic cuts for particle candidates, 2such as muons.
- Combining oppositely charged muon candidate pairs into J/ψ pre-candidates , and fitting such pairs to a vertex while applying appropriate selection cuts.
- Selecting B-decay product candidates additional to the J/ψ (such as K_S or K^{*0}) by combining tracks which are identified not to be muons or electrons.
- Matching particle tracks to Monte Carlo truth information.
- Calculating additional variables such as proper decay time and transverse decay length.

Chapter 6

The $\Delta\Gamma_d/\Gamma_d$ analysis

6.1 Introduction

The following four chapters describe in detail the analysis performed by the ATLAS collaboration to measure the relative width difference $\Delta\Gamma_d/\Gamma_d$ of the B^0–$\bar{B}^0$ system [9]. The aims of this analysis are to produce a measurement of $\Delta\Gamma_d/\Gamma_d$ with greater precision than any other experiment, from which results have differed by more than 1.5σ [7, 8], and to carry out an important null test of the Standard Model prediction. The method by which $\Delta\Gamma_d/\Gamma_d$ is measured is based on the theoretical description given in chapter 2.

6.2 Standard Model prediction

The prediction of the value of $\Delta\Gamma_d$ in the Standard Model relies on an operator product expansion, known as the heavy quark expansion, which is used to calculate Γ_{12} (defined in Section 2.3) as a simultaneous expansion in $\Lambda_{\mathrm{QCD}}/m_b$ and $\alpha_s(m_b)$ [49]. Λ_{QCD} is the QCD energy scale, m_b is the mass of the b quark and α_s is the strong coupling constant. The next to leading order (NLO) expansion of Γ_{12} was obtained in 2003 by Refs. [50, 51]. The NLO result was improved in 2007 by Ref. [52] using colour-enhanced α_s/m_b corrections.

These methods yield the current Standard Model result of [49]:

$$\frac{\Delta\Gamma_d}{\Delta M_d} = (0.54 \pm 0.10) \times 10^{-2} \tag{6.1}$$

The current experimental measurements of ΔM_d and $\tau(B^0)$ are [2]:

$$\Delta M_d = 0.510 \pm 0.003\ \text{ps}^{-1} \tag{6.2}$$

$$\tau(B^0) = 1/\Gamma_d = 1.520 \pm 0.004\text{ps} \tag{6.3}$$

These measurements have high enough precision to be used as the SM values and can therefore be combined with the theoretical result to obtain the Standard Model prediction of $\Delta\Gamma_d/\Gamma_d$:

$$\left.\frac{\Delta\Gamma_d}{\Gamma_d}\right|_{SM} = (0.42 \pm 0.08) \times 10^{-2} \tag{6.4}$$

Measurements of $\Delta\Gamma_d/\Gamma_d$ have been performed by the BaBar [53], Belle [7] and LHCb [8] collaborations. These results along with the current world average value [6] are given in Table 6.1.

Collaboration	$\Delta\Gamma_d/\Gamma_d$ ($\times 10^{-2}$)
BaBar	$-0.8 \pm 3.7(\text{stat.}) \pm 0.9(\text{syst.})$
Belle	$-1.7 \pm 1.8(\text{stat.}) \pm 1.1(\text{syst.})$
LHCb	$-4.4 \pm 2.5(\text{stat.}) \pm 1.1(\text{syst.})$
World average	-0.1 ± 1.0

Table 6.1: Previous experimental measurements of $\Delta\Gamma_d/\Gamma_d$ [53, 7, 8] and the world average value [6].

6.3 Measurement method

In principle, $\Delta\Gamma_d$ can be extracted from the lifetime distribution of the decay $B^0 \to f$, which is demonstrated in Eq. 2.37. Such a measurement, although possible, would give poor precision on $\Delta\Gamma_d$. Since $\Delta\Gamma_d \ll \Gamma_d$, the term $e^{-\Gamma_d t}$ dominates the lifetime distribution, preventing an accurate measurement of $\Delta\Gamma_d$. A more promising method is established by Refs. [54, 55], in which the ratio of the lifetime distributions of two different B^0 decay modes is measured. One of the decay modes should be a CP eigenstate, and the other a flavour specific state.

The measurement of $\Delta\Gamma_d$ presented in this chapter uses the CP eigenstate $J/\psi K_S$ and the flavour specific states $J/\psi K^{*0}$ and $J/\psi \bar{K}^{*0}$. The flavour specific states are added together and are henceforth denoted as $J/\psi K^{*0}$, unless otherwise stated. For both decay modes, the proper decay length of the B^0 meson L^B_{prop} is measured using the procedure described in chapter 7. The ratio $R(L^B_{\text{prop}})$ of the two decay modes is then computed as:

$$R(L^B_{\text{prop}}) = \frac{N(J/\psi K_S, L^B_{\text{prop}})}{N(J/\psi K^{*0}, L^B_{\text{prop}})}. \tag{6.5}$$

where $N(J/\psi K_S, L^B_{\text{prop}})$ and $N(J/\psi K^{*0}, L^B_{\text{prop}})$ are the numbers of reconstructed B^0 decays to the specified final state as a function of L^B_{prop}.

The expected decay rates as a function of the measured value L^B_{prop} are:

$$\Gamma(J/\psi K_S, L^B_{\text{prop}}) = \Gamma(J/\psi K_S, t) \otimes G(t) = \int_0^\infty G(L^B_{\text{prop}} - ct)\Gamma(J/\psi K_S, t)dt, \tag{6.6}$$

$$\Gamma(J/\psi K^{*0}, L^B_{\text{prop}}) = \Gamma(J/\psi K^{*0}, t) \otimes G(t) = \int_0^\infty G(L^B_{\text{prop}} - ct)\Gamma(J/\psi K^{*0}, t)dt, \tag{6.7}$$

where $G(L^B_{\text{prop}} - ct)$ is the detector resolution of L^B_{prop}, which is discussed in chapter 7. The lower limit of the integral is zero rather than negative infinity as L^B_{prop} and t are defined to be positive. The decay rate $\Gamma(J/\psi K_S, t)$ is given by Eq. 2.48. The expression for $\Gamma(J/\psi K^{*0}, t)$ is obtained from the sum of Eqs. 2.50 and 2.53. If the detection efficiencies of K^{*0} and $\bar{K}^{*0}$ are different, the terms proportional to the production asymmetry A_P in Eqs. 2.50 and 2.53 will not cancel in the sum, causing $\Gamma(J/\psi K^{*0}, t)$ to depend on A_P. The values of A_P and the relative difference in detection efficiencies of K^{*0} and $\bar{K}^{*0}$ mesons are both of the order of 10^{-2}, which is demonstrated in chapter 8. This produces a contribution of the order of 10^{-4} in $\Gamma(J/\psi K^{*0}, t)$, which can safely be neglected.

The value of $\Delta\Gamma_d$ is extracted from a fit to the experimental ratio (6.5) using expressions (6.6) and (6.7). The details of the fitting procedure are given in chapter 7. The J/ψ meson is reconstructed using the decay $J/\psi \to \mu^+\mu^-$ which offers a clean selection of J/ψ mesons and a highly efficient online trigger. The trigger efficiencies in the two B^0 decay channels are equal within minor effects related to the differences in the decay kinematics since only the

properties of the J/ψ meson are used to trigger the events. The K_S and K^{*0} mesons are reconstructed using the $K_S \to \pi^+\pi^-$ and $K^{*0} \to K^+\pi^-$ decays. The details of this reconstruction are given in Section 6.6. The chosen B^0 decay modes have the same number of charged particles (two muons and two hadrons) in the final state. Therefore, many experimental systematic uncertainties cancel in the ratio $R(L^B_{\text{prop}})$ resulting in an increased precision of the $\Delta\Gamma_d$ measurement. This is an important advantage of the selected approach.

6.4 Data sample

This analysis uses the full sample of pp collision data collected by the ATLAS detector in 2011 at $\sqrt{s} = 7$ TeV and in 2012 at $\sqrt{s} = 8$ TeV.

A set of dimuon trigger chains designed to select $J/\psi \to \mu^+\mu^-$ decays is used in this analysis. This collection of triggers includes numerous triggers with different muon p_{T} thresholds and additional topological and invariant mass requirements. The integrated luminosity corresponding to this selection of triggers is 4.9 fb^{-1} in 2011 and 20.3 fb^{-1} in 2012. The lifetime efficiency of the individual triggers is known to be significantly different. However, this efficiency is expected to cancel in the ratio (6.5), since both decays are selected with the same suite of triggers. A dedicated study conducted to prove this cancellation is presented in section 7.0.2.

6.5 Monte Carlo Samples

The method presented in Section 6.3 should be corrected to take into account the dependence of the reconstruction efficiencies of the $B^0 \to J/\psi K_S$ and $B^0 \to J/\psi K^{*0}$ decays on the B^0 lifetime. A large part of this dependence, together with any associated uncertainties, cancels in the ratio (6.5) because the number of final particles in both decay modes is the same and the procedure to measure the B^0 lifetime described in chapter 7 is similar in both cases. Selecting both channels in a consistent manner, described in Section 6.6, minimises any lifetime bias. Thus, the correction to the ratio (6.5) is expected to be small. Still, it cannot be eliminated completely be-

cause the hadronic tracks in the $B^0 \to J/\psi K_S$ decay come from a displaced $K_S \to \pi^+\pi^-$ vertex due to the long decay length of the K_S, whereas all four tracks in the $B^0 \to J/\psi K^{*0}$ decay originate from a single vertex as the K^{*0} decay length is effectively zero. This difference between the two channels is the main source of the experimental bias in the ratio (6.5), which can be evaluated only with Monte Carlo (MC) simulation. Using simulated events the quantity $R_{\text{eff}}(L^B_{\text{prop}})$ defined as

$$R_{\text{eff}}(L^B_{\text{prop}}) \equiv \frac{\varepsilon(B^0 \to J/\psi K_S, L^B_{\text{prop}})}{\varepsilon(B^0 \to J/\psi K^{*0}, L^B_{\text{prop}})}. \tag{6.8}$$

is measured. Here $\varepsilon(B^0 \to J/\psi K_S, L^B_{\text{prop}})$ and $\varepsilon(B^0 \to J/\psi K^{*0}, L^B_{\text{prop}})$ are the efficiencies to reconstruct $B^0 \to J/\psi K_S$ and $B^0 \to J/\psi K^{*0}$ decays, respectively.

In all cases the events are filtered at generator level by requiring two muons with $|\eta| < 2.5$ and transverse momenta, $p_T > 2.5$ GeV for the MC11 samples and $p_T > 3.5$ GeV for the MC12 samples. The events are passed through a full simulation of the detector as described in section 5.3, and processed with the same reconstruction algorithms including trigger requirements, as used for the data. All samples are produced with both MC11 and MC12 configurations to properly account for different conditions during the two years of data-taking. The decays of B^0 meson are simulated with Pythia 6.1 for the 7 TeV MC samples and with Pythia 8 for the 8 TeV MC samples.

6.6 Event reconstruction and selection

For a given event, the primary vertex (PV) of the pp collision producing the B^0 meson is determined using good-quality tracks reconstructed in the ID. The average transverse position of the pp collisions (the beam spot) is used in this determination as a constraint. Due to the high LHC luminosity, each event containing a B^0 meson is accompanied by a large number of pile-up interactions, which occur at various z positions along the beam line. These background interactions produce several PV candidates. The selection of the primary vertex corresponding to the B^0 production point is described in chapter 7.

All selection cuts presented in the following subsections were chosen to maximize the ratio of signal to background.

6.6.1 J/ψ reconstruction

The J/ψ candidates are reconstructed from pairs of oppositely charged muons. The pair of oppositely charged muons with $p_T > 2.5$ GeV and $|\eta| < 2.4$ is fitted to a common vertex with the VKalVrt fitter package [56]. The $\chi^2(J/\psi)$ of the vertex fit must satisfy $\chi^2(J/\psi)/n.d.f. < 16$, where $n.d.f.$ stands for the number of degrees of freedom and is equal to one in this case. The mass of the J/ψ candidate is required to be between 2.86 and 3.34 GeV.

6.6.2 K_S reconstruction

The K_S candidates are reconstructed from pairs of oppositely charged particle tracks not used in the primary or pile-up vertex reconstruction. Each track is required to have at least one hit in either of the two silicon detectors. The transverse momenta of the tracks must be greater than 400 MeV and have $|\eta| < 2.5$. The pairs are fitted to a common vertex and kept if the $\chi^2(K_S)/n.d.f. < 15$ ($n.d.f. = 1$), and the projection of the distance between the J/ψ and K_S vertices along the K_S momentum in the transverse plane is less than 44 cm. The ratio of this projection to its uncertainty must be greater than 2. Two additional requirements are related to the point of closest approach of the K_S trajectory to the J/ψ vertex in the xy plane. The distance between this point and the position of the J/ψ decay vertex in the xy plane is required to be less than 2 mm. The difference in the z coordinates of these two points must be less than 10 mm. These requirements help to reduce the combinatorial background. The mass of the K_S candidate is required to be between 465 and 535 MeV and its transverse momentum must be greater that 1 GeV. Additionally, the transverse decay length of the K_S ($L_{xy}(K_S)$) is required to be less than 440 mm and the ratio of $L_{xy}(K_S)$ to its uncertainty must be greater than two. The invariant mass distribution of the $K\pi$ pairs is shown in Fig. 6.1, in which the cut on $m(K_S)$ was removed and an additional cut of 5230 MeV $< m(B^0) <$ 5330 MeV was included.

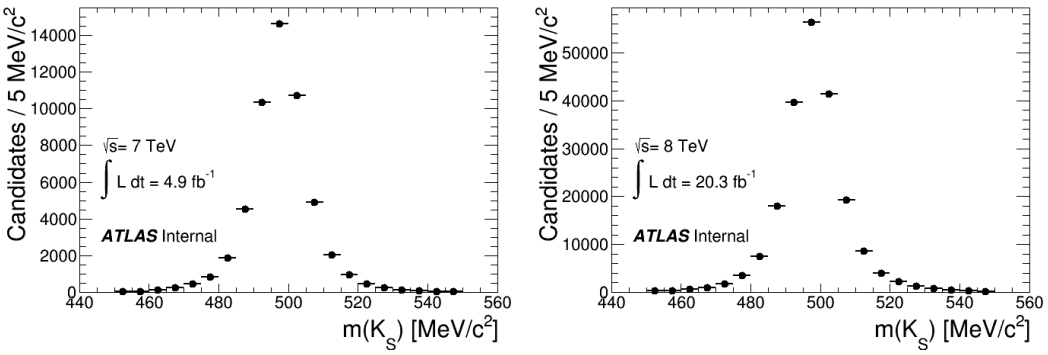

(a) (b)

Figure 6.1: The invariant mass distributions for K_S candidates for the (a) 2011 and (b) 2012 data sets.

6.6.3 $B^0 \to J/\psi K_S$ reconstruction

The $B^0 \to J/\psi(\mu^+\mu^-)\, K_S(\pi^+\pi^-)$ candidates are constructed by refitting the four tracks of the J/ψ and K_S candidates using VKalVrt. The muon tracks are constrained to intersect in a secondary vertex and their invariant mass is constrained to the nominal J/ψ mass [2]. The two pions from the K_S decay are constrained to originate from a tertiary vertex and their invariant mass is constrained to the nominal mass of the K_S meson [2]. The combined momentum of the refitted K_S decay tracks is required to point to the dimuon vertex. The fit has $n.d.f. = 6$. The quality of the cascade vertex fit is ensured by the requirement $\chi^2(B^0) - \chi^2(J/\psi) < 25$. Finally, the transverse momentum of the B^0 is required to exceed 10 GeV and its mass must be between 4900 and 5600 GeV. The invariant mass distribution of the $B^0 \to J/\psi K_S$ candidates is shown in Fig. 6.2.

6.6.4 $B^0 \to J/\psi K^{*0}$ reconstruction

For the selection of $B^0 \to J/\psi K^{*0}$ candidates, a J/ψ candidate and two additional oppositely charged particles are combined together. One particle is assigned the mass of the charged kaon and the other the mass of the charged pion. The transverse momentum of the kaon is required to exceed 800 MeV and the transverse momentum of the pion must be greater than

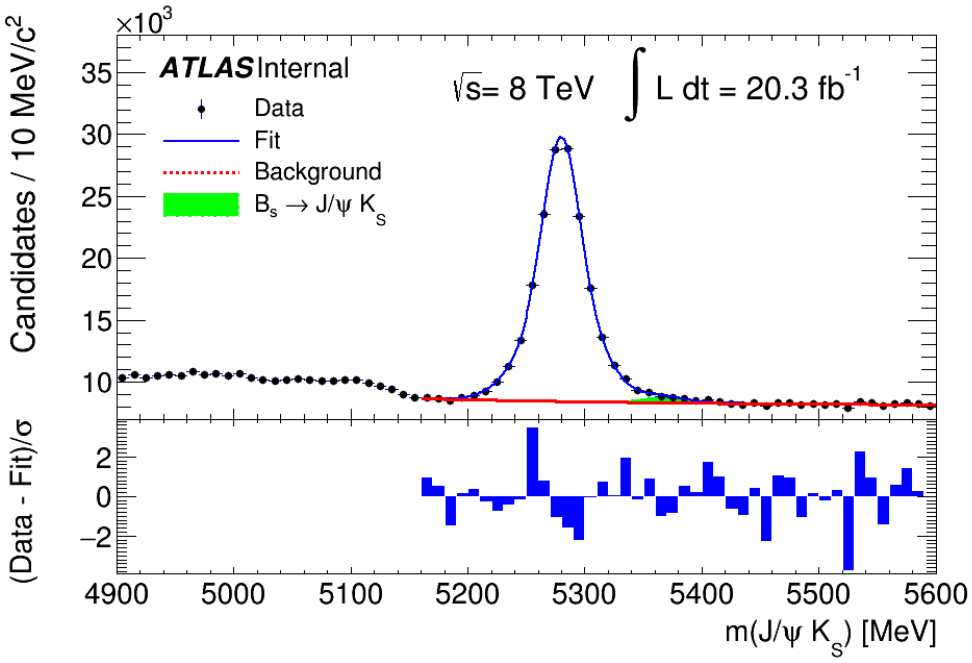

Figure 6.2: The invariant mass distribution of the total sample of $B^0 \to J/\psi K_S$ candidates in the 2012 data sample. The full line shows the result of the fit to the function described in the text. The dashed line shows the combinatorial background contribution. The filled area shows the peaking background contribution from the $B_s^0 \to J/\psi K_S$ decay. The lower frame of the figure shows the difference between each data point and the fit at that point divided by the statistical uncertainty of the data point.

400 MeV. The pseudorapidity of the kaon and pion tracks should be less than 2.5. A vertex fit of the four selected tracks is performed using the `VKalVrt` package. In this fit the invariant mass of the two muon tracks is constrained to the nominal J/ψ mass [2]. All four tracks are constrained to originate from the same vertex. The quality of the vertex fit is ensured by the requirement $\chi^2(B^0) - \chi^2(J/\psi) < 16$ imposed on the $\chi^2(B^0)$ of this fit. The invariant mass of the kaon and pion is required to be $850 < m(K\pi) < 950$ MeV. This range is slightly shifted with respect to the PDG value of the K^{*0} mass (895.81 ± 0.18 MeV) to provide a better suppression of the reflection from the $B_s \to J/\psi\phi$ decay. The transverse momentum of the $K\pi$ pair is required to exceed 2 GeV and the transverse momentum of the B^0 candidate must be greater than 10 GeV. Finally, the mass of the B^0 candidate must be between 4900 and 5600 GeV. The invariant mass distribution of the $K\pi$

pairs is shown in Fig. 6.3, in which the cut on $m(K\pi)$ was removed and an additional cut of 5230 MeV $< m(B^0) <$ 5330 MeV was included. The invariant mass distribution of the $B^0 \to J/\psi K^{*0}$ candidates is shown in Fig. 6.4.

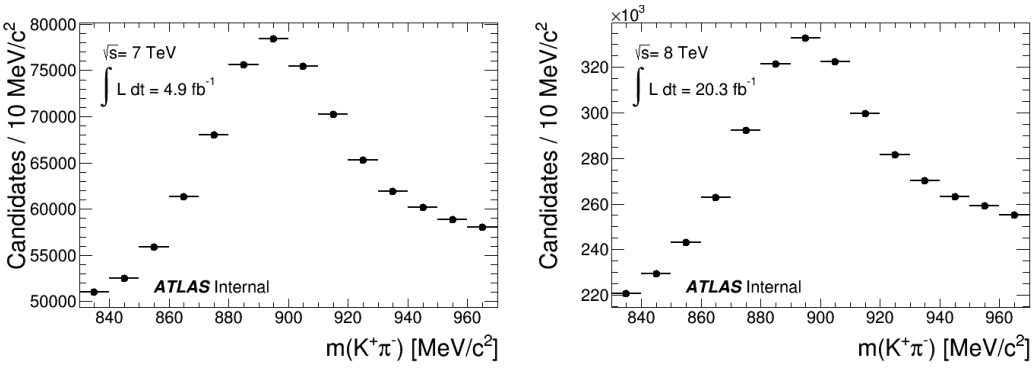

(a) (b)

Figure 6.3: The invariant mass distributions for $K\pi$ candidates for the (a) 2011 and (b) 2012 data sets.

Since particle identification of charged hadrons is not efficient in ATLAS, each pair of tracks is tested twice with the assignment of kaon and pion swapped. If both assignments satisfy the above selection criteria, the combination with the smallest deviation from the nominal K^{*0} mass [2] is chosen. The final states $J/\psi K^{*0}$ and $J/\psi \bar{K}^{*0}$ are not distinguished and the definition of the B^0 proper decay length discussed in chapter 7 is not sensitive to the assignment of masses. Therefore, the ambiguity of the kaon and pion identification does not impact on the obtained result.

Similarly to the $B^0 \to J/\psi K_S$ selection, no cuts are applied that could bias the lifetime distribution of the $B^0 \to J/\psi K^{*0}$ candidates. Also, multiple B^0 candidates satisfying all selection criteria are treated independently.

6.6.5 Multiplicity of B^0 candidates

If there are several $B^0 \to J/\psi K_S$ or $B^0 \to J/\psi K^{*0}$ candidates in a single event that pass the selection criteria, they will be included in the data sample. In such cases, the additional candidates contribute to the combinatorial background and do not impact the signal yields.

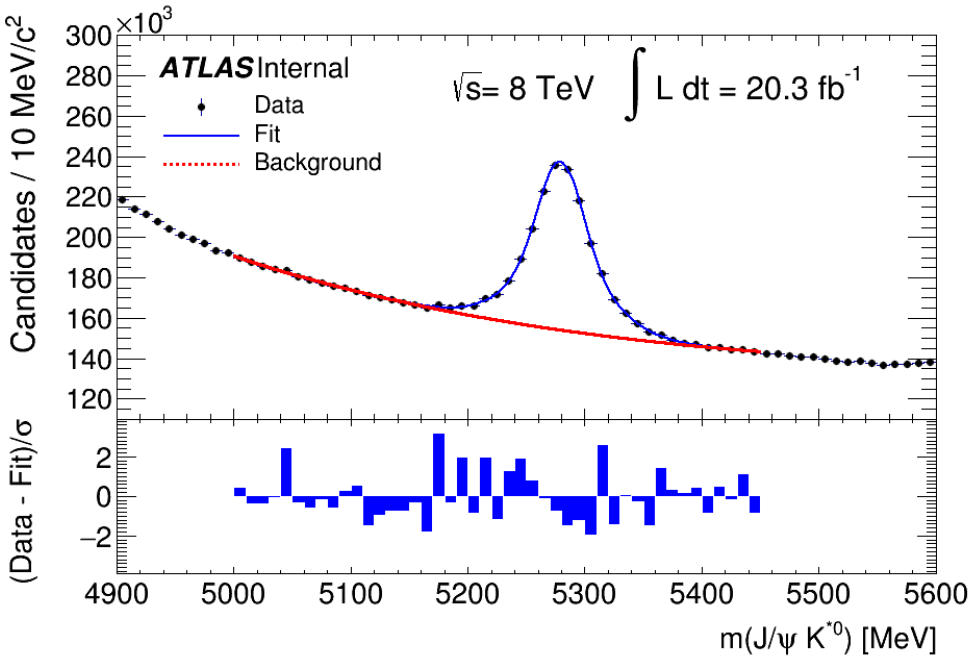

Figure 6.4: The invariant mass distribution of the total sample of $B^0 \to J/\psi K^{*0}$ candidates in the 2012 data sample.

The $B^0 \to J/\psi K_S$ channel has a mean of 1.01 candidates in each event for the 2011 and 2012 data sets. The mean number of $B^0 \to J/\psi K_S$ candidates in Monte Carlo is 1.00 in both 2011 and 2012.

For the $B^0 \to J/\psi K^{*0}$ channel, there is a mean of 1.41 candidates per event in the 2011 data set and 1.44 in the 2012 data set. In Monte Carlo, the average number of $B^0 \to J/\psi K^{*0}$ candidates per event is 1.16 in 2011 and 2012. The $B^0 \to J/\psi K^{*0}$ channel has a much larger combinatorial background contribution than the $B^0 \to J/\psi K_S$ channel and as such has more candidates per event on average. In simulation, only the decay $B^0 \to J/\psi K^{*0}$ was simulated. Therefore, the multiplicity of candidates in simulation is lower. Figure 6.5 shows the number of B^0 candidates that pass selection in each event in data and Monte Carlo.

6.6.6 Selection efficiencies

Tables 6.2 to 6.5 show all selection cuts applied to events in the Monte Carlo samples, and their sequential efficiencies. The final selection efficiency is

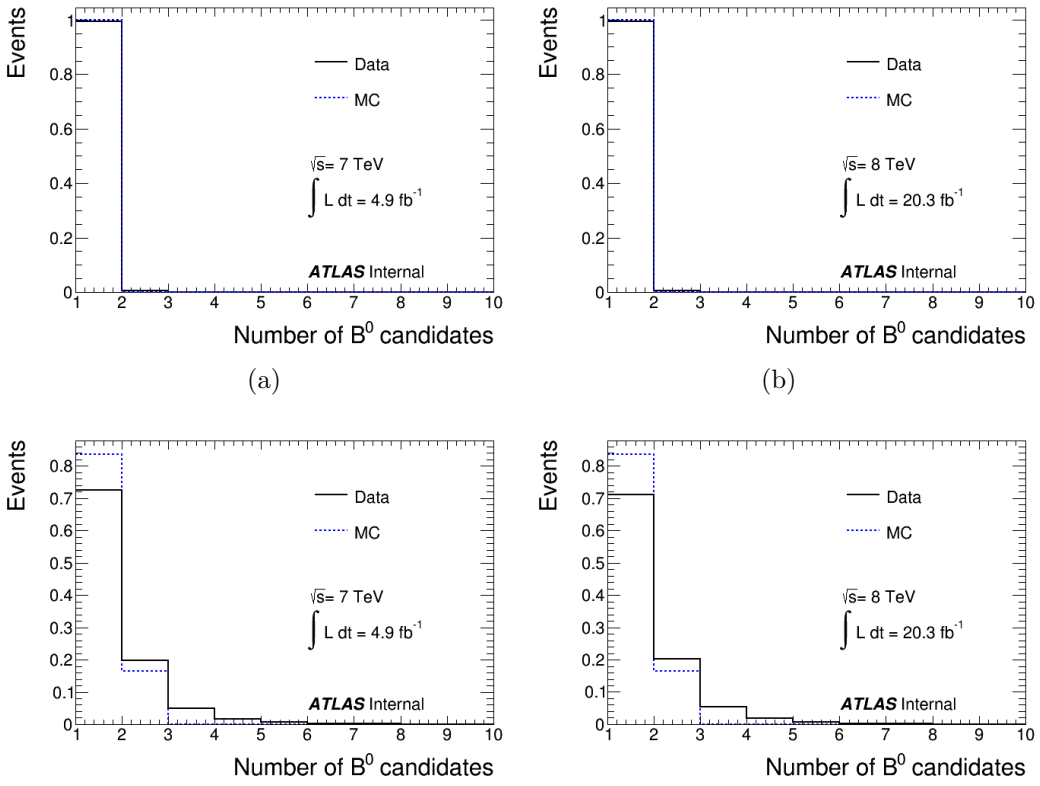

Figure 6.5: Number of B^0 candidates per event for (a,b) $B^0 \to J/\psi K_S$ decays and (c,d) $B^0 \to J/\psi K^{*0}$ decays.

lower in 2011 than in 2012 primarily due to the smaller value of $\sqrt{s}$ in 2011, which causes the transverse momentum cuts to be more impactful.

Cut	Efficiency (%)
$\chi^2(J/\psi) < 16$	99.56
$2860\,\text{MeV} < m(J/\psi) < 3340\,\text{MeV}$	99.28
$\chi^2(B^0) - \chi^2(J/\psi) < 25$	95.57
$465\,\text{MeV} < m(K_S) < 535\,\text{MeV}$	94.84
$p_T(K_S) > 1\,\text{GeV}$	93.97
$p_T(B^0) > 10\,\text{GeV}$	86.31
$L_{xy}(K_S) < 440\,\text{mm}$	86.31
$L_{xy}(K_S)/\sigma_{L_{xy}}(K_S) > 2$	86.30
$4900\,\text{MeV} < m(B^0) < 5600\,\text{MeV}$	85.76

Table 6.2: Selection efficiencies for $B^0 \to J/\psi K_S$ events in 2011.

Cut	Efficiency (%)
$\chi^2(J/\psi) < 16$	99.72
$2860\,\text{MeV} < m(J/\psi) < 3340\,\text{MeV}$	99.47
$\chi^2(B^0) - \chi^2(J/\psi) < 25$	96.13
$465\,\text{MeV} < m(K_S) < 535\,\text{MeV}$	95.38
$p_T(K_S) > 1\,\text{GeV}$	94.49
$p_T(B^0) > 10\,\text{GeV}$	89.94
$L_{xy}(K_S) < 440\,\text{mm}$	89.94
$L_{xy}(K_S)/\sigma_{L_{xy}}(K_S) > 2$	89.93
$4900\,\text{MeV} < m(B^0) < 5600\,\text{MeV}$	89.47

Table 6.3: Selection efficiencies for $B^0 \to J/\psi K_S$ events in 2012.

Cut	Efficiency (%)
$\chi^2(J/\psi) < 16$	99.99
$2860\,\text{MeV} < m(J/\psi) < 3340\,\text{MeV}$	99.72
$\chi^2(B^0) - \chi^2(J/\psi) < 16$	98.21
$850\,\text{MeV} < m(K^{*0}) < 950\,\text{MeV}$	88.70
$p_T(K^+) > 800\,\text{MeV}$	87.97
$p_T(K^{*0}) > 2\,\text{GeV}$	87.97
$p_T(B^0) > 10\,\text{GeV}$	87.97
$4900\,\text{MeV} < m(B^0) < 5600\,\text{MeV}$	87.97

Table 6.4: Selection efficiencies for $B^0 \to J/\psi K^{*0}$ events in 2011.

Cut	Efficiency (%)
$\chi^2(J/\psi) < 16$	99.99
$2860\,\text{MeV} < m(J/\psi) < 3340\,\text{MeV}$	99.77
$\chi^2(B^0) - \chi^2(J/\psi) < 16$	98.38
$850\,\text{MeV} < m(K^{*0}) < 950\,\text{MeV}$	89.24
$p_T(K^+) > 800\,\text{MeV}$	88.52
$p_T(K^{*0}) > 2\,\text{GeV}$	88.52
$p_T(B^0) > 10\,\text{GeV}$	88.52
$4900\,\text{MeV} < m(B^0) < 5600\,\text{MeV}$	88.52

Table 6.5: Selection efficiencies for $B^0 \to J/\psi K^{*0}$ events in 2012.

Chapter 7

The proper decay length of the B^0 meson

This chapter details the adopted method used to measure the proper decay length of the B^0 meson in the $B^0 \to J/\psi K_S$ and $B^0 \to J/\psi K^{*0}$ channels which, as explained in Section 6.3, is required for the measurement of $\Delta\Gamma_d/\Gamma_d$. The procedure is explicitly designed to use the same input information in both the $B^0 \to J/\psi K_S$ and $B^0 \to J/\psi K^{*0}$ channels. The aim of this approach is to reduce the experimental bias in the ratio (6.5). The origin of the B^0 meson coincides with the primary pp interaction point. The tracks from the B^0 candidate are excluded in the measurement of the primary vertex (PV) position. The position of the B^0 decay is determined by the J/ψ vertex, which is obtained from the vertex fit of the two muons, and is not affected by the additional particles from the B^0 decay. Therefore, there is no intrinsic difference in the proper decay length measurement of the two B^0 decay modes.

The proper decay length of the B^0 meson, L^B_{prop}, is determined in the xy plane of the detector because of the better precision compared to the measurement in three dimensions, strengthened by the small transverse size of the beam spot. A further advantage of measuring L^B_{prop} in the xy plane is the reduced dependence on pile-up interactions, which occur at various z positions along the beam line. The PV corresponding to the B^0 production point is selected from all reconstructed PVs as follows. For each PV candidate, the point of closest approach of the B^0 trajectory to the PV in the

xy plane is determined and the difference δz of the z coordinates of these two points is measured. The candidate with the minimum absolute value of δz is selected as the B^0 production vertex. As with any other procedure of PV selection, this method is not ideal and occasionally a wrong PV is selected due to the resolution for the B^0 momentum direction. However, any selected PV should be close enough to the true B^0 production vertex because numerically $\delta z \sim \mathcal{O}(1\text{ mm})$ and both vertices are located on the beam line, which has a gradient of approximately 10^{-3} in both the xz and yz planes. In addition, as shown in Table 3.1, the transverse size of the beam spot is about 15 μm in both the x and y directions, and so the distance between the true vertex and the selected vertex in the xy plane is expected to be much less than the precision of the decay length measurement, which is about 100 μm. The fraction of events in which the selected PV does not correspond to the true B^0 vertex is estimated using Monte Carlo and is found to be very small, at about 10^{-4} in 2011 and 2×10^{-4} in 2012 for both B^0 decay modes. The higher value in 2012 is expected due to the increased number of pile-up vertices. Thus, the measurement of L^B_{prop} performed in the xy plane is not significantly affected by any incorrect selection of the PV.

For each reconstructed $B^0 \to J/\psi K_S$ or $B^0 \to J/\psi K^{*0}$ candidate, L^B_{prop} is measured using the projection of the B^0 decay length along the B^0 momentum in the plane transverse to the beam axis:

$$L^B_{\text{prop}} = \mathbf{L^B_{xy}} \cdot \hat{\mathbf{p}}^{\mathbf{B}}_{\text{T}} \frac{m_{B^0}}{p^B_{\text{T}}} = \frac{(x^{J/\psi} - x^{\text{PV}})p^B_x + (y^{J/\psi} - y^{\text{PV}})p^B_y}{(p^B_{\text{T}})^2} m_{B^0}. \tag{7.1}$$

Here, $\mathbf{L^B_{xy}}$ is the transverse decay length of the B^0 meson and $\mathbf{p}^{\mathbf{B}}_{\text{T}}$ is its transverse momentum vector, where $p^B_{\text{T}} = |\mathbf{p}^{\mathbf{B}}_{\text{T}}|$. The quantity $m_{B^0} = 5279.61$ MeV [2] is the mass of the B^0 meson. The variables $x^{J/\psi}, y^{J/\psi}$ are the coordinates of the J/ψ vertex; $x^{\text{PV}}, y^{\text{PV}}$ are the coordinates of the primary vertex and p^B_x, p^B_y are the x and y components of the momentum of the B^0 meson.

The resolution of L^B_{prop} is obtained from simulation. It is found to be very similar for the two decay modes. Figure 7.1 shows the distribution of the resolution, given by $L^B_{\text{prop}} - ct$, where t is the true proper decay time of the B^0 meson. This distribution for the $J/\psi K_S$ and $J/\psi K^{*0}$ decay modes is fitted by the function $G(L^B_{\text{prop}} - ct)$ defined as the sum of two Gaussian

functions:

$$G(x) = \frac{1}{\sqrt{2\pi}} \left(\frac{f}{\sigma_1} e^{-x^2/(2\sigma_1^2)} + \frac{1-f}{\sigma_2} e^{-x^2/(2\sigma_2^2)} \right). \tag{7.2}$$

where f is the fraction of $G(x)$ comprised by the first Gaussian function and σ_1 and σ_2 are, respectively, the standard deviations of the first and second Gaussian functions. The values of f, σ_1 and $\sigma_2$obtained from the fit for both decay modes are given in Table 7.1.

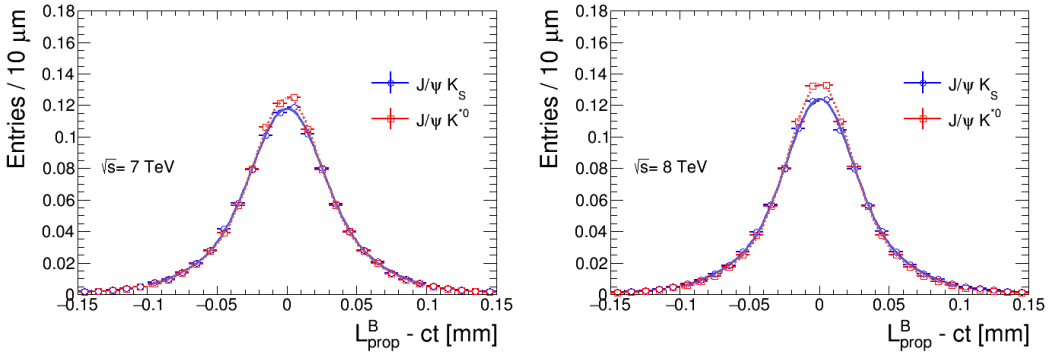

(a) (b)

Figure 7.1: Distribution of $L^B_{\text{prop}} - ct$. in (a) the 2011 data sample and (b) the 2012 data sample.

Year	$\sqrt{s}$	Channel	f	σ_1 [mm]	σ_2 [mm]
2011	7 TeV	$B^0 \to J/\psi K_S$	0.454	0.0234	0.0502
2011	7 TeV	$B^0 \to J/\psi K^{*0}$	0.412	0.0212	0.0518
2012	8 TeV	$B^0 \to J/\psi K_S$	0.453	0.0221	0.0482
2012	8 TeV	$B^0 \to J/\psi K^{*0}$	0.456	0.0206	0.0455

Table 7.1: Parameters describing the resolution of L^B_{prop}. The uncertainties on these parameters are negligible as they are obtained from the high statistics of the MC samples.

To obtain the proper decay length distributions in the studied B^0 decay modes, the range of L^B_{prop} between -0.3 and 6 mm is divided into ten bins defined in Table 7.2. The selected bin size is much larger than the average resolution of L^B_{prop}, which is approximately 35 μm for the $J/\psi K_S$ channel and 33 μm for the $J/\psi K^{*0}$ channel. In each bin of L^B_{prop}, the number of

$B^0 \to J/\psi K_S$ and $B^0 \to J/\psi K^{*0}$ decays are extracted from a binned log-likelihood fit to the corresponding mass distributions.

Bin number	1	2	3	4	5	6	7	8	9	10
Lower edge [mm]	−0.3	0.0	0.3	0.6	0.9	1.2	1.5	1.8	2.1	3.0
Upper edge [mm]	0.0	0.3	0.6	0.9	1.2	1.5	1.8	2.1	3.0	6.0

Table 7.2: Definition of the L^B_{prop} bins.

In this fit, the mass distributions are modelled by a sum of functions describing the signal and background components. For the $B^0 \to J/\psi K^{*0}$ channel, the signal function $f_s^{J/\psi K^{*0}}$ is defined as the sum of two Gaussian functions. The Gaussian functions are constrained to have the same mean. The background function $f_b^{J/\psi K^{*0}}$ is defined using an exponential function with a second-order polynomial as the exponent. The fit is first applied to the total sample (shown in Fig 6.4) to determine the mean and standard deviations of the two Gaussian functions and their relative fractions. For the fit in each L^B_{prop} bin, all parameters describing the signal, except the normalisation of $f_s^{J/\psi K^{*0}}$, are fixed to the values obtained in the fit of the total sample. A dedicated study was performed to verify that fixing the parameters of the signal does not produce any bias in the result, which is described in Section 7.0.1. The parameters of $f_b^{J/\psi K^{*0}}$ remain free.

The signal function for the $B^0 \to J/\psi K_S$ channel $f_s^{J/\psi K_S}$ is defined as the sum of two Gaussian functions. The background is modelled by the sum of two functions: $f_b^{J/\psi K_S} = f_b^c + f_b^{B_s}$. The combinatorial background function f_b^c is defined using an exponential function with a second-order polynomial as the exponent. The second function, $f_b^{B_s}$, accounts for the contribution from $B_s^0 \to J/\psi K_S$ decays and is defined as the sum of two Gaussian functions. The $B_s^0 \to J/\psi K_S$ contribution is visible in the mass distribution as a shoulder in the signal peak, as can be seen in Fig. 6.2. Its fraction relative to the $B^0 \to J/\psi K_S$ signal is $\sim 1\%$. The signal Gaussian functions are constrained to have the same mean. The relative fractions and standard deviations of the B_s^0 background Gaussian functions are parameterised to be the same as those of the signal Gaussian functions. The B_s^0 background Gaussian functions are also constrained to have the same mean. The mean

of the B_s^0 background Gaussian functions is shifted relative to the mean of the signal Gaussian functions by the difference between the nominal masses of the B_s^0 and B^0 mesons (87.34 MeV) [2]. The fit is first applied to the total sample to determine the mean and standard deviations of the signal Gaussian functions and their relative fractions. For the fit in each $L^B_{\rm prop}$ bin, all parameters describing the signal, except the normalisation of $f_s^{J/\psi K_S}$, are fixed to the values obtained in the fit of the total sample. The parameters of $f_b^{B_s}$ are also fixed, except for the normalisation. A dedicated study was performed to verify that fixing the parameters of the signal does not produce any bias in the result, which is described in Section 7.0.1. All parameters of f_b^c remain free.

The separation of the $B^0 \to J/\psi K_S$ and $B_s^0 \to J/\psi K_S$ contributions is important for the $\Delta\Gamma_d$ measurement because the mean lifetimes of the B^0 and B_s^0 mesons decaying to this CP eigenstate are different. On the contrary, the separation of $B^0 \to J/\psi K^{*0}$ and $B_s^0 \to J/\psi K^{*0}$ decays is not necessary because the lifetimes of the B^0 and B_s^0 mesons decaying to this final state are equal to within 1% [2, 6]. Thus, the small ($\sim$1%) contribution of the $B_s^0 \to J/\psi K^{*0}$ decay does not have an impact on the $\Delta\Gamma_d$ measurement.

The fit ranges of the $J/\psi K_S$ and $J/\psi K^{*0}$ mass distributions are selected such that the background under the B^0 signal is smooth. The mass distribution $m(J/\psi K_S)$ contains a contribution from partially reconstructed $B \to J/\psi K_S \pi$ decays. This contribution has a threshold at $m(J/\psi K_S) \simeq m(B^0) - m(\pi) \simeq 5130$ MeV. For this reason, the fit range $5160 < m(J/\psi K_S) < 5600$ MeV is selected. The corresponding contribution of $B \to J/\psi K^{*0}\pi$ decays is smaller. Therefore, the lower limit of the fit range of $m(J/\psi K^{*0})$ is selected at 5000 MeV. The impact of the selection of the fit range on the value of $\Delta\Gamma_d$ is included in the systematic uncertainty.

The total number of signal $B^0 \to J/\psi K_S$ decays obtained from the fit to the total sample is $28\,170 \pm 250$ in the 2011 data set and $110\,800 \pm 520$ in the 2012 data set. For $B^0 \to J/\psi K^{*0}$ decays the corresponding numbers are $129\,200 \pm 900$ in the 2011 data set and $555\,800 \pm 1\,900$ in the 2012 data set. Figures 7.2 - 7.11 show the fitted mass distributions of $B^0 \to J/\psi K_S$ candidates and $B^0 \to J/\psi K^{*0}$ candidates in the bins of $L^B_{\rm prop}$ defined in Table 7.2 for the 2012 data sample.

Figure 7.12 shows the number of signal events and its statistical uncertainty in each bin as a function of $L^B_{\rm prop}$ for the $B^0 \to J/\psi K_S$ and $B^0 \to J/\psi K^{*0}$ channels. The ratio of the numbers of B^0 candidates in the two channels computed in each $L^B_{\rm prop}$ bin i gives the experimental ratio $R_{i,\rm uncor}$ defined as:

$$R_{i,\rm uncor} = \frac{N_i(J/\psi K_S)}{N_i(J/\psi K^{*0})}. \tag{7.3}$$

Here $N_i(J/\psi K_S)$ and $N_i(J/\psi K^{*0})$ are the numbers of events in a given bin i. This ratio has to be corrected by the ratio of the reconstruction efficiencies in each $L^B_{\rm prop}$ bin $R_{i,\rm eff}(L^B_{\rm prop})$ defined by Eq. (6.8). The determination of $R_{i,\rm eff}(L^B_{\rm prop})$ is explained is Section 9.1.

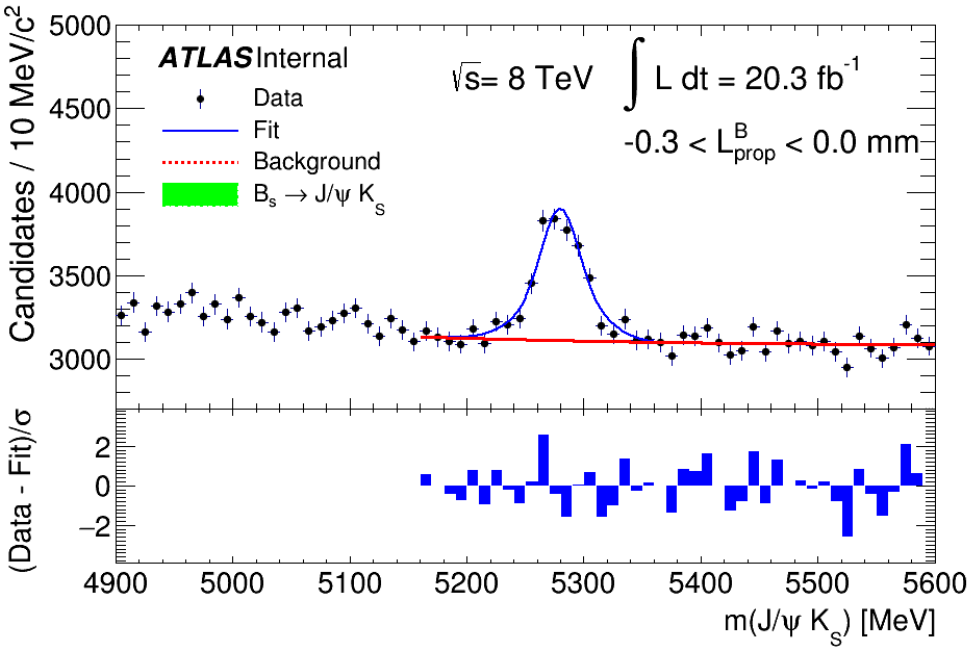

(a)

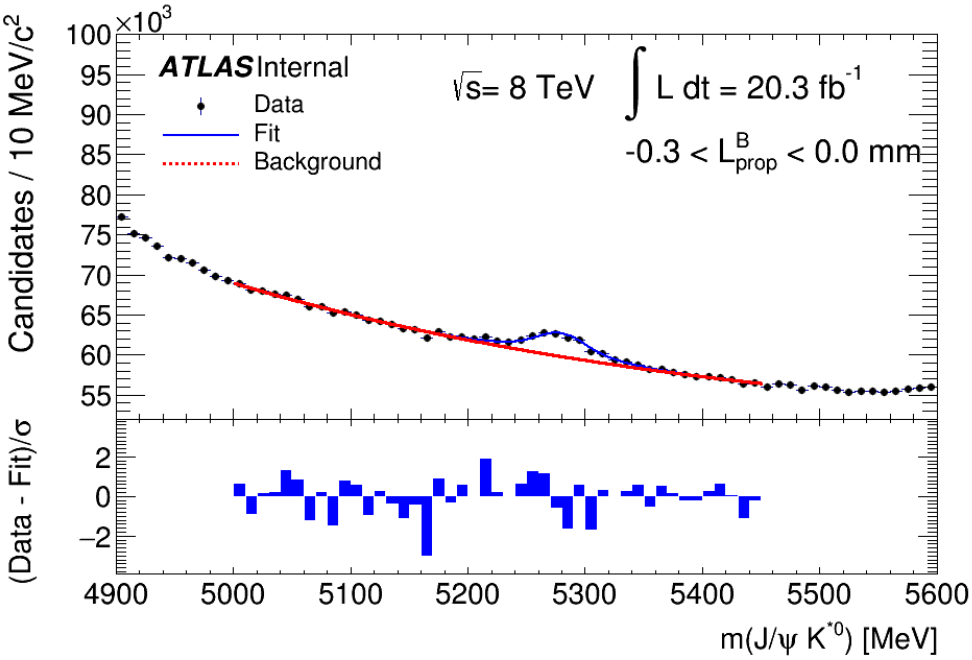

(b)

Figure 7.2: The invariant mass distributions of (a) $B^0 \to J/\psi K_S$ candidates and (b) $B^0 \to J/\psi K^{*0}$ candidates in 2012 for $-0.3 < L^B_{\text{prop}} < 0.0$ mm. The full line shows the result of the fit to the function described in the text. The dashed line shows the combinatorial background contribution. The filled area in figure (a) shows the peaking background contribution from the $B^0_s \to J/\psi K_S$ decay. The lower frame of each figure shows the difference between each data point and the fit at that point divided by the statistical uncertainty of the data point.

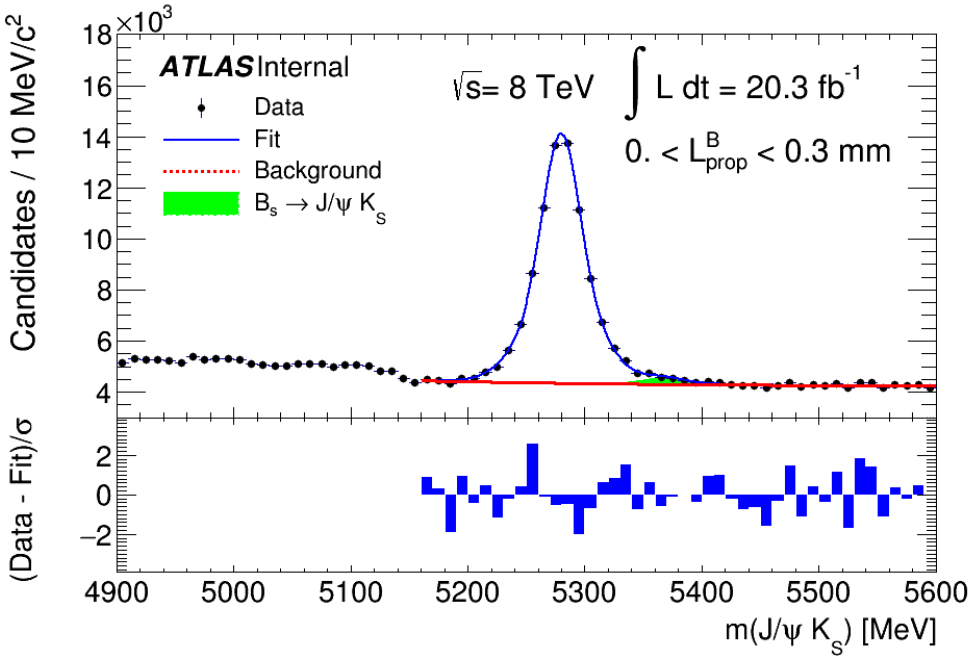

(a)

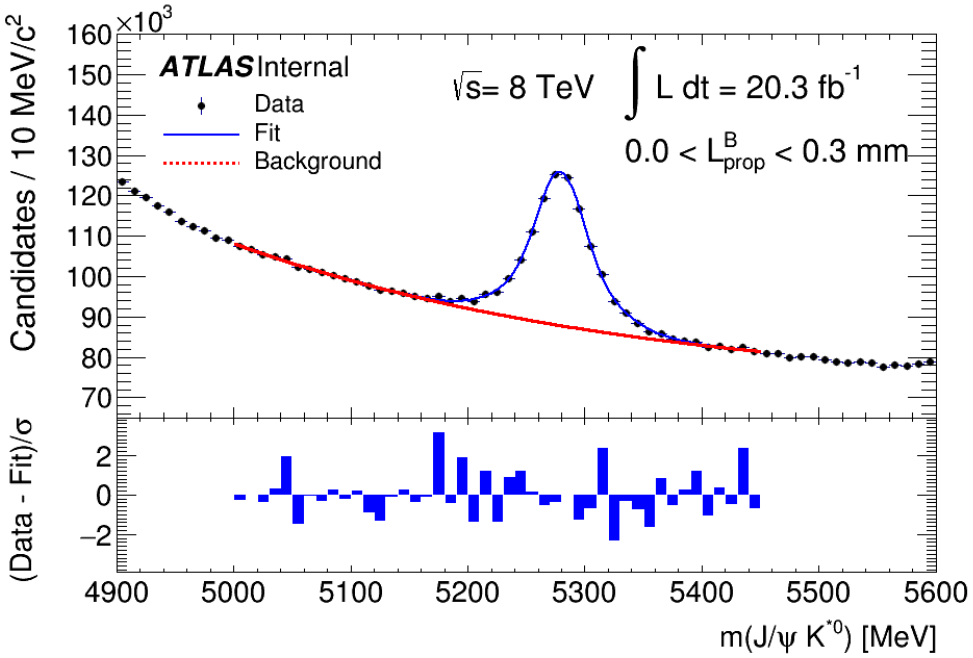

(b)

Figure 7.3: The invariant mass distributions of (a) $B^0 \to J/\psi K_S$ candidates and (b) $B^0 \to J/\psi K^{*0}$ candidates in 2012 for $0.0 < L^B_{\text{prop}} < 0.3$ mm. The full line shows the result of the fit to the function described in the text. The dashed line shows the combinatorial background contribution. The filled area in figure (a) shows the peaking background contribution from the $B^0_s \to J/\psi K_S$ decay. The lower frame of each figure shows the difference between each data point and the fit at that point divided by the statistical uncertainty of the data point.

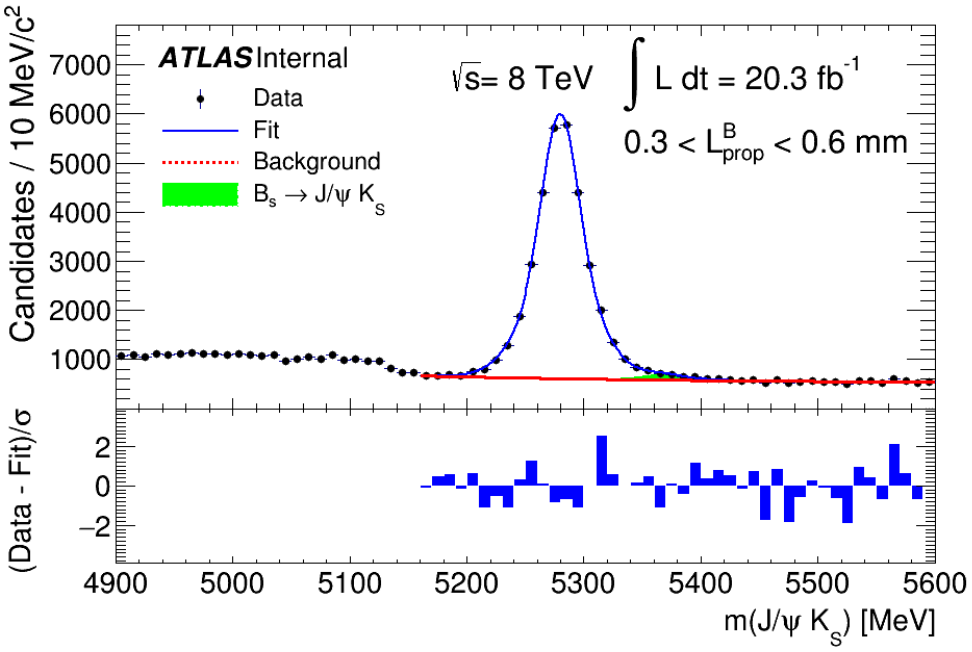

(a)

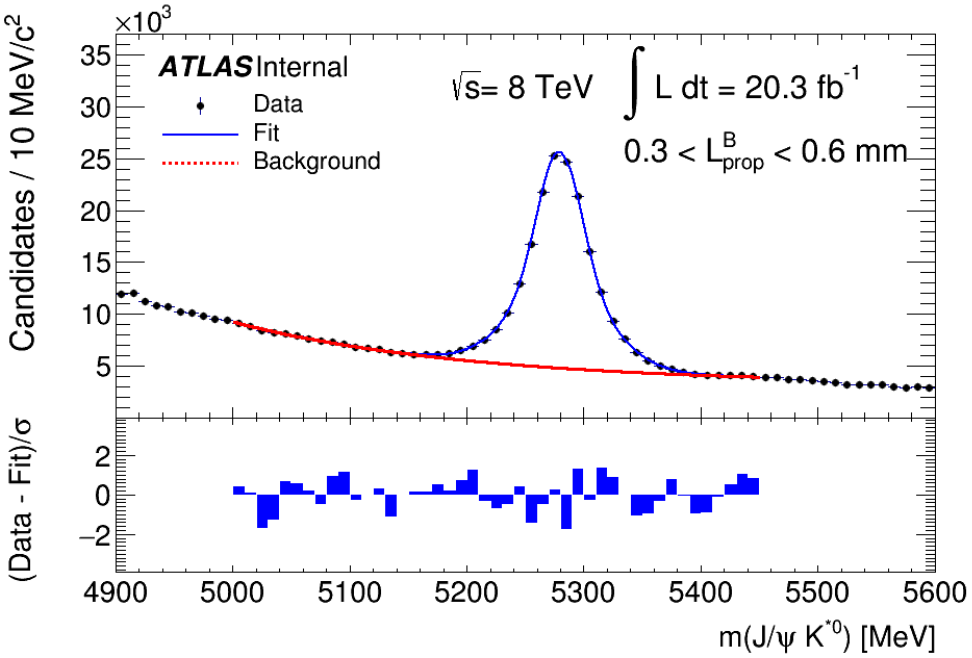

(b)

Figure 7.4: The invariant mass distributions of (a) $B^0 \to J/\psi K_S$ candidates and (b) $B^0 \to J/\psi K^{*0}$ candidates in 2012 for $0.3 < L^B_{\text{prop}} < 0.6$ mm. The full line shows the result of the fit to the function described in the text. The dashed line shows the combinatorial background contribution. The filled area in figure (a) shows the peaking background contribution from the $B^0_s \to J/\psi K_S$ decay. The lower frame of each figure shows the difference between each data point and the fit at that point divided by the statistical uncertainty of the data point.

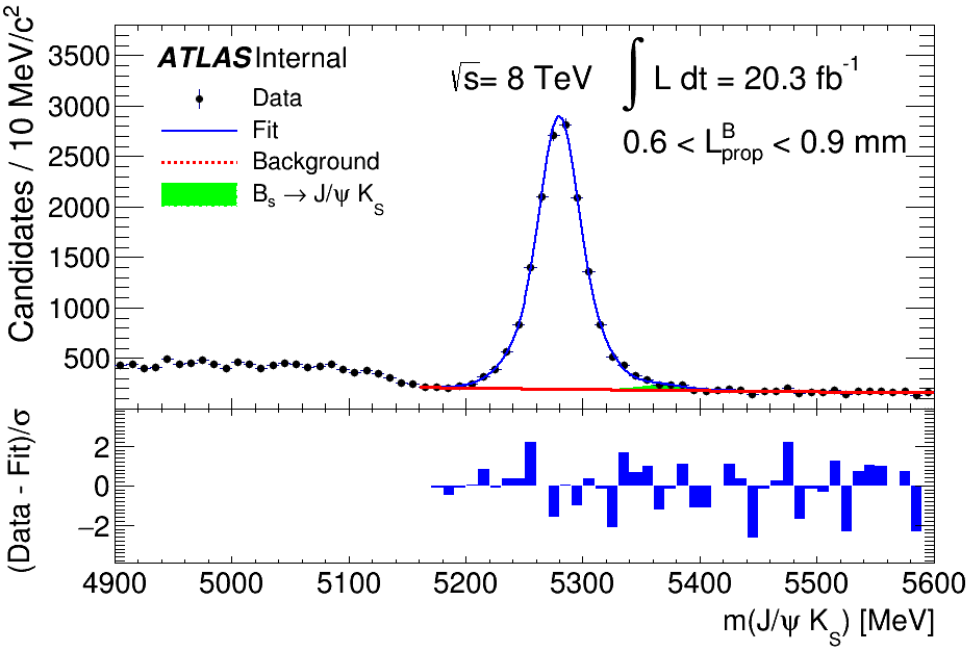

(a)

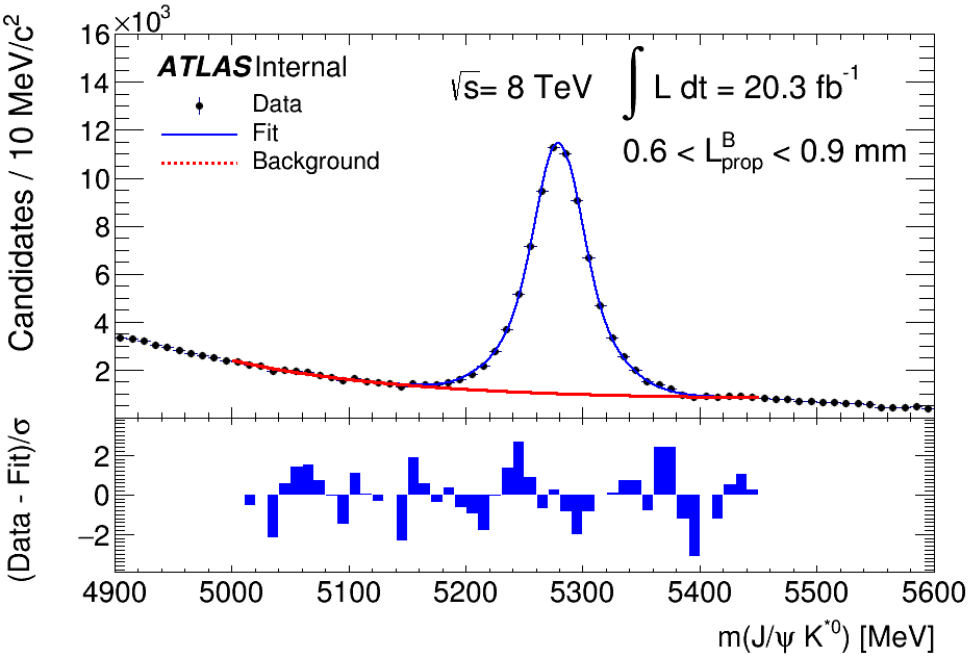

(b)

Figure 7.5: The invariant mass distributions of (a) $B^0 \to J/\psi K_S$ candidates and (b) $B^0 \to J/\psi K^{*0}$ candidates in 2012 for $0.6 < L^B_{\text{prop}} < 0.9$ mm. The full line shows the result of the fit to the function described in the text. The dashed line shows the combinatorial background contribution. The filled area in figure (a) shows the peaking background contribution from the $B^0_s \to J/\psi K_S$ decay. The lower frame of each figure shows the difference between each data point and the fit at that point divided by the statistical uncertainty of the data point.

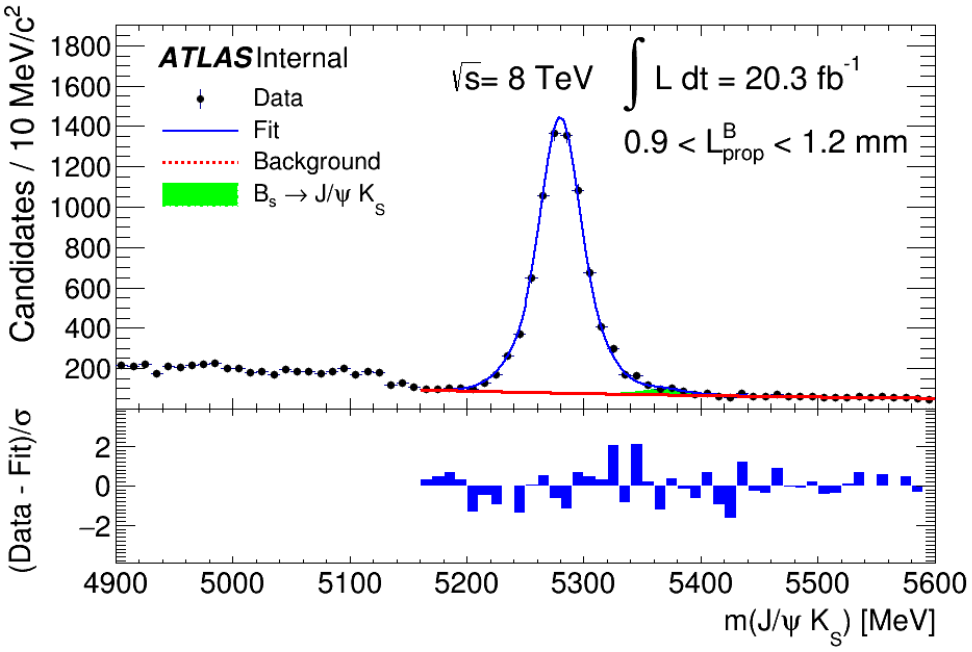

(a)

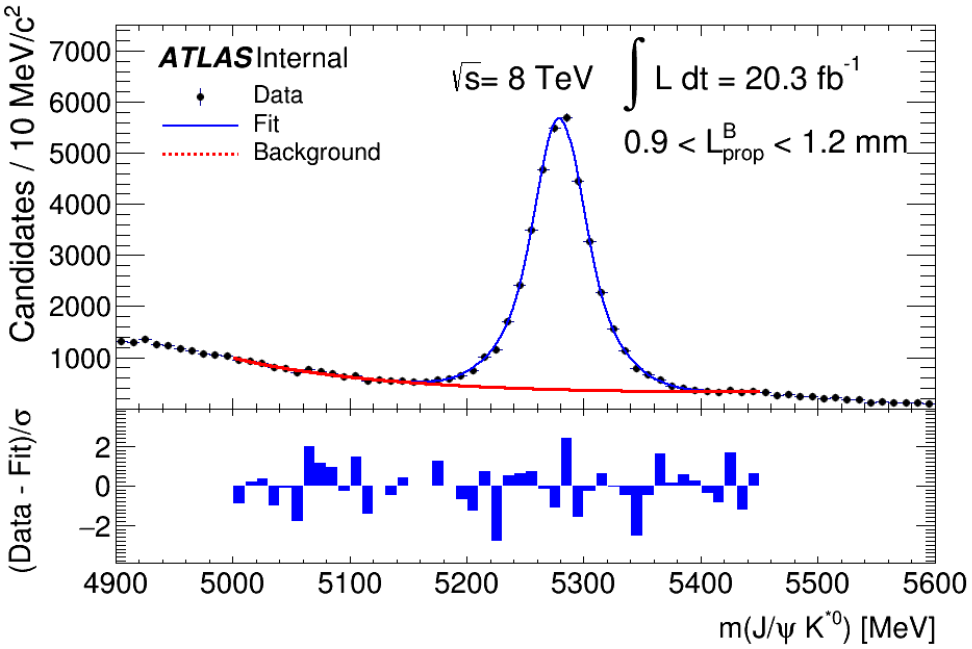

(b)

Figure 7.6: The invariant mass distributions of (a) $B^0 \to J/\psi K_S$ candidates and (b) $B^0 \to J/\psi K^{*0}$ candidates in 2012 for $0.9 < L^B_{\text{prop}} < 1.2$ mm. The full line shows the result of the fit to the function described in the text. The dashed line shows the combinatorial background contribution. The filled area in figure (a) shows the peaking background contribution from the $B^0_s \to J/\psi K_S$ decay. The lower frame of each figure shows the difference between each data point and the fit at that point divided by the statistical uncertainty of the data point.

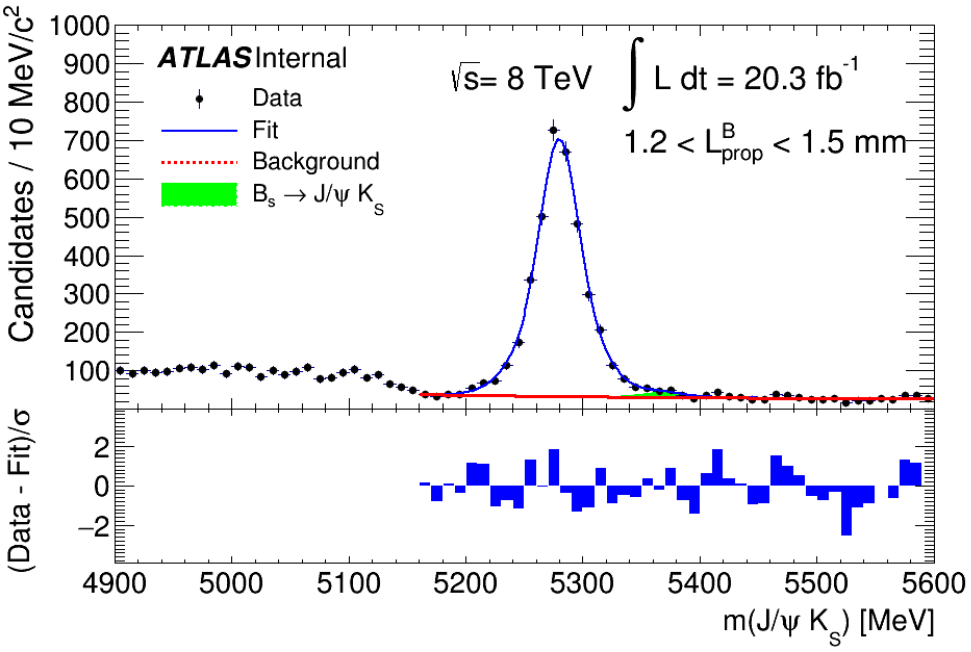

(a)

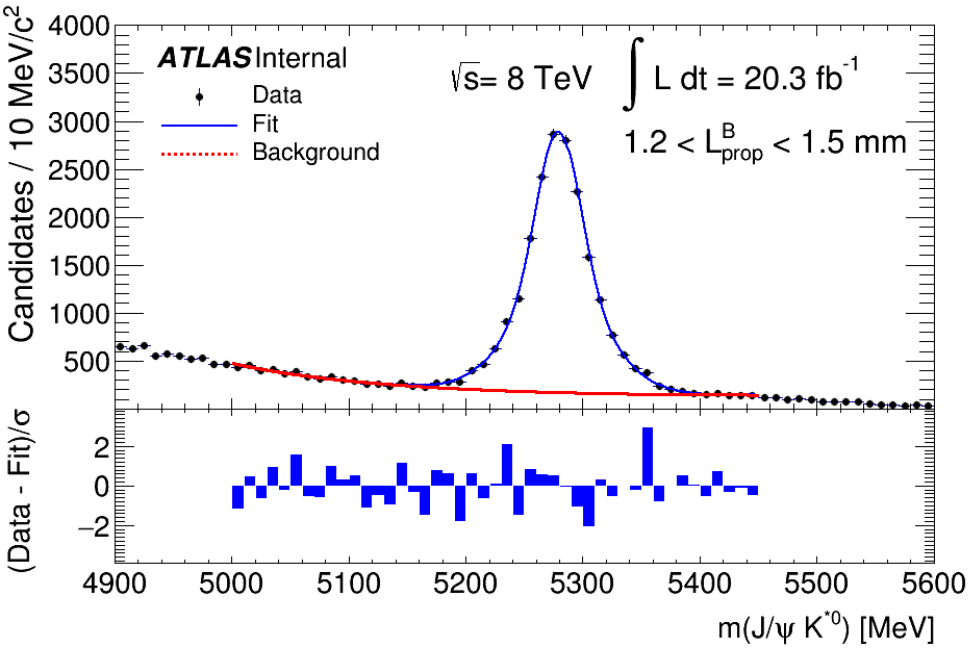

(b)

Figure 7.7: The invariant mass distributions of (a) $B^0 \to J/\psi K_S$ candidates and (b) $B^0 \to J/\psi K^{*0}$ candidates in 2012 for $1.2 < L^B_{\text{prop}} < 1.5$ mm. The full line shows the result of the fit to the function described in the text. The dashed line shows the combinatorial background contribution. The filled area in figure (a) shows the peaking background contribution from the $B^0_s \to J/\psi K_S$ decay. The lower frame of each figure shows the difference between each data point and the fit at that point divided by the statistical uncertainty of the data point.

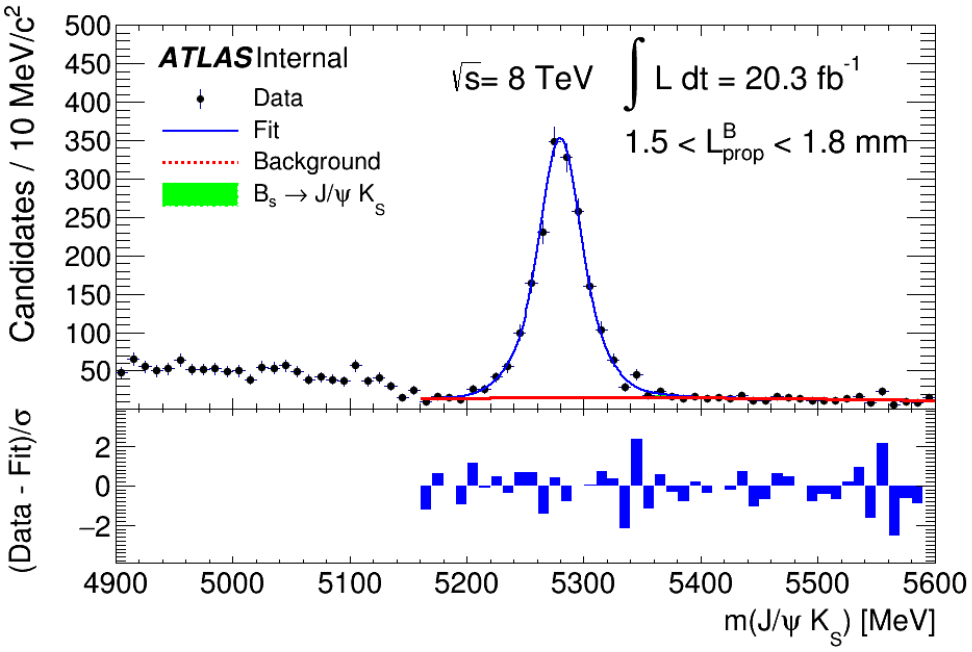

(a)

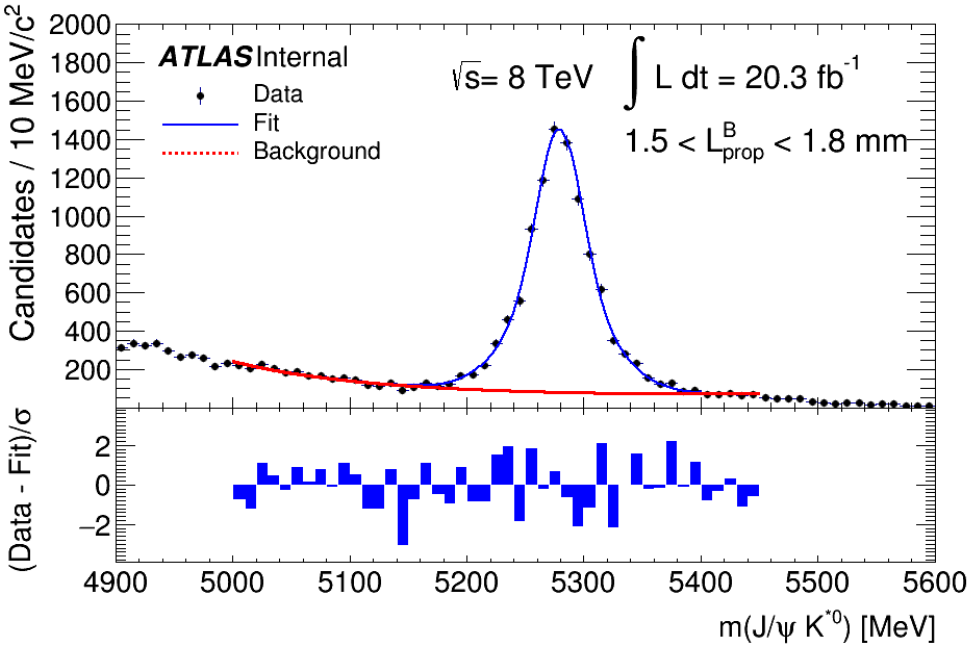

(b)

Figure 7.8: The invariant mass distributions of (a) $B^0 \to J/\psi K_S$ candidates and (b) $B^0 \to J/\psi K^{*0}$ candidates in 2012 for $1.5 < L^B_{\text{prop}} < 1.8$ mm. The full line shows the result of the fit to the function described in the text. The dashed line shows the combinatorial background contribution. The filled area in figure (a) shows the peaking background contribution from the $B^0_s \to J/\psi K_S$ decay. The lower frame of each figure shows the difference between each data point and the fit at that point divided by the statistical uncertainty of the data point.

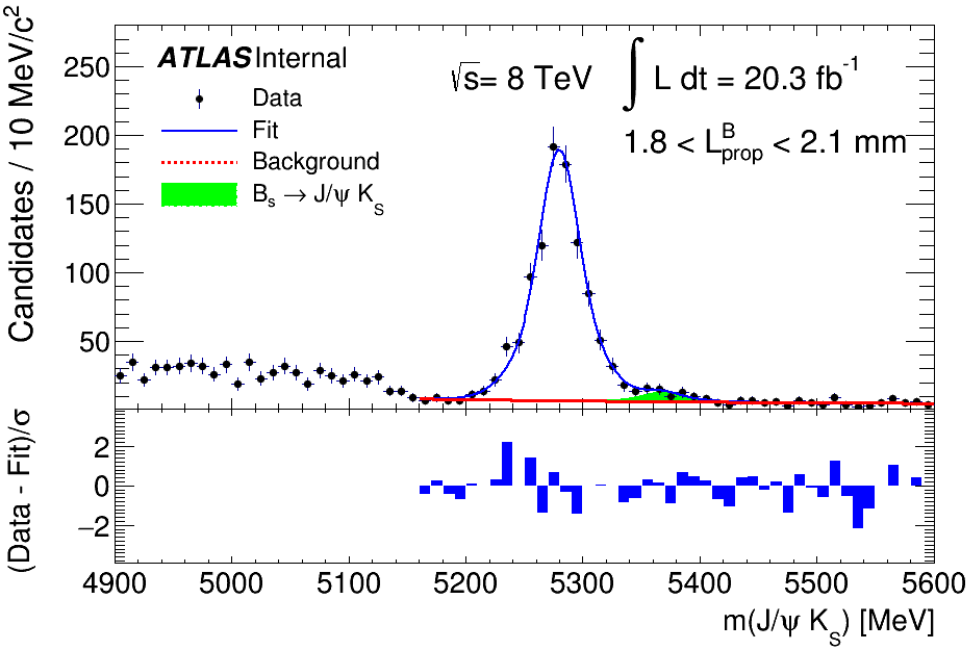

(a)

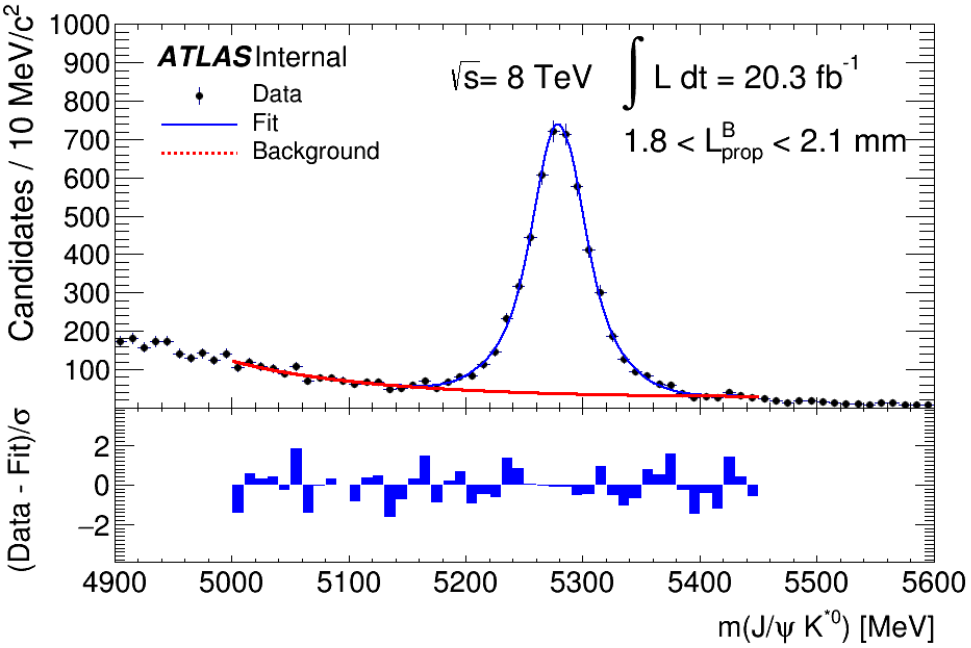

(b)

Figure 7.9: The invariant mass distributions of (a) $B^0 \to J/\psi K_S$ candidates and (b) $B^0 \to J/\psi K^{*0}$ candidates in 2012 for $1.8 < L^B_{\text{prop}} < 2.1$ mm. The full line shows the result of the fit to the function described in the text. The dashed line shows the combinatorial background contribution. The filled area in figure (a) shows the peaking background contribution from the $B^0_s \to J/\psi K_S$ decay. The lower frame of each figure shows the difference between each data point and the fit at that point divided by the statistical uncertainty of the data point.

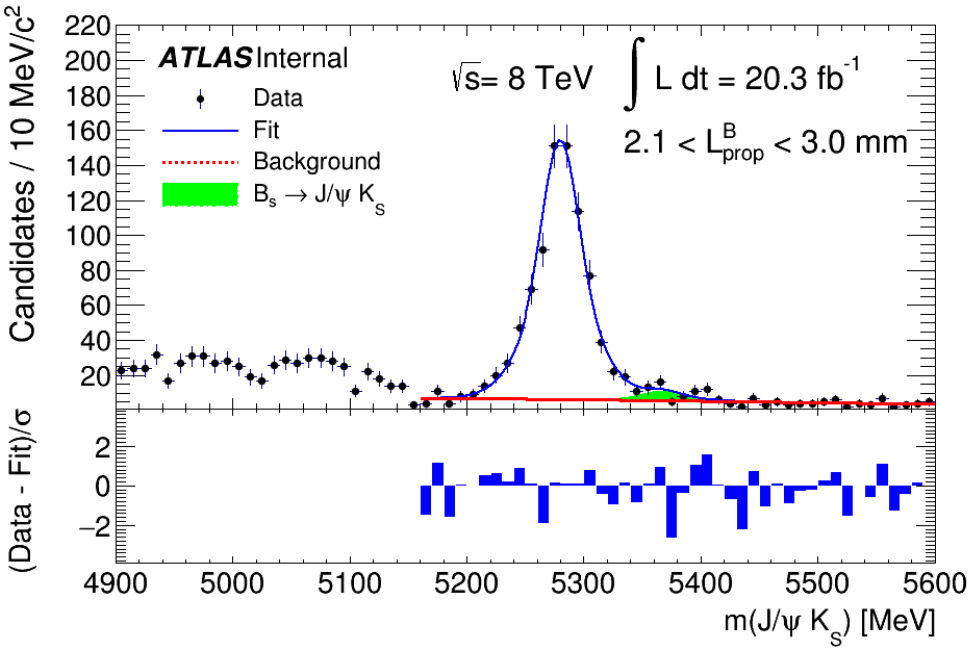

(a)

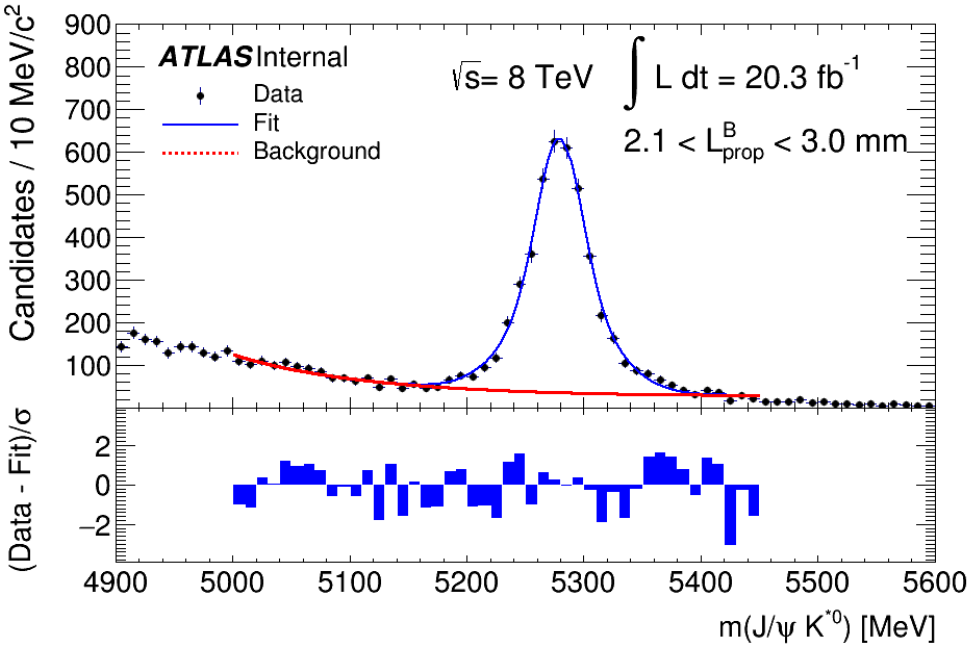

(b)

Figure 7.10: The invariant mass distributions of (a) $B^0 \to J/\psi K_S$ candidates and (b) $B^0 \to J/\psi K^{*0}$ candidates in 2012 for $2.1 < L^B_{\text{prop}} < 3.0$ mm. The full line shows the result of the fit to the function described in the text. The dashed line shows the combinatorial background contribution. The filled area in figure (a) shows the peaking background contribution from the $B^0_s \to J/\psi K_S$ decay. The lower frame of each figure shows the difference between each data point and the fit at that point divided by the statistical uncertainty of the data point.

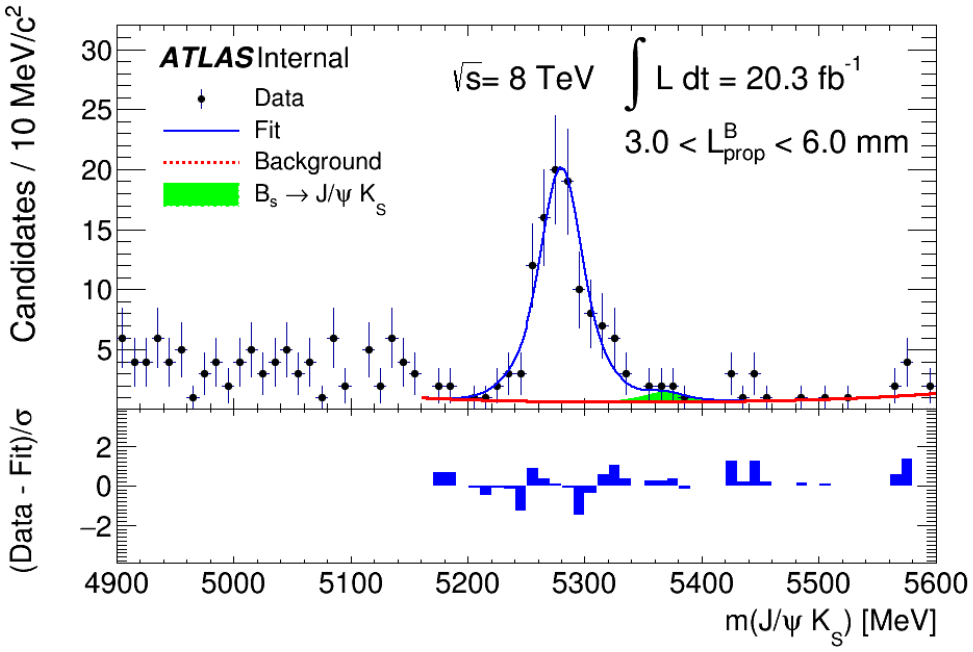

(a)

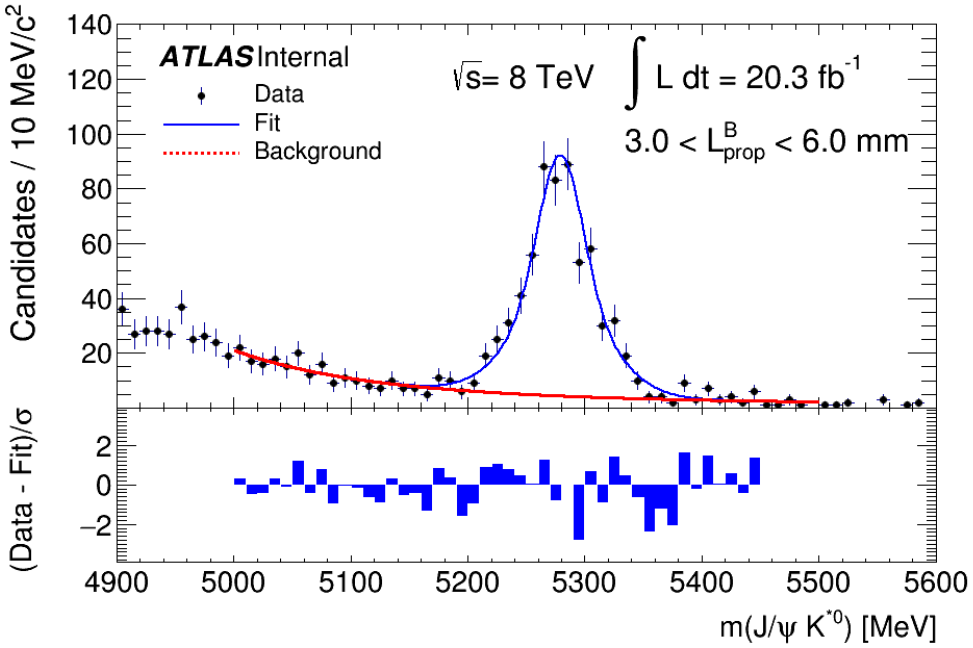

(b)

Figure 7.11: The invariant mass distributions of (a) $B^0 \to J/\psi K_S$ candidates and (b) $B^0 \to J/\psi K^{*0}$ candidates in 2012 for $3.0 < L^B_{\text{prop}} < 6.0$ mm. The full line shows the result of the fit to the function described in the text. The dashed line shows the combinatorial background contribution. The filled area in figure (a) shows the peaking background contribution from the $B^0_s \to J/\psi K_S$ decay. The lower frame of each figure shows the difference between each data point and the fit at that point divided by the statistical uncertainty of the data point.

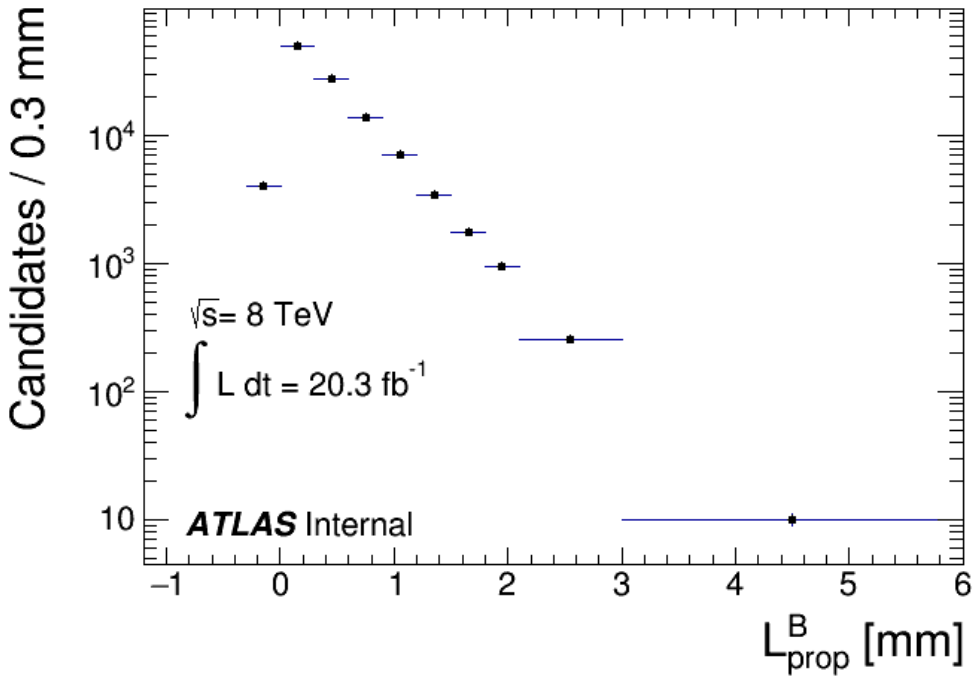

(a)

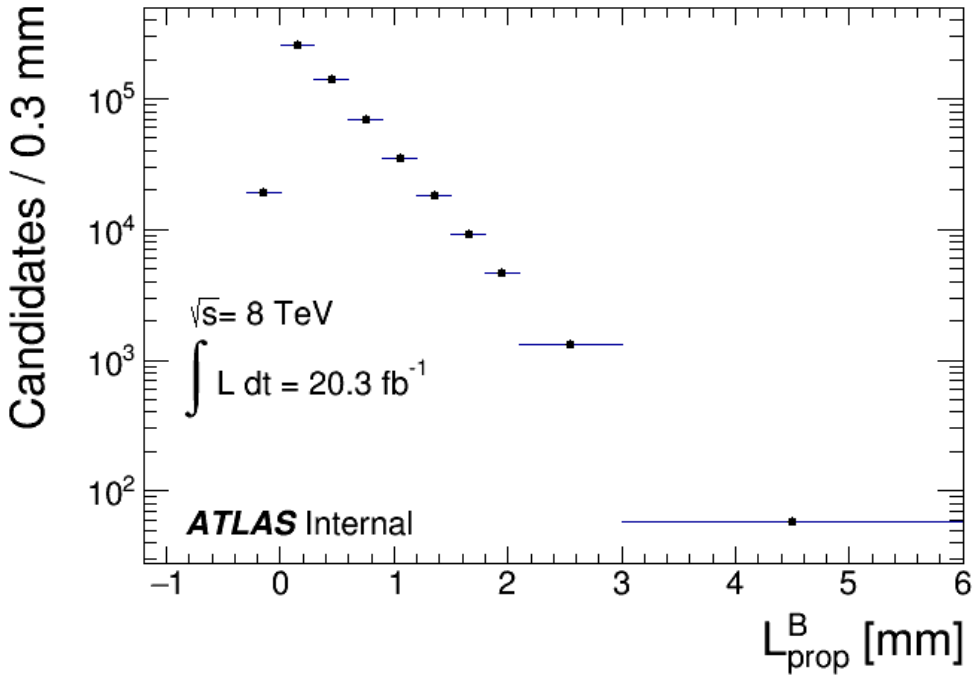

(b)

Figure 7.12: The number of B^0 candidates as a function of the proper decay length of the B^0 meson, L^B_{prop}, for (a) $B^0 \to J/\psi K_S$ and (b) $B^0 \to J/\psi K^{*0}$ decays after event selection in the 2012 data sample. The uncertainties are statistical only.

7.0.1 Verification of mass fits

Tables 7.3 and 7.4 give the $\chi^2/n.d.f.$ and probability (p-value) for each of the fits of the mass distributions. These results confirm an overall good quality of the fit in the individual L^B_{prop} bins.

In the fit of the signal yield in the L^B_{prop} bins, all parameters describing the signal except the normalisation are fixed to the values obtained in the fit of the total sample. The consistency of the fit model in the bins of L^B_{prop} is checked by releasing the width of the first Gaussian function (σ_1) and the scaling factor between the width of the first and second Gaussian functions (s_{12}). A separate check is performed where the mean (μ) of the Gaussian functions is released. Tables 7.5 and 7.6 give the difference between the values of σ_1 and s_{12} from the fit in which they are released and the fit of the total sample. Tables 7.7 - 7.8 give the difference between the value of μ from the fit in which μ is released and the fit of the total sample. For the $B^0 \to J/\psi K_S$ channel, the fit of the total sample gives $\sigma_1 = 15.78 \pm 0.59$ MeV, $s_{12} = 2.18 \pm 0.08$, $\mu = 5280.2 \pm 0.2$ MeV in 2011 and $\sigma_1 = 14.67 \pm 0.42$ MeV, $s_{12} = 2.02 \pm 0.03$, $\mu = 5280.3 \pm 0.1$ MeV in 2012. For the $B^0 \to J/\psi K^{*0}$ channel, the fit of the total sample gives $\sigma_1 = 17.42 \pm 0.57$ MeV, $s_{12} = 2.17 \pm 0.04$, $\mu = 5279.6 \pm 0.2$ MeV in 2011 and $\sigma_1 = 18.51 \pm 0.27$ MeV, $s_{12} = 2.13 \pm 0.02$, $\mu = 5279.5 \pm 0.1$ MeV in 2012. The relative fraction of the first Gaussian (f_1) is, for the $B^0 \to J/\psi K_S$ channel, $f_1 = 0.541 \pm 0.044$ for the 2011 sample and $f_1 = 0.427 \pm 0.030$ for the 2012 sample. For the $B^0 \to J/\psi K^{*0}$ channel, $f_1 = 0.371 \pm 0.028$ for 2011 and $f_1 = 0.424 \pm 0.015$ for 2012. The fraction of the second Gaussian in the fit is equal to $1 - f_1$. The performed study confirms the validity of the adopted fitting procedure since a very good consistency between the released and default values of σ_1, s_{12}, and μ is obtained for all L^B_{prop} bins in both channels.

	2011			2012		
L^B_{prop} range (mm)	$\chi^2/n.d.f.$	p-value	B^0 yield	$\chi^2/n.d.f.$	p-value	B^0 yield
$-0.3 < L^B_{\text{prop}} < 0.0$	48.28/39	0.15	1054 ± 113	50.14/39	0.11	4147 ± 226
$0.0 < L^B_{\text{prop}} < 0.3$	38.90/39	0.47	13090 ± 189	44.37/39	0.26	51520 ± 367
$0.3 < L^B_{\text{prop}} < 0.6$	30.01/39	0.85	7228 ± 107	37.21/39	0.52	28430 ± 211
$0.6 < L^B_{\text{prop}} < 0.9$	39.69/39	0.44	3638 ± 73	53.64/39	0.06	14310 ± 142
$0.9 < L^B_{\text{prop}} < 1.2$	41.87/39	0.35	1832 ± 51	31.96/39	0.78	7206 ± 99
$1.2 < L^B_{\text{prop}} < 1.5$	35.25/39	0.64	900 ± 36	44.17/39	0.26	3539 ± 68
$1.5 < L^B_{\text{prop}} < 1.8$	34.14/39	0.69	456 ± 25	39.55/39	0.45	1792 ± 48
$1.8 < L^B_{\text{prop}} < 2.1$	50.94/39	0.10	246 ± 17	29.99/39	0.85	966 ± 35
$2.1 < L^B_{\text{prop}} < 3.0$	26.32/39	0.94	201 ± 17	39.99/39	0.43	787 ± 32
$3.0 < L^B_{\text{prop}} < 6.0$	14.62/39	1.00	27 ± 7	30.35/39	0.84	107 ± 11

Table 7.3: $\chi^2/n.d.f.$, p-value and B^0 yield for the fits to the mass distributions in each L^B_{prop} bin for the $B^0 \to J/\psi K_S$ channel.

	2011			2012		
L^B_{prop} range (mm)	$\chi^2/n.d.f.$	p-value	B^0 yield	$\chi^2/n.d.f.$	p-value	B^0 yield
$-0.3 < L^B_{\text{prop}} < 0.0$	33.55/41	0.79	4535 ± 512	37.75/41	0.62	19510 ± 1063
$0.0 < L^B_{\text{prop}} < 0.3$	40.61/41	0.49	59950 ± 681	57.80/41	0.04	257900 ± 1413
$0.3 < L^B_{\text{prop}} < 0.6$	32.45/41	0.83	32870 ± 253	30.21/41	0.89	141400 ± 524
$0.6 < L^B_{\text{prop}} < 0.9$	49.26/41	0.18	16550 ± 157	69.39/41	0.01	71180 ± 326
$0.9 < L^B_{\text{prop}} < 1.2$	43.81/41	0.35	8396 ± 108	58.84/41	0.04	36120 ± 224
$1.2 < L^B_{\text{prop}} < 1.5$	43.13/41	0.38	4319 ± 78	45.65/41	0.28	18580 ± 159
$1.5 < L^B_{\text{prop}} < 1.8$	41.69/41	0.44	2193 ± 54	64.72/41	0.01	9432 ± 112
$1.8 < L^B_{\text{prop}} < 2.1$	69, 94/41	0.03	1118 ± 38	33.99/41	0.77	4809 ± 79
$2.1 < L^B_{\text{prop}} < 3.0$	36.54/41	0.67	949 ± 36	60.58/41	0.02	4082 ± 74
$3.0 < L^B_{\text{prop}} < 6.0$	29.34/46	0.97	139 ± 13	59.27/46	0.09	598 ± 28

Table 7.4: $\chi^2/n.d.f.$ and p-value for the fits to the mass distributions in each L^B_{prop} bin for the $B^0 \to J/\psi K^{*0}$ channel.

	2011		2012	
L^B_{prop}range (mm)	$\Delta\sigma_1$ (MeV)	Δs_{12}	$\Delta\sigma_1$ (MeV)	Δs_{12}
$-0.3 < L^B_{\text{prop}} < 0.0$	$+5.82 \pm 3.96$	$+0.46 \pm 2.20$	$+3.76 \pm 1.79$	-0.51 ± 1.05
$0.0 < L^B_{\text{prop}} < 0.3$	$+0.25 \pm 0.44$	-0.07 ± 0.10	-0.04 ± 0.35	$+0.01 \pm 0.05$
$0.3 < L^B_{\text{prop}} < 0.6$	-0.38 ± 0.46	$+0.05 \pm 0.08$	$+0.25 \pm 0.33$	-0.06 ± 0.05
$0.6 < L^B_{\text{prop}} < 0.9$	-0.21 ± 0.34	$+0.05 \pm 0.11$	$+0.13 \pm 0.27$	$+0.00 \pm 0.06$
$0.9 < L^B_{\text{prop}} < 1.2$	-0.51 ± 0.36	$+0.02 \pm 0.17$	$+0.12 \pm 0.16$	-0.03 ± 0.08
$1.2 < L^B_{\text{prop}} < 1.5$	$+0.29 \pm 0.68$	$+0.07 \pm 0.27$	-0.68 ± 0.14	$+0.04 \pm 0.14$
$1.5 < L^B_{\text{prop}} < 1.8$	-0.03 ± 1.34	-0.09 ± 0.31	$+0.17 \pm 0.77$	$+0.06 \pm 0.19$
$1.8 < L^B_{\text{prop}} < 2.1$	-0.95 ± 1.41	$+1.30 \pm 0.61$	$+0.33 \pm 1.23$	$+0.03 \pm 0.26$
$2.1 < L^B_{\text{prop}} < 3.0$	$+0.07 \pm 2.27$	$+0.07 \pm 0.49$	$+0.25 \pm 1.33$	$+0.03 \pm 0.28$
$3.0 < L^B_{\text{prop}} < 6.0$	$+4.81 \pm 5.94$	-0.27 ± 0.86	$+1.57 \pm 4.64$	-0.22 ± 0.75

Table 7.5: Change in σ_1 and s_{12} between the fit in which they are released and the default fit for the $B^0 \to J/\psi K_S$ channel.

	2011		2012	
L^B_{prop} range (mm)	$\Delta\sigma_1$ (MeV)	Δs_{12}	$\Delta\sigma_1$ (MeV)	Δs_{12}
$-0.3 < L^B_{\text{prop}} < 0.0$	$+1.06 \pm 3.45$	$+1.15 \pm 0.84$	$+2.54 \pm 2.03$	$+0.37 \pm 0.54$
$0.0 < L^B_{\text{prop}} < 0.3$	-0.32 ± 0.40	$+0.05 \pm 0.10$	-0.03 ± 0.17	-0.05 ± 0.06
$0.3 < L^B_{\text{prop}} < 0.6$	$+0.34 \pm 0.49$	-0.04 ± 0.04	-0.11 ± 0.23	-0.01 ± 0.02
$0.6 < L^B_{\text{prop}} < 0.9$	$+0.40 \pm 0.42$	-0.06 ± 0.06	$+0.11 \pm 0.20$	-0.02 ± 0.02
$0.9 < L^B_{\text{prop}} < 1.2$	-0.46 ± 0.21	-0.02 ± 0.08	-0.14 ± 0.12	-0.04 ± 0.06
$1.2 < L^B_{\text{prop}} < 1.5$	$+0.12 \pm 0.59$	-0.01 ± 0.14	-0.44 ± 0.19	$+0.08 \pm 0.06$
$1.5 < L^B_{\text{prop}} < 1.8$	-0.27 ± 0.76	$+0.19 \pm 0.18$	$+0.00 \pm 0.38$	$+0.06 \pm 0.08$
$1.8 < L^B_{\text{prop}} < 2.1$	-0.70 ± 1.19	$+0.37 \pm 0.28$	$+0.29 \pm 0.60$	-0.03 ± 0.11
$2.1 < L^B_{\text{prop}} < 3.0$	-2.80 ± 1.08	$+0.50 \pm 0.27$	-0.80 ± 0.59	$+0.15 \pm 0.13$
$3.0 < L^B_{\text{prop}} < 6.0$	$+1.22 \pm 2.69$	$+0.74 \pm 0.51$	$+4.93 \pm 3.72$	-0.61 ± 0.43

Table 7.6: Change in σ_1 and s_{12} between the fit in which they are released and the default fit for the $B^0 \to J/\psi K^{*0}$ channel.

	2011	2012
L^B_{prop} range (mm)	$\Delta\mu$ (MeV)	$\Delta\mu$ (MeV)
$-0.3 < L^B_{\text{prop}} < 0.0$	$+0.6 \pm 2.9$	-1.8 ± 1.2
$0.0 < L^B_{\text{prop}} < 0.3$	-0.3 ± 0.2	-0.3 ± 0.2
$0.3 < L^B_{\text{prop}} < 0.6$	$+0.2 \pm 0.2$	$+0.0 \pm 0.2$
$0.6 < L^B_{\text{prop}} < 0.9$	$+0.0 \pm 0.3$	-0.4 ± 0.2
$0.9 < L^B_{\text{prop}} < 1.2$	-0.7 ± 0.6	$+0.4 \pm 0.3$
$1.2 < L^B_{\text{prop}} < 1.5$	$+1.0 \pm 0.9$	-0.7 ± 0.4
$1.5 < L^B_{\text{prop}} < 1.8$	$+2.4 \pm 1.2$	$+0.0 \pm 0.6$
$1.8 < L^B_{\text{prop}} < 2.1$	-2.4 ± 1.7	-1.4 ± 0.9
$2.1 < L^B_{\text{prop}} < 3.0$	-0.1 ± 1.8	$+0.2 \pm 1.0$
$3.0 < L^B_{\text{prop}} < 6.0$	$+5.3 \pm 4.6$	-0.8 ± 2.5

Table 7.7: Change in μ between the fit in which it is released and the default fit for the $B^0 \to J/\psi K_S$ channel. Values are given in MeV.

	2011	2012
L^B_{prop} range (mm)	$\Delta\mu$ (MeV)	$\Delta\mu$ (MeV)
$-0.3 < L^B_{\text{prop}} < 0.0$	-5.2 ± 3.6	-4.5 ± 2.2
$0.0 < L^B_{\text{prop}} < 0.3$	-0.3 ± 0.3	-0.1 ± 0.2
$0.3 < L^B_{\text{prop}} < 0.6$	$+0.2 \pm 0.2$	$+0.2 \pm 0.2$
$0.6 < L^B_{\text{prop}} < 0.9$	$+0.3 \pm 0.3$	-0.5 ± 0.2
$0.9 < L^B_{\text{prop}} < 1.2$	$+0.0 \pm 0.6$	-0.1 ± 0.3
$1.2 < L^B_{\text{prop}} < 1.5$	-0.2 ± 0.9	-0.7 ± 0.4
$1.5 < L^B_{\text{prop}} < 1.8$	-1.3 ± 1.2	-1.0 ± 0.5
$1.8 < L^B_{\text{prop}} < 2.1$	-0.8 ± 1.7	-0.5 ± 0.7
$2.1 < L^B_{\text{prop}} < 3.0$	-1.9 ± 1.5	-0.9 ± 0.8
$3.0 < L^B_{\text{prop}} < 6.0$	$+1.7 \pm 4.1$	-3.5 ± 2.2

Table 7.8: Change in μ between the fit in which it is released and the default fit for the $B^0 \to J/\psi K^{*0}$ channel. Values are given in MeV.

7.0.2 Triggers

If any of the triggers used in this analysis have a proper decay length dependence, an additional bias in the distributions of L^B_{prop} could be introduced. This section describes the study of the triggers used to identify whether any such L^B_{prop} bias is present.

The fraction of events in the final sample selected by a given trigger for each channel in the 2011 and 2012 data and MC samples is shown in tables 7.9 to 7.12. The naming convention for the triggers is as following. The label "EF" stands for the Event Filter, which is described in Section 4.7. The tag "Jpsimumu" indicates that the trigger requires a $\mu^+\mu^-$ pair that originate from a common vertex and have an invariant mass close to the J/ψ mass (2.5 GeV $< m_{\mu\mu} <$ 4.3 GeV). The tags "mu10" and "mu4" signify that at least one of the muons must have transverse momentum greater than, respectively, 10 GeV or 4 GeV. The "2mu4" and "2mu6" tags indicate that both muons have transverse momentum greater than 4 or 6 GeV respectively, and the "mu4mu6" tag means that one muon has transverse momentum greater than 6 GeV and the other has transverse momentum greater than 4 GeV. The addition of a "T" in these labels signifies that the 4 GeV transverse momentum requirement was applied at L1 (defined in Section 4.7).

The fractions for the $B^0 \to J/\psi K_S$ channel are approximately the same as those for the $B^0 \to J/\psi K^{*0}$ channel, which is expected as the triggers are applied to the muons from the J/ψ decay. Additionally, the trigger fractions are similar enough in data and Monte-Carlo that no prescale is required.

Trigger	Fraction (%)	
	Data	MC
EF_mu10_Jpsimumu	20.39	28.40
EF_mu4_Jpsimumu	46.26	59.96
EF_2mu4_Jpsimumu	43.85	33.48
EF_2mu4T_Jpsimumu	44.03	34.87
EF_mu4Tmu6_Jpsimumu	32.07	28.38

Table 7.9: Trigger fractions for $B^0 \to J/\psi K_S$ in 2011.

The data taken in periods A1-C5 of 2012 was affected by a problem with the level 2 trigger suite used during these periods known as "L2StarA",

Trigger	Fraction (%)	
	Data	MC
EF_mu10_Jpsimumu	23.68	29.86
EF_mu4_Jpsimumu	45.35	61.98
EF_2mu4_Jpsimumu	42.83	30.33
EF_2mu4T_Jpsimumu	43.71	31.71
EF_mu4Tmu6_Jpsimumu	31.61	23.92

Table 7.10: Trigger fractions for $B^0 \to J/\psi K^{*0}$ in 2011.

Trigger	Fraction (%)	
	Data	MC
EF_2mu4T_Jpsimumu	85.70	90.01
EF_2mu4T_Jpsimumu_Barrel	60.12	50.81
EF_2mu4T_Jpsimumu_BarrelOnly	50.44	42.50
EF_mu4Tmu6_Jpsimumu	67.84	70.57
EF_mu4Tmu6_Jpsimumu_Barrel	41.39	38.78
EF_2mu6_Jpsimumu	24.08	25.40
EF_2mu4T_Jpsimumu_L2StarB	58.58	87.85
EF_2mu4T_Jpsimumu_Barrel_L2StarB	42.48	56.56
EF_2mu4T_Jpsimumu_BarrelOnly_L2StarB	39.92	50.30
EF_mu4Tmu6_Jpsimumu_L2StarB	50.89	69.03
EF_mu4Tmu6_Jpsimumu_Barrel_L2StarB	31.43	43.69
EF_2mu6_Jpsimumu_L2StarB	17.36	26.82

Table 7.11: Trigger fractions for $B^0 \to J/\psi K_S$ in 2012.

which resulted in a loss of reconstruction efficiency in events where the muons produced by the decay of a J/ψ meson have a large transverse impact parameter $d_0(\mu)$. This caused a decrease in efficiency dependent on the proper decay length of the B^0 meson which would have introduced a bias in the measurement of L^B_{prop}. However, the adopted measurement method ensures that this bias does not affect the value of $\Delta\Gamma_d/\Gamma_d$. Both $B^0 \to J/\psi K_S$ and $B^0 \to J/\psi K^{*0}$ events are triggered by the muons from the J/ψ decay. Therefore, the bias in the L^B_{prop} distribution should be the same for both channels and should cancel when the ratio of the two distributions is taken.

Figure 7.13 compares the L^B_{prop} distributions for $B^0 \to J/\psi K_S$ and $B^0 \to$

Trigger	Fraction (%)	
	Data	MC
EF_2mu4T_Jpsimumu	86.49	90.46
EF_2mu4T_Jpsimumu_Barrel	59.12	48.96
EF_2mu4T_Jpsimumu_BarrelOnly	50.04	41.02
EF_mu4Tmu6_Jpsimumu	68.96	71.06
EF_mu4Tmu6_Jpsimumu_Barrel	40.63	37.40
EF_2mu6_Jpsimumu	27.99	26.56
EF_2mu4T_Jpsimumu_L2StarB	58.58	87.34
EF_2mu4T_Jpsimumu_Barrel_L2StarB	41.13	53.68
EF_2mu4T_Jpsimumu_BarrelOnly_L2StarB	39.19	48.22
EF_mu4Tmu6_Jpsimumu_L2StarB	50.53	69.40
EF_mu4Tmu6_Jpsimumu_Barrel_L2StarB	30.20	41.93
EF_2mu6_Jpsimumu_L2StarB	19.97	28.21

Table 7.12: Trigger fractions for $B^0 \to J/\psi K^{*0}$ in 2012.

$J/\psi K^{*0}$ events taken with the L2StarA and L2StarB triggers. Figure 7.14 shows the ratio of the L^B_{prop} distributions for events taken with the two different triggers. The sensitivity of the L^B_{prop} distributions to the trigger in the individual B^0 decay channels is clearly visible. However, the ratio of the $B^0 \to J/\psi K_S$ distribution to the $B^0 \to J/\psi K^{*0}$ distribution does not show any statistically significant L^B_{prop} dependence. This ratio is presented in Fig. 7.15 together with the result of the fit by a first order polynomial. The fit to the ratio obtained from data has $\chi^2/n.d.f. = 2.17/7$ and a slope of $(-0.85 \pm 1.58) \times 10^{-2}$. In Monte-Carlo, the ratio has $\chi^2/n.d.f. = 1.54/7$ and a slope of $(-0.43 \pm 0.57) \times 10^{-2}$. The slope is consistent with zero within the statistical uncertainty in both data and MC. This study therefore clearly indicates that the proper decay length bias of the triggers does not affect the ratio of the L^B_{prop} distributions and therefore does not influence the measurement of $\Delta\Gamma_d/\Gamma_d$.

Since the L^B_{prop} bias of the triggers is caused by an unexpected $d_0(\mu)$ dependence, the distributions of $d_0(\mu)$ produced using the L2StarA and L2StarB triggers should also be compared. This comparison for both B^0 channels is shown in Fig. 7.16. The ratio of the $d_0(\mu)$ distributions for the two triggers is shown in Fig. 7.17. The trigger dependence of $d_0(\mu)$ distri-

butions in each channel is clear. The $d_0(\mu)$ the ratio of the $B^0 \to J/\psi K_S$ distribution to the $B^0 \to J/\psi K^{*0}$ distribution is shown in Fig. 7.18. The fit to this ratio in data by a first order polynomial has $\chi^2/n.d.f. = 4.03/14$ and a slope of $(-0.02 \pm 1.42) \times 10^{-2}$. In Monte Carlo, the fit to the ratio has $\chi^2/n.d.f. = 4.02/16$ and a slope of $(-0.12 \pm 0.39) \times 10^{-2}$. The slope is statistically consistent with zero in both data and MC, which demonstrates that the trigger bias in $d_0(\mu)$ cancels when the ratio of the two B^0 decay channels is taken. Therefore, this trigger bias does not affect the measurement of $\Delta\Gamma_d/\Gamma_d$.

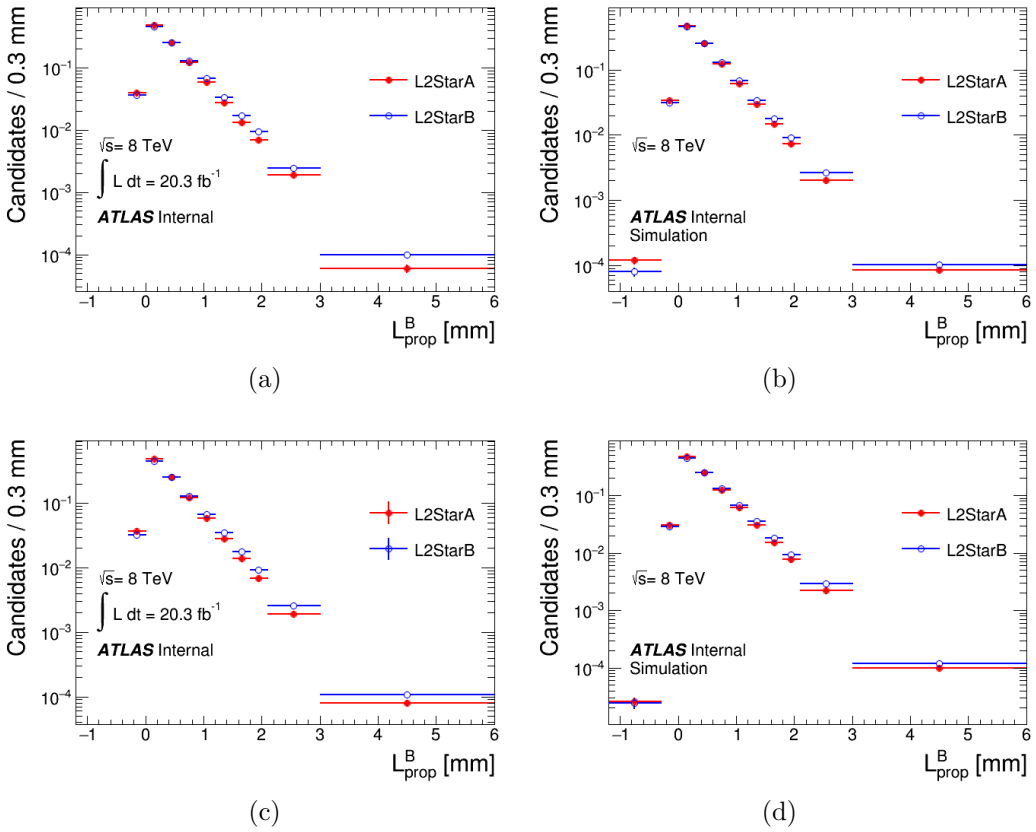

Figure 7.13: Comparison of the L^B_{prop} distributions for the L2StarB and L2StarA triggers for (a,b) $B^0 \to J/\psi K_S$ candidates in data and MC respectively and (c,d) $B^0 \to J/\psi K^{*0}$ candidates in data and MC respectively.

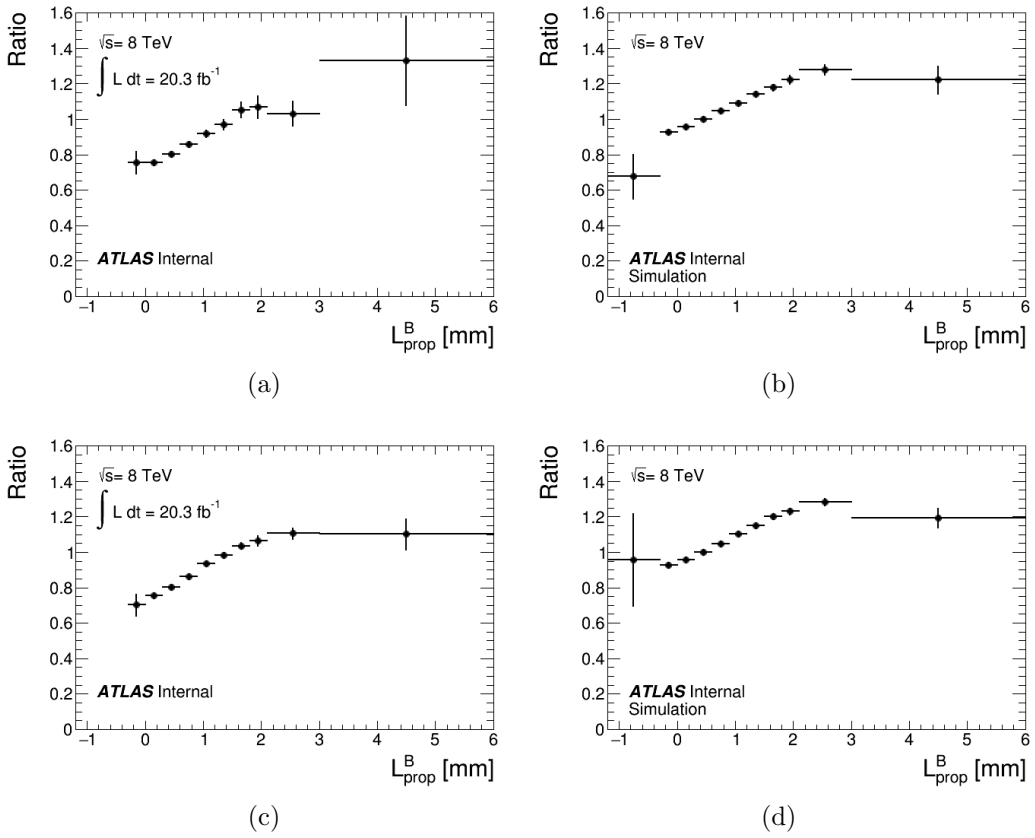

Figure 7.14: Ratio of the L^B_{prop} distributions for the L2StarB and L2StarA triggers for (a,b) $B^0 \to J/\psi K_S$ candidates in data and MC respectively and (c,d) $B^0 \to J/\psi K^{*0}$ candidates in data and MC respectively.

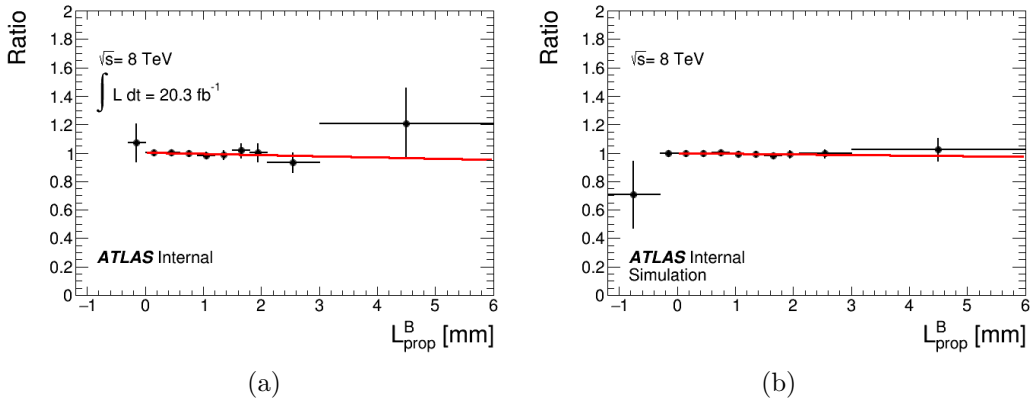

Figure 7.15: Ratio of the $L^B_{\text{prop}}(B^0 \to J/\psi K_S)$ trigger ratio to the $L^B_{\text{prop}}(B^0 \to J/\psi K^{*0})$ trigger ratio in (a) data and (b) MC.

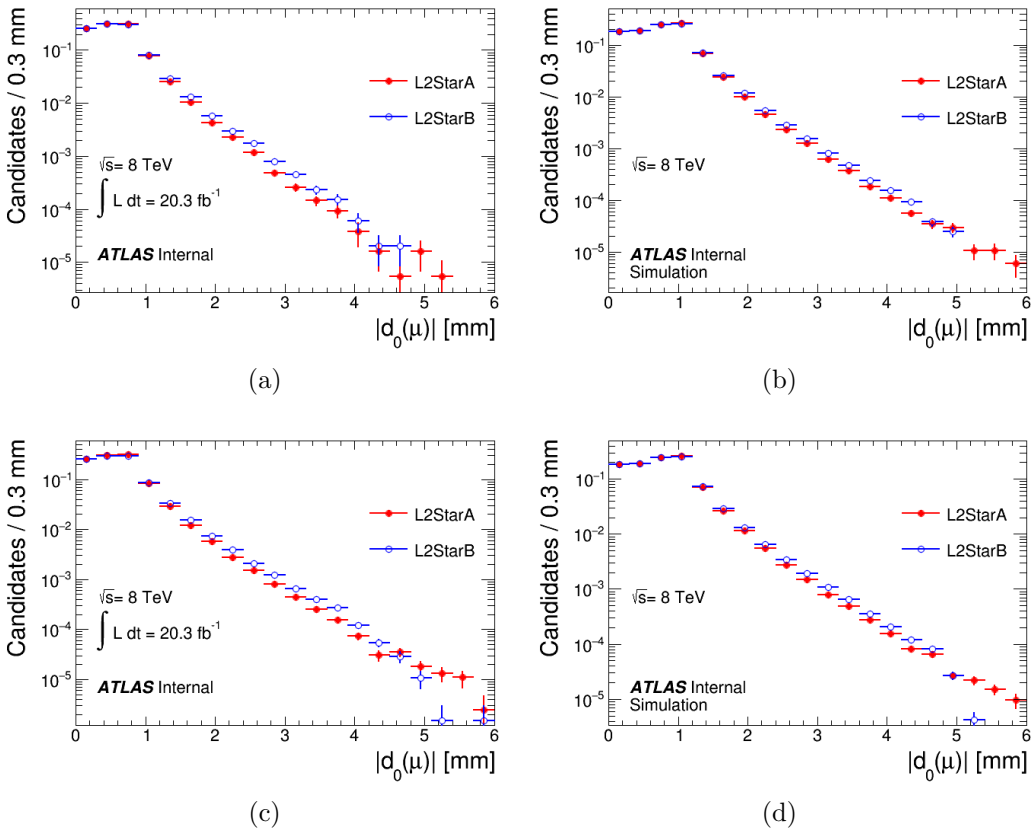

Figure 7.16: Comparison of the $d_0(\mu)$ distributions for the L2StarB and L2StarA triggers for (a,b) $B^0 \to J/\psi K_S$ candidates in data and MC respectively and (c,d) $B^0 \to J/\psi K^{*0}$ candidates in data and MC respectively.

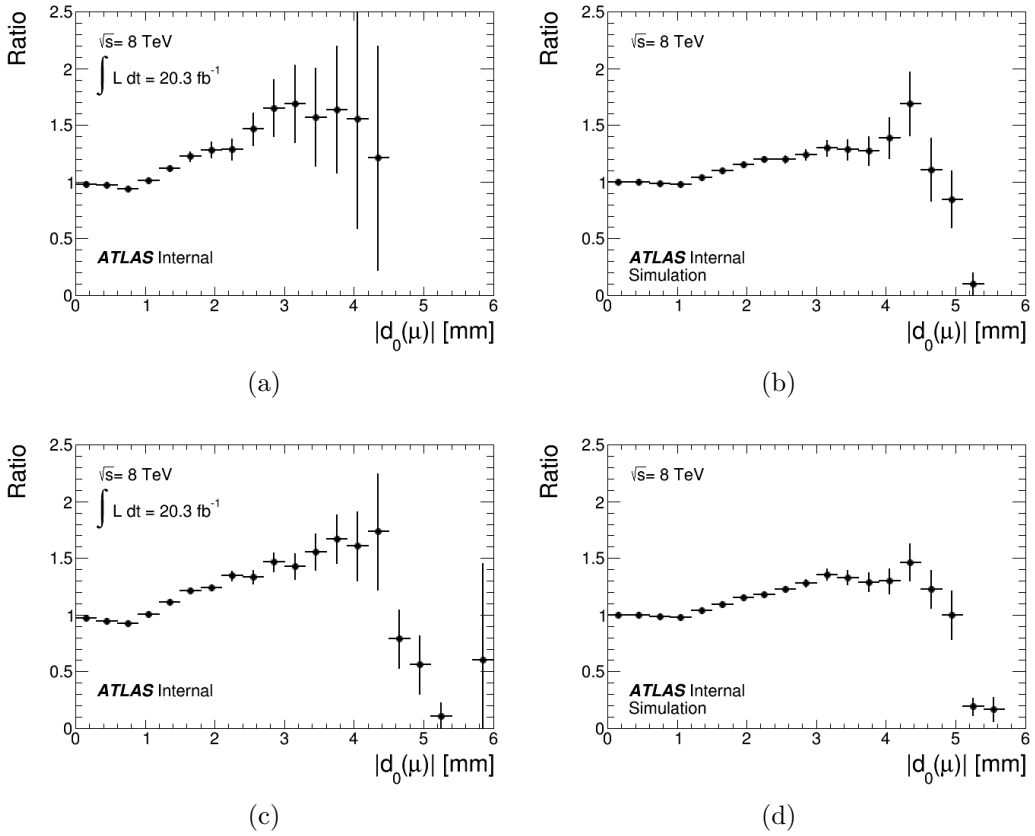

Figure 7.17: Ratio of the $d_0(\mu)$ distributions for the L2StarB and L2StarA triggers for (a,b) $B^0 \to J/\psi K_S$ candidates in data and MC respectively and (c,d) $B^0 \to J/\psi K^{*0}$ candidates in data and MC respectively.

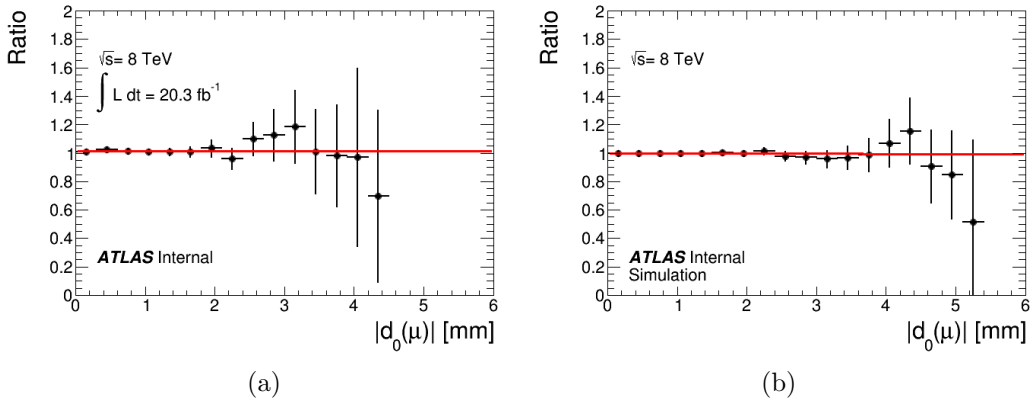

Figure 7.18: Ratio of the $d_0(\mu)(B^0 \to J/\psi K_S)$ trigger ratio to the $d_0(\mu)(B^0 \to J/\psi K^{*0})$ trigger ratio in (a) data and (b) MC.

Chapter 8

The production asymmetry of the B^0 meson

In this chapter, the measurement of the production asymmetry A_P of the B^0 meson is described. This measurement is required for the determination of $\Delta\Gamma_d/\Gamma_d$ as it has not previously been evaluated in the ATLAS experiment.

The time dependent decay rate of $B^0 \to J/\psi K_S$ given by Eq. 2.48 contains a term proportional to the production asymmetry of the B^0 meson. The measured ratio of proper decay length distributions $R(L^B_{\text{prop}})$ defined in Eq. 6.5 therefore also depends on A_P. The expression for A_P is given in Eq. 2.40. Although b quarks are predominantly produced in $b\bar{b}$ pairs, which result in an equal number of b and $\bar{b}$ quarks, the presence of a valence u quark in pp collisions leads to a small excess of B^+ mesons (quark content $\bar{b}u$) over B^- mesons ($b\bar{u}$) [57, 58]. Similarly, there is an excess of $B^0(\bar{b}d)$ mesons over $\bar{B}^0(b\bar{d})$ mesons due to the presence of a valence d quark in the protons. The larger number of B mesons than $\bar{B}$ mesons is compensated for by the excess of b baryons over their corresponding anti-particles. In each case the excess is expected to be of the order of 1%. A value of A_P in pp collisions has been measured by the LHCb experiment [59], but this result is not directly applicable to the conditions of the ATLAS experiment because of the different ranges of pseudorapidities and transverse momenta of the detected B mesons. Therefore, a dedicated measurement of A_{P} is necessary.

The production asymmetry A_{P} of the B^0 meson can be obtained from the time-dependent charge asymmetry of the flavour-specific $B^0 \to J/\psi K^{*0}$

decay. If the initial flavour of the B^0 meson is not determined, the time-dependent rate of the decays $B^0 \to J/\psi K^{*0}$ and $\bar{B}^0 \to J/\psi \bar{K}^{*0}$ are given by Eqs. (2.50) and (2.53) respectively. CP violation in mixing is predicted to be small in the SM and is omitted from these expressions. The terms proportional to $A_{\rm P}$ in Eqs. (2.50) and (2.53) reflect the oscillating component of the $B^0 \to J/\psi K^{*0}$ decay. The corresponding charge asymmetry due to B^0 oscillations in bin i of $L^B_{\rm prop}$, $A_{i,\rm osc}$, is defined as:

$$A_{i,\rm osc} \equiv \frac{\int_{L_i^{\rm min}}^{L_i^{\rm max}} \left(\int_0^\infty G(L^B_{\rm prop} - ct, J/\psi K^{*0})(\Gamma[t, J/\psi K^{*0}] - \Gamma[t, J/\psi \bar{K}^{*0}])\mathrm{d}t\right) \mathrm{d}L^B_{\rm prop}}{\int_{L_i^{\rm min}}^{L_i^{\rm max}} \left(\int_0^\infty G(L^B_{\rm prop} - ct, J/\psi K^{*0})(\Gamma[t, J/\psi K^{*0}] + \Gamma[t, J/\psi \bar{K}^{*0}])\mathrm{d}t\right) \mathrm{d}L^B_{\rm prop}}. \tag{8.1}$$

Here $G(L^B_{\rm prop} - ct, J/\psi K^{*0})$ is the detector resolution of $L^B_{\rm prop}$, as given by Eq. (7.2), for the $B^0 \to J/\psi K^{*0}$ channel. The values of the lower and upper edges of bin i, $L_i^{\rm min}$ and $L_i^{\rm max}$, are given in Table 7.2. Using Eqs. (2.50) and (2.53), $A_{i,\rm osc}$ can be presented as:

$$A_{i,\rm osc} = A_{\rm P} \frac{\int_{L_i^{\rm min}}^{L_i^{\rm max}} \left(\int_0^\infty G(L^B_{\rm prop} - ct, J/\psi K^{*0}) \mathrm{e}^{-\Gamma_d t} \cos(\Delta m_d t)\mathrm{d}t\right) \mathrm{d}L^B_{\rm prop}}{\int_{L_i^{\rm min}}^{L_i^{\rm max}} \left(\int_0^\infty G(L^B_{\rm prop} - ct, J/\psi K^{*0}) \mathrm{e}^{-\Gamma_d t} \cosh \frac{\Delta\Gamma_d t}{2}\mathrm{d}t\right) \mathrm{d}L^B_{\rm prop}}. \tag{8.2}$$

In addition to B^0 oscillations, the asymmetry in the number of $J/\psi K^{*0}$ and $J/\psi \bar{K}^{*0}$ events is also caused by a detector-related asymmetry $A_{\rm det}$ due to differences in the reconstruction of positive and negative particles. The main source of $A_{\rm det}$ is the difference in the interaction cross-section of charged kaons with the detector material, which for momenta below 10 GeV is significantly larger for negative kaons [2]. This difference is due to the additional hyperon production channels in K^--nucleon reactions, which are absent in K^+-nucleon interactions. Thus, positive kaons have a larger probability to pass intact through the active part of the experimental setup and to be detected. In comparison, the charge dependence of the $\pi^\pm$-nucleon interactions is much smaller. Therefore, the observed number of $K^{*0} \to K^+\pi^-$ decays is larger than that of $\bar{K}^{*0} \to K^-\pi^+$, resulting in a positive value of the detector asymmetry $A_{\rm det}$. This effect is independent of the B^0 decay time.

The values of $A_{i,\rm osc}$ and $A_{\rm det}$ are affected by misidentification of the kaon and pion in the $B^0 \to J/\psi K^{*0}$ decay. The observed number of $J/\psi \bar{K}^{*0}$ events, $N(J/\psi \bar{K}^{*0})$, includes genuine $\bar{B}^0 \to J/\psi \bar{K}^{*0}$ and some $B^0 \to J/\psi K^{*0}$

decays. The latter decay contributes because of a wrong assignment of the kaon and pion masses to the two reconstructed charged particles, so that the decay $K^{*0} \to K^+\pi^-$ is identified as a $\bar{K}^{*0} \to K^-\pi^+$. The mistag fraction W quantifies this wrong contribution to the $J/\psi\bar{K}^{*0}$ sample. It is defined as the fraction of true $B^0 \to J/\psi K^{*0}$ decays in $N(J/\psi\bar{K}^{*0})$:

$$W = \frac{N(B^0 \to J/\psi K^{*0})}{N(J/\psi\bar{K}^{*0})}. \tag{8.3}$$

Similarly, the quantity $\bar{W}$ quantifies the fraction of true $B^0 \to J/\psi\bar{K}^{*0}$ decays in the observed number of $J/\psi K^{*0}$ events, $N(J/\psi K^{*0})$:

$$\bar{W} = \frac{N(\bar{B}^0 \to J/\psi\bar{K}^{*0})}{N(J/\psi K^{*0})}. \tag{8.4}$$

The mistag fractions are determined in simulation. The obtained values are:

$$W = \bar{W} = 0.12 \pm 0.02. \tag{8.5}$$

The simulation confirms that the mistag fraction is the same for $B^0 \to J/\psi K^{*0}$ and $\bar{B}^0 \to J/\psi\bar{K}^{*0}$ decays within the statistical uncertainty of 0.4% determined by the number of MC events. Figure 8.1 shows the values of W and $\bar{W}$ computed in the bins of $L^B_{\rm prop}$ defined in Table 7.2. The distribution is fitted by a constant and have $\chi^2/n.d.f. = 2.30/8$ and $\chi^2/n.d.f. = 12.18/8$ respectively, which demonstrates that the mistag fraction does not depend on the B^0 decay time. The systematic uncertainty in the difference of the mistag fraction for $B^0 \to J/\psi K^{*0}$ and $\bar{B}^0 \to J/\psi\bar{K}^{*0}$ decays cancels to large extent. Therefore, the same value of the mistag fraction applies for $N(J/\psi\bar{K}^{*0})$ and $N(J/\psi K^{*0})$ and W will be used for both.

The systematic uncertainty of W is much larger than the statistical uncertainty. Therefore, the given uncertainty of W is systematic only. It takes into account possible variations of the MC simulation which describe B^0 production and decay. The impact of the systematic uncertainty in the value of W on the measurement of $\Delta\Gamma_d$ is very small and is discussed in Section 9.3.

Using the above information, the expected charge asymmetry in bin i of

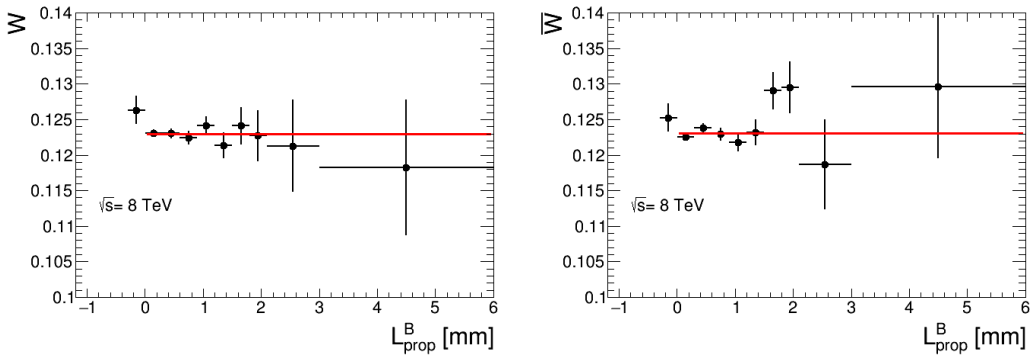

(a) (b)

Figure 8.1: Mistag fractions W and $\bar{W}$ in bins of $L^B_{\rm prop}$. The solid line shows the fit to the distributions by a constant.

$L^B_{\rm prop}$, $A_{i,\rm exp}$, can be expressed as:

$$A_{i,\rm exp} = (A_{\rm det} + A_{i,\rm osc})\,(1 - 2W). \tag{8.6}$$

Here the factor $1-2W$ takes into account the contribution of wrongly identified B^0 decays, which is the same for both $A_{\rm det}$ and $A_{i,\rm osc}$. The second-order terms proportional to $A_{\rm det}A_{\rm P}$ are of the order of 10^{-4} and are neglected in this expression.

The observed charge asymmetry, $A_{i,\rm obs}$, is defined as:

$$A_{i,\rm obs} \equiv \frac{N_i(J/\psi K^{*0}) - N_i(J/\psi \bar{K}^{*0})}{N_i(J/\psi K^{*0}) + N_i(J/\psi \bar{K}^{*0})}. \tag{8.7}$$

Figure 8.2 shows the asymmetry $A_{\rm obs}$ as a function of $L^B_{\rm prop}$ for the 2011 and 2012 samples combined together. The result of the fit to Eq. (8.6) is superimposed. The asymmetry $A_{\rm P}$ is obtained from a χ^2 minimisation:

$$\chi^2[A_{\rm det}, A_{\rm P}] = \sum_{i=2}^{10} \frac{(A_{i,\rm obs} - A_{i,\rm exp})^2}{\sigma_i^2}. \tag{8.8}$$

The free parameters in the fit are $A_{\rm det}$ and $A_{\rm P}$. The values σ_i are the statistical uncertainties of $A_{i,\rm obs}$. The fit has a χ^2 of 6.50 per seven degrees of freedom. The first bin of $L^B_{\rm prop}$ corresponds to a negative decay length due

to the detector resolution. It is not included in this sum as it is affected more than the other data points by systematic uncertainties. Ignoring it has a negligible impact on the uncertainty of this measurement. The fit yields the following values for the asymmetries:

$$A_{\text{det}} = (+1.33 \pm 0.24 \pm 0.30) \times 10^{-2}. \quad (8.9)$$

$$A_{\text{P}} = (+0.25 \pm 0.48 \pm 0.05) \times 10^{-2}. \quad (8.10)$$

The first uncertainty of A_{P} and A_{det} is statistical and the second is due to the uncertainties in the mistag fraction and in the deviations of $|q/p|$ from unity (see Eq. (2.17)). If $|q/p|$ is not unity then Eqs. 2.50 and 2.53 both contain two additional terms dependent on $a/2 = \frac{1}{2}(1 - |q/p|^2) = (-0.05 \pm 0.11) \times 10^{-2}$ [6]. The large relative uncertainty of $a/2$ thus has a non-trivial effect on the measurement of A_{P} and A_{det} and is therefore included in the uncertainty. It is important to note that the uncertainty of $a/2$ does not affect the measurement of $\Delta\Gamma_d/\Gamma_d$ because the term of Eq. 2.48 from which $\Delta\Gamma_d/\Gamma_d$ is determined is proportional to $1 + a/2$ and $a \ll 1$. The systematic uncertainty of A_{det} also contains a contribution from the possible difference between the mistag fractions of the $B^0 \to J/\psi K^{*0}$ and $\bar{B}^0 \to J/\psi \bar{K}^{*0}$ decays. This measurement of the B^0 production asymmetry A_{P} for $p_{\text{T}}(B^0) > 10$ GeV and $|\eta(B^0)| < 2.5$ is consistent with zero. It is also consistent with the LHCb result $A_{\text{P}} = (-0.36 \pm 0.76 \pm 0.28) \times 10^{-2}$ [59] obtained for $4 < p_{\text{T}}(B^0) < 30$ GeV and $2.5 < \eta(B^0) < 4.0$. The measured value of A_{P} given in Eq. (8.10) is used for the extraction of the width difference $\Delta\Gamma_d$.

As a cross-check, a separate evaluation of the detector asymmetry is made from the difference between the reconstruction efficiencies of $B^0 \to J/\psi \bar{K}^{*0}$ and $\bar{B}^0 \to J/\psi \bar{K}^{*0}$ in simulation, denoted by $\epsilon(B^0)$ and $\epsilon(\bar{B}^0)$ respectively. For this determination, the detector asymmetry is given by:

$$A_{\text{det}}(\text{MC}) = \frac{\epsilon(\text{B}^0) - \epsilon(\bar{\text{B}}^0)}{\epsilon(\text{B}^0) + \epsilon(\bar{\text{B}}^0)} \quad (8.11)$$

The obtained value is $A_{\text{det}}(\text{MC}) = (+1.74 \pm 0.03) \times 10^{-2}$, which is consistent with the value obtained in data (Eq. (8.9)).

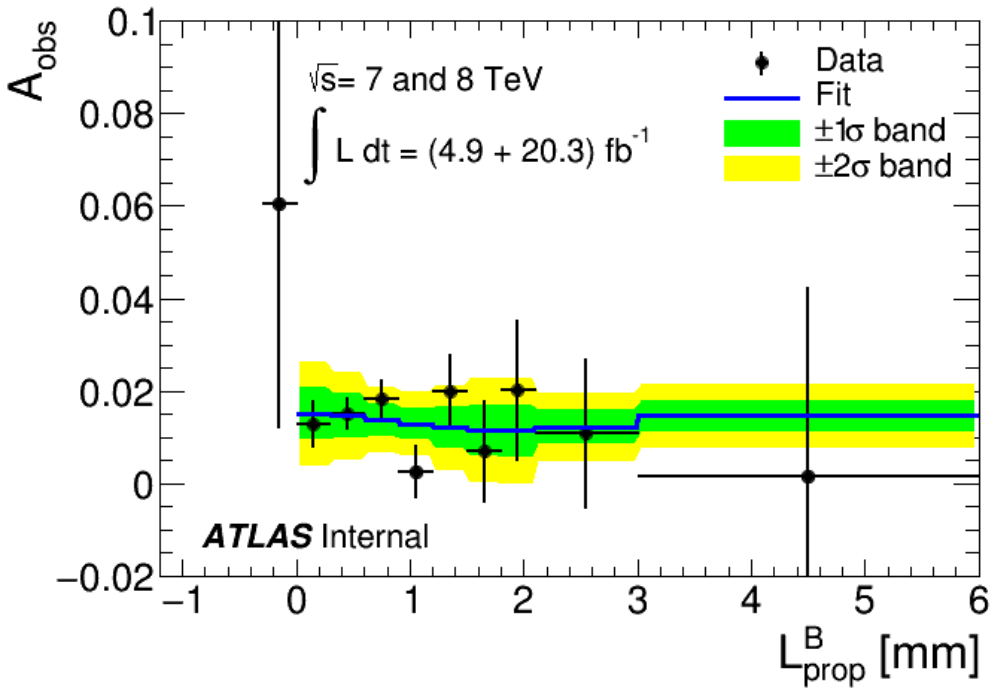

Figure 8.2: Observed charge asymmetry $A_{\rm obs}$ in $B^0 \to J/\psi K^{*0}$ decays measured as a function of the proper decay length of the B^0 meson ($L^B_{\rm prop}$). The line shows the asymmetry $A_{\rm exp}$ obtained from fitting Eq. (8.6) to the data. The first point corresponding to negative proper decay length is not used in the fit. The error bands correspond to the combination of uncertainties obtained by the fit for the production asymmetry $A_{\rm P}$ and the detector asymmetry $A_{\rm det}$.

Chapter 9

The measurement of $\Delta\Gamma_d/\Gamma_d$

This chapter describes the method by which the value of $\Delta\Gamma_d/\Gamma_d$ is measured. The examination of the systematic uncertainties is also included, as well as the final results of the analysis.

9.1 Ratio of efficiencies

As explained in Section 6.5, the ratio $R_{i,\text{exp}}(L^B_{\text{prop}})$ should be corrected by the lifetime-dependent ratio of efficiencies $R_{i,\text{eff}}(L^B_{\text{prop}})$ defined in Eq. (6.8). This ratio is measured using data from MC simulation. To obtain reliable values for this efficiency ratio, the kinematic properties of the simulated B^0 meson and its production environment need to be consistent with that observed in data. The comparison of several such properties, which can produce a sizable impact on $R_{i,\text{eff}}(L^B_{\text{prop}})$, reveal some differences between data and simulation. These differences are corrected for by an appropriate re-weighting of the simulated events using the procedure described in Section 9.1.1. The properties considered include the transverse momentum and pseudorapidity of the B^0 meson and the average number of pile-up events.

9.1.1 Monte Carlo re-weighting

The first property considered is the transverse momentum $p_T(B^0)$ of the B^0 meson and the distribution of $p_T(B^0)$ is found to be different in data and MC simulation. Figure 9.1 shows the $p_T(B^0)$ distributions for the 2011 and

2012 data sets for $B^0 \to J/\psi K_S$ and $B^0 \to J/\psi K^{*0}$ candidates. To build the distributions, a background subtraction procedure is applied to the data and the Monte-Carlo simulation. For each $p_T(B^0)$ bin, a signal band containing all candidates with $5230 < M(J/\psi K^{*0}) < 5330$ GeV and two background bands with $5150 < M(J/\psi K^{*0}) < 5200$ GeV and $5360 < M(J/\psi K^{*0}) < 5410$ GeV are defined. The signal and background bands are the same for both the $B^0 \to J/\psi K_S$ and $B^0 \to J/\psi K^{*0}$ channels. The number of signal candidates is obtained by subtracting the number of candidates in the two background bands from the number of candidates in the signal band. For simulation, all of the reconstructed particles in the corresponding B^0 decay are required to match the true generated decay products of the B^0 meson. The same background subtraction procedure is then applied to the selected simulated events.

The observed difference between data and MC is accounted for by applying a weight to the MC events according to the reconstructed value of $p_T(B^0)$. To obtain this weight, the ratio of the number of B^0 candidates in data and MC is parametrised by a continuous function. This function is different for the $B^0 \to J/\psi K_S$ and $B^0 \to J/\psi K^{*0}$ channels and it also differs for the 2011 and 2012 data samples. The applied weight is equal to the value of this function for a given value of $p_T(B^0)$. The ratio of the number of B^0 candidates in data and MC and its parametrisation are shown in Fig. 9.2.

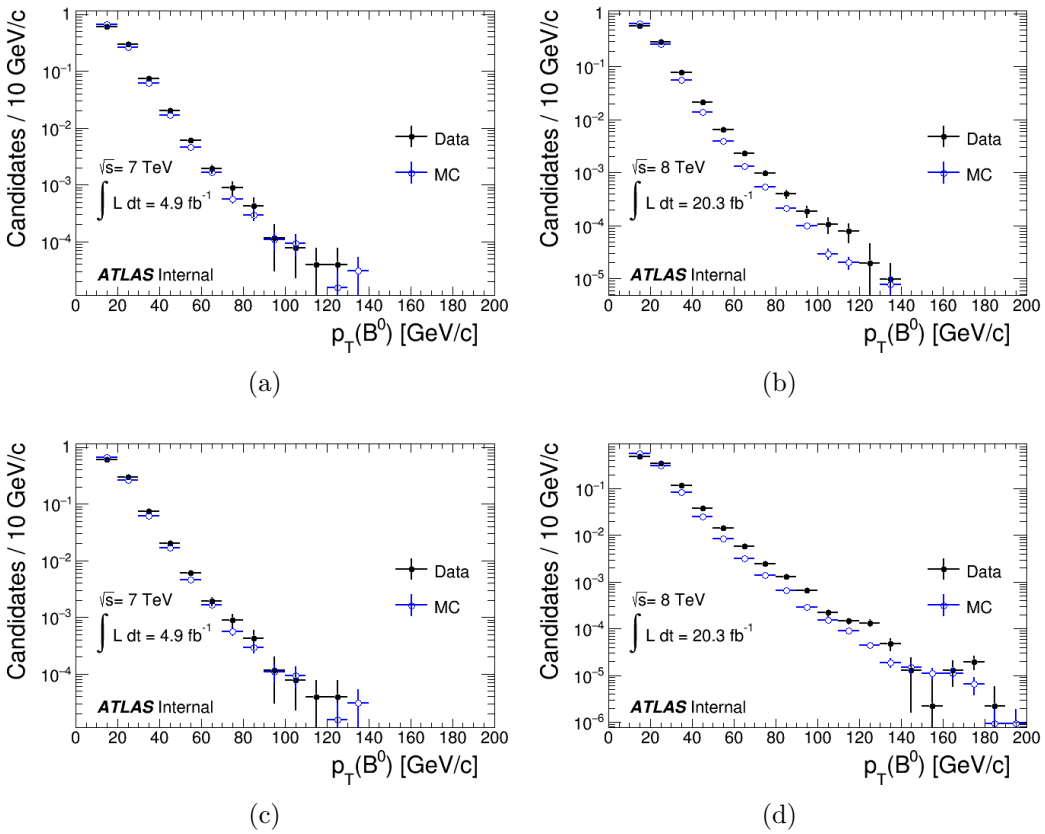

Figure 9.1: Number of B^0 candidates in data and in MC as a function of $p_T(B^0)$ for (a,b) $B^0 \to J/\psi K_S$ and (c,d) $B^0 \to J/\psi K^{*0}$ decays.

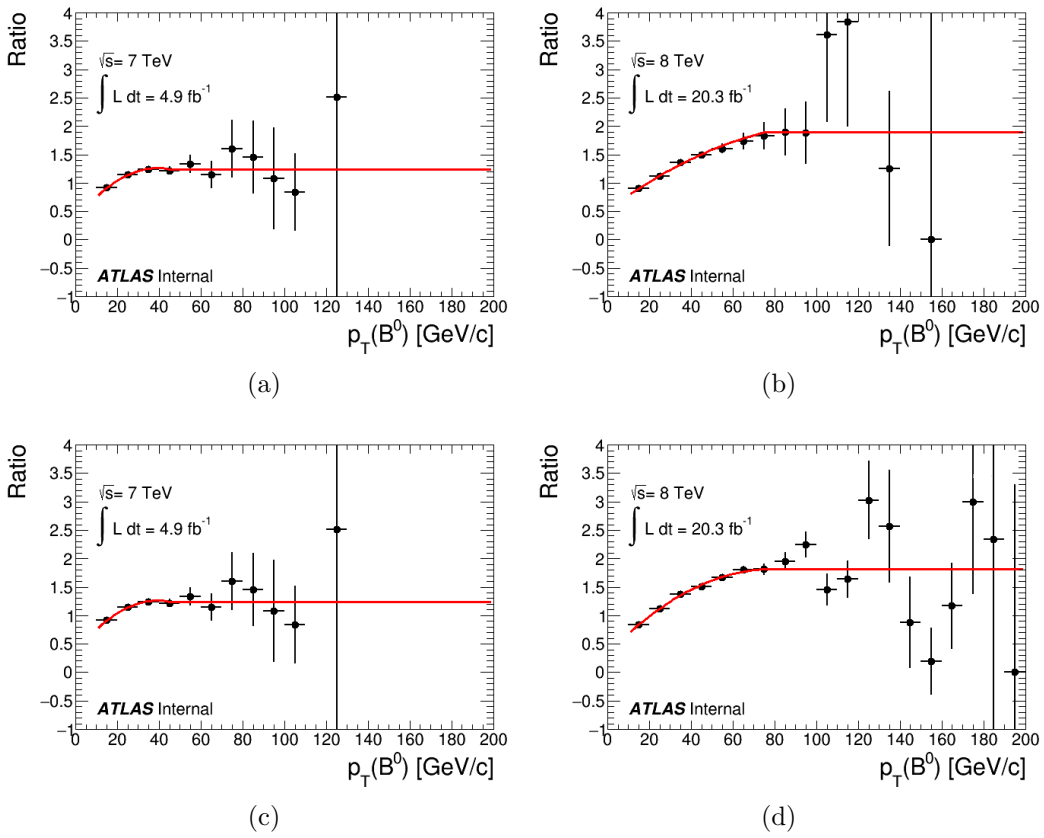

Figure 9.2: The ratio of the number of B^0 candidates in data and MC as a function of $p_T(B^0)$ for (a,b) $B^0 \to J/\psi K_S$ and (c,d) $B^0 \to J/\psi K^{*0}$ decays. The normalisation is arbitrary. The full line shows the parametrisation by a continuous function.

The second variable considered is the pseudorapidity $\eta(B^0)$ of the B^0 meson. Figure 9.3 shows the distributions of $\eta(B^0)$ for B^0 candidates in data and MC. These distributions are obtained using the same background subtraction procedure as the distributions of $p_T(B^0)$. The ratio of data to MC distributions is shown in Fig. 9.4. To account for the observed difference in $\eta(B^0)$, a weight is applied to the MC events. It is defined as the ratio of data to MC number of the B^0 candidates in a given $\eta(B^0)$ bin. Different $\eta(B^0)$ weights are applied to the $J/\psi K_S$ and $J/\psi K^{*0}$ channels and to the 2011 and 2012 data samples.

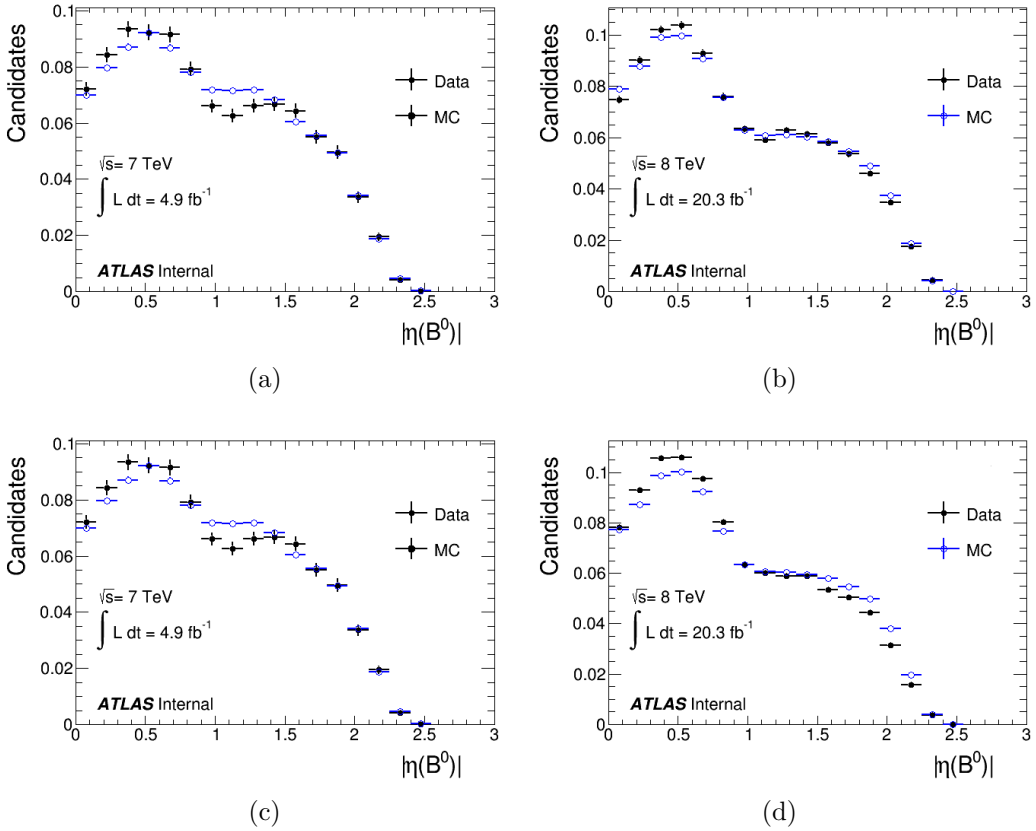

Figure 9.3: Number of B^0 candidates in data and in MC as a function of $\eta(B^0)$ for (a,b) $B^0 \to J/\psi K_S$ and (c,d) $B^0 \to J/\psi K^{*0}$ decays.

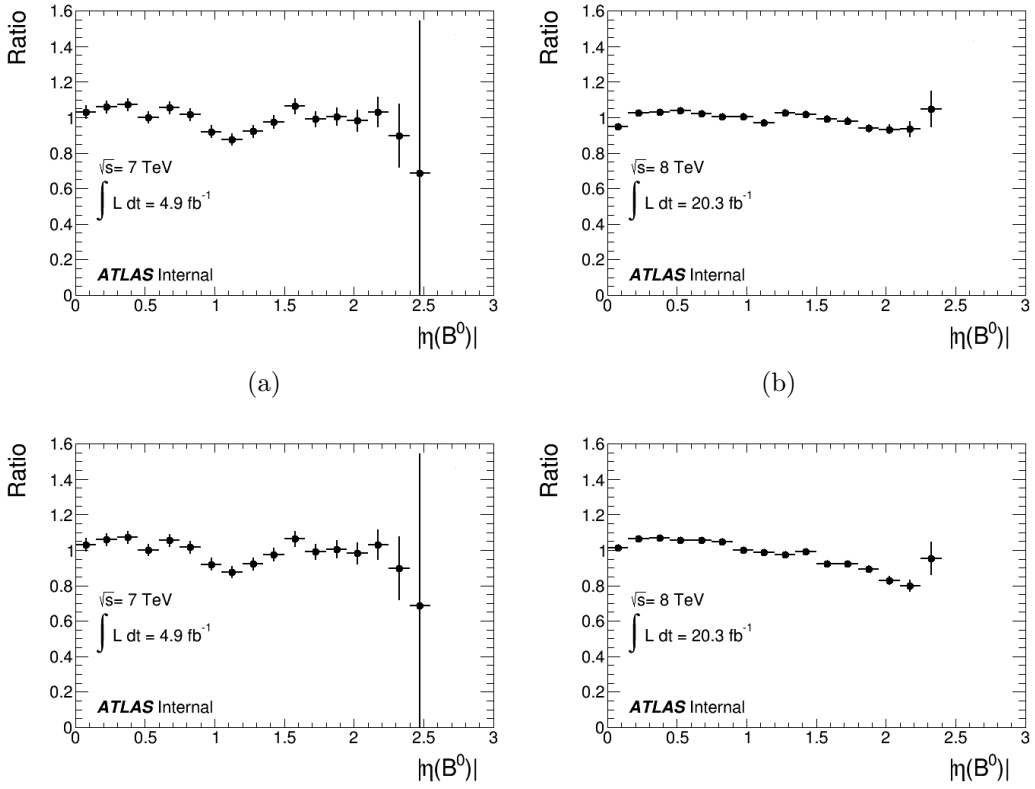

Figure 9.4: The ratio of the number of B^0 candidates in data and MC as a function of $\eta(B^0)$ for (a,b) $B^0 \to J/\psi K_S$ and (c,d) $B^0 \to J/\psi K^{*0}$ decays. The normalisation is arbitrary.

The third quantity considered is the number of background pile-up interactions registered simultaneously with the B^0 production. The charged tracks produced in the pile-up interactions make the detection of the B^0 decay more difficult and reduce its reconstruction efficiency. Therefore, it is important that the description of the pile-up interactions is consistent between data and simulation. Figure 9.5 shows the distributions of the average number of pile-up interactions $\mu(B^0)$ accompanying the detected B^0 candidates in data and MC. These distributions are obtained using the same background subtraction procedure as the distributions of $p_T(B^0)$. The observed difference between data and MC is due to the way in which pile-up events are simulated, which is described in Section 5.3.5. This difference is corrected by applying an additional weight to the MC events. The weight

is defined as the ratio of data to MC of the number of B^0 candidates in a given $\mu(B^0)$ bin. This ratio is shown in Fig. 9.6. Different $\mu(B^0)$ weights are applied to the $J/\psi K_S$ and $J/\psi K^{*0}$ channels and to the 2011 and 2012 data samples.

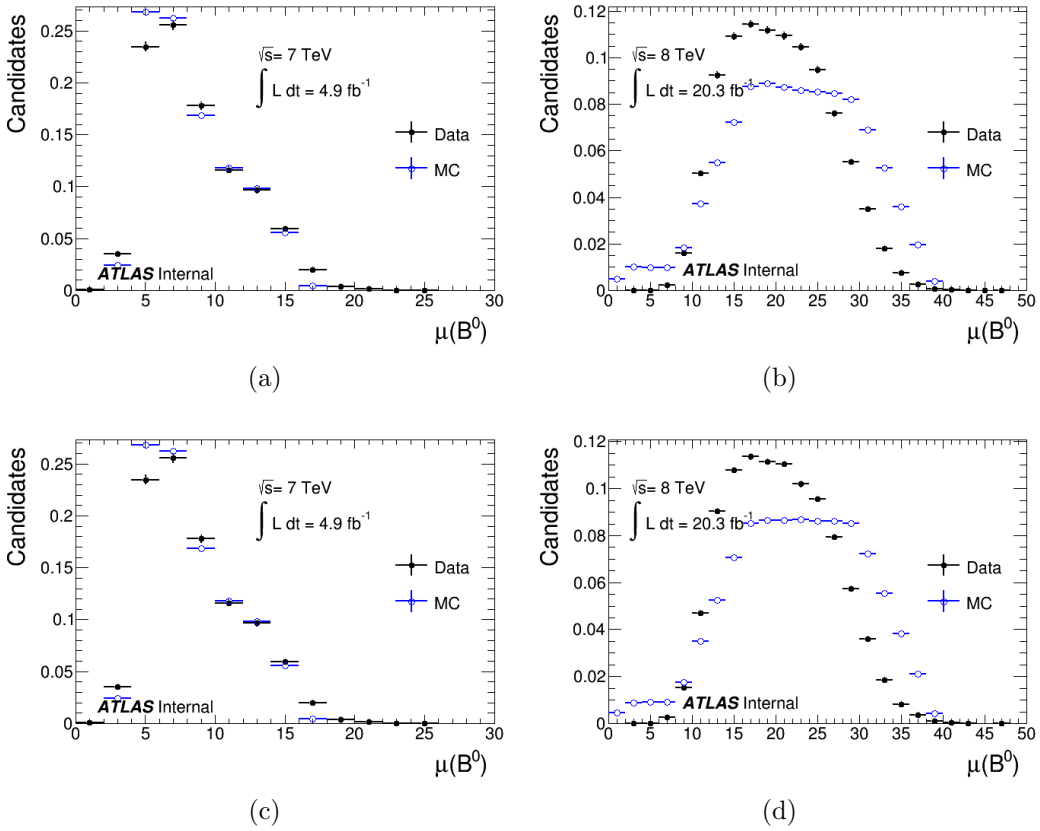

Figure 9.5: Number of B^0 candidates in data and in MC as a function of $\mu(B^0)$ for (a,b) $B^0 \to J/\psi K_S$ and (c,d) $B^0 \to J/\psi K^{*0}$ decays.

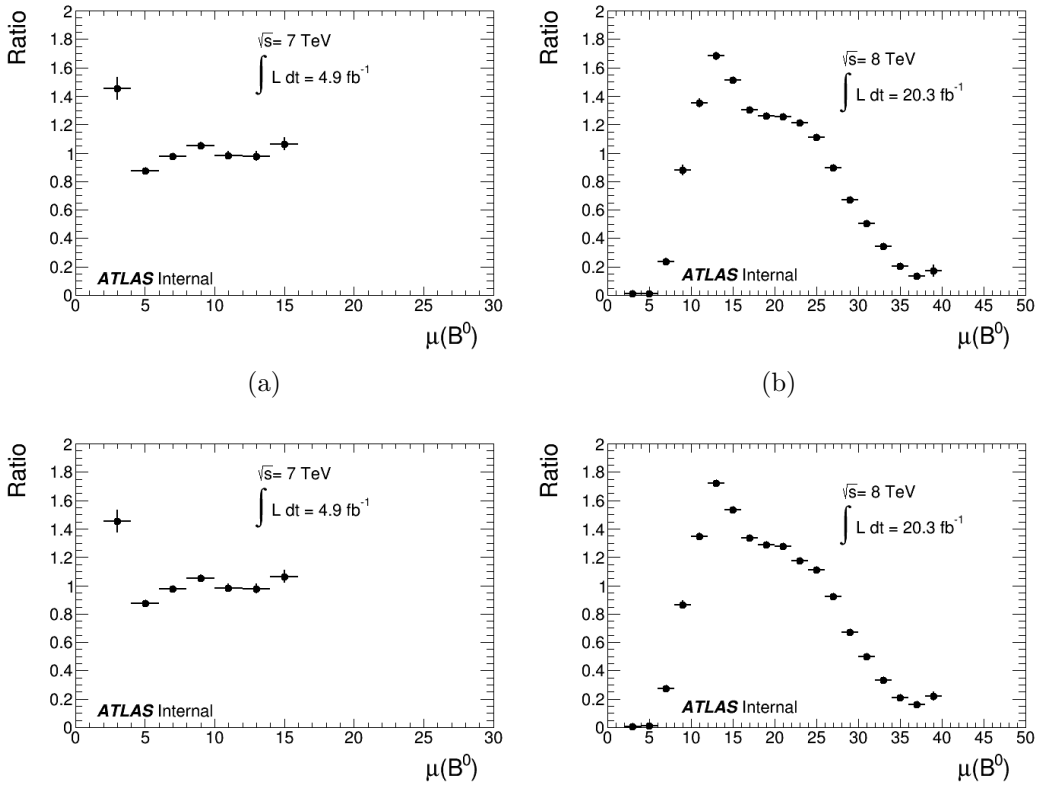

Figure 9.6: The ratio of the number of B^0 candidates in data and MC as a function of $\mu(B^0)$ for (a,b) $B^0 \to J/\psi K_S$ and (c,d) $B^0 \to J/\psi K^{*0}$ decays. The normalisation is arbitrary.

9.1.2 Resulting $R_{i,\mathrm{eff}}(L^B_{\mathrm{prop}})$ distribution

The resulting weight applied to the MC events is defined as the product of the three weights ($p_T(B^0)$, $\eta(B^0)$ and $\mu(B^0)$) described above. The distribution of $R_{i,\mathrm{eff}}(L^B_{\mathrm{prop}})$ obtained after re-weighting is shown in Fig. 9.7. The normalisation of this ratio is arbitrary; only its deviation from a constant can impact the measurement of $\Delta\Gamma_d$. This deviation is found to be very small and does not exceed 5% for proper decay lengths up to 2 mm. The achieved stability of the $R_{i,\mathrm{eff}}(L^B_{\mathrm{prop}})$ distribution is an important consequence of the chosen measurement procedure. Figure 9.8 shows the ratio of weighted to unweighted distributions of $R_{i,\mathrm{eff}}(L^B_{\mathrm{prop}})$ fitted to a first order polynomial. The fit has a slope of $(1.25 \pm 1.63) \times 10^{-2}$ for the 2011 dataset and $(-0.60 \pm 4.90) \times 10^{-3}$

for the 2012 dataset. This demonstrates that the re-weighting procedure does not substantially change the measurement of $\Delta\Gamma_d$ because the slopes are consistent with zero.

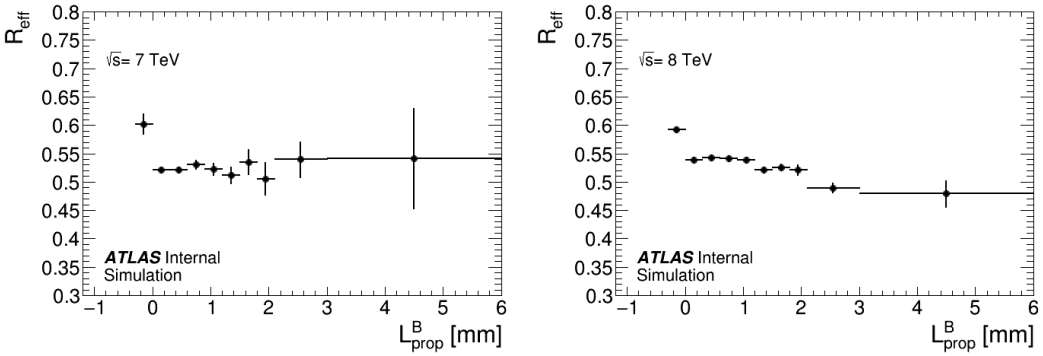

(a) (b)

Figure 9.7: The ratio of reconstruction efficiencies of $B^0 \to J/\psi K_S$ and $B^0 \to J/\psi K^{*0}$ decays (R_{eff}) determined as a function of the proper decay length of the B^0 meson (L^B_{prop}) for (a) $\sqrt{s} = 7$ TeV and (b) $\sqrt{s} = 8$ TeV simulated events. The normalisation is arbitrary.

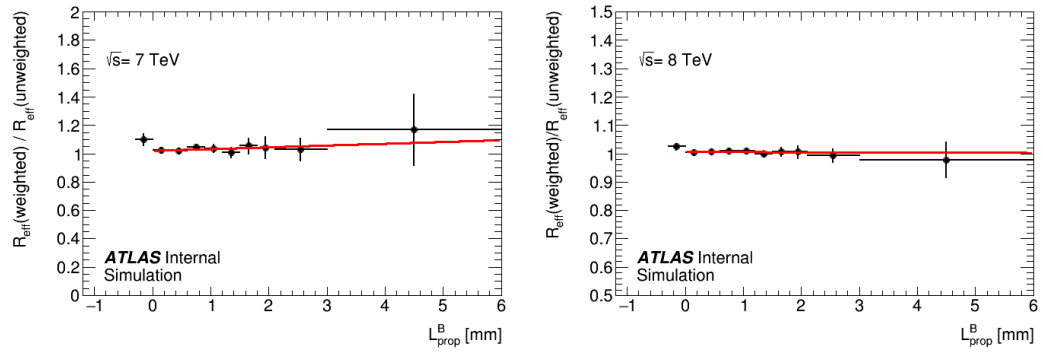

(a) (b)

Figure 9.8: Ratio of corrected to non-corrected values of R_{eff} as a function of L^B_{prop}. The full line shows the result of the fit by a straight line.

To check that the measurement method is consistent between the 2011 and 2012 datasets, the ratios of reconstruction efficiencies for the two years are compared. Figure 9.9 shows the ratio $R_{i,\text{eff}}(2012)/R_{i,\text{eff}}(2011)$. This ratio is fitted with a first order polynomial. The fit gives $\chi^2/n.d.f. = 5.29/7$ and

a slope of $(-2.42 \pm 1.19) \times 10^{-2}$. The slope is due to the difference in the experimental conditions between the 2011 and 2012, such as the transverse momentum and pseudorapidity of the B^0, and the average number of pile-up interactions per event.

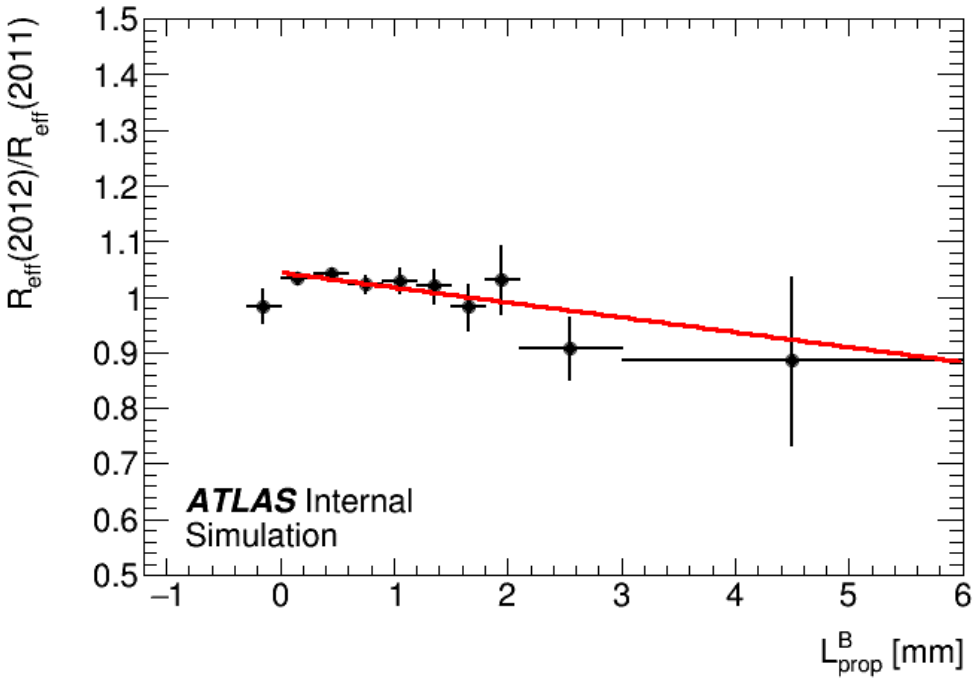

Figure 9.9: Ratio of the efficiency ratios $R_{\text{eff}}(2012)/R_{\text{eff}}(2011)$. The full line shows the result of the fit by a straight line.

9.2 Fit of $\Delta\Gamma_d/\Gamma_d$

The obtained values of $R_{i,\text{eff}}$ are used to correct the observed ratio $R_{i,\text{uncor}}$ given by Eq. (7.3). The resulting ratio $R_{i,\text{cor}}$ is defined as:

$$R_{i,\text{cor}} = \frac{R_{i,\text{uncor}}}{R_{i,\text{eff}}}. \tag{9.1}$$

This ratio is shown in Figure 9.10. It is used to obtain $\Delta\Gamma_d/\Gamma_d$ by the following procedure. For each L^B_{prop} bin i defined in Table 7.2, the expected

numbers of events in the $J/\psi K_S$ and $J/\psi K^{*0}$ channels are computed as:

$$N_i[\Delta\Gamma_d/\Gamma_d, J/\psi K_S] = C_1 \int_{L_i^{\min}}^{L_i^{\max}} \Gamma[L^B_{\rm prop}, J/\psi K_S] \mathrm{d}L^B_{\rm prop}, \quad (9.2)$$

$$N_i[\Delta\Gamma_d/\Gamma_d, J/\psi K^{*0}] = C_2 \int_{L_i^{\min}}^{L_i^{\max}} \Gamma[L^B_{\rm prop}, J/\psi K^{*0}] \mathrm{d}L^B_{\rm prop}. \quad (9.3)$$

The integration limits $L_i^{\min}$ and $L_i^{\max}$ for each bin i are given by the lower and upper bin edges in Table 7.2. C_1 and C_2 are arbitrary normalisation coefficients. The expressions for $\Gamma[L^B_{\rm prop}, J/\psi K_S]$ and $\Gamma[L^B_{\rm prop}, J/\psi K^{*0}]$ are given by Eqs. (6.6) and (6.7), respectively. As explained in Sec. 2.7, the sensitivity to $\Delta\Gamma_d$ comes from $\Gamma[L^B_{\rm prop}, J/\psi K_S]$ while $\Gamma[L^B_{\rm prop}, J/\psi K^{*0}]$ provides the normalisation, which helps to reduce the systematic uncertainties. The expected ratio of the decay rates in the two channels in each $L^B_{\rm prop}$ bin is:

$$R_{i,\rm exp}[\Delta\Gamma_d/\Gamma_d] = \frac{N_i[\Delta\Gamma_d/\Gamma_d, J/\psi K_S]}{N_i[\Delta\Gamma_d/\Gamma_d, J/\psi K^{*0}]}. \quad (9.4)$$

The relative width difference $\Delta\Gamma_d/\Gamma_d$ is obtained from a χ^2 minimisation:

$$\chi^2[\Delta\Gamma_d/\Gamma_d] = \sum_{i=2}^{10} \frac{(R_{i,\rm cor} - R_{i,\rm exp}[\Delta\Gamma_d/\Gamma_d])^2}{\sigma_i^2}. \quad (9.5)$$

The values σ_i are the statistical uncertainties of $R_{i,\rm cor}$. In the sum, the first bin of $L^B_{\rm prop}$ is not included as it corresponds to a negative decay length.

The free parameters in this minimisation are the overall normalisation and $\Delta\Gamma_d/\Gamma_d$. All other parameters describing the B^0 meson are fixed to their world average values [2]. The fit is performed separately for the 2011 and 2012 samples because the systematic uncertainties for the two data samples are different. The result of the fit is shown in Figure 9.10. The χ^2 of the fit is 4.34 ($n.d.f. = 7$) in the 2011 data set and 2.81 ($n.d.f. = 7$) in the 2012 data set.

The fit yields:

$$\Delta\Gamma_d/\Gamma_d = (-2.8 \pm 2.2\ (\text{stat.}) \pm 1.5\ (\text{MC stat.})) \times 10^{-2} \quad (2011), \quad (9.6)$$

$$\Delta\Gamma_d/\Gamma_d = (+0.8 \pm 1.3\ (\text{stat.}) \pm 0.5\ (\text{MC stat.})) \times 10^{-2} \quad (2012). \quad (9.7)$$

Here the uncertainties due to the data and MC statistics are given separately. The MC statistical uncertainty is treated as systematic. All other systematic uncertainties are discussed in Section 9.3.

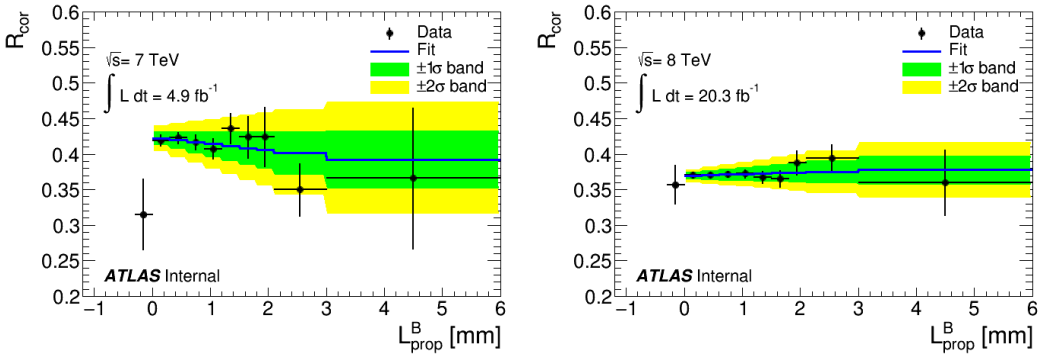

(a) (b)

Figure 9.10: Efficiency-corrected ratio of the observed decay length distributions, $R_{\rm cor}(L^B_{\rm prop})$ for (a) $\sqrt{s} = 7$ TeV and (b) $\sqrt{s} = 8$ TeV data sets. The normalisation of the two data sets is arbitrary. The full line shows the fit of $R_{\rm cor}(L^B_{\rm prop})$ to $R_{\rm exp}$ given by Eq. (9.4). The error bands correspond to uncertainties in $\Delta\Gamma_d/\Gamma_d$ determined by the fit.

To check that the uncertainties in the obtained values of $\Delta\Gamma_d/\Gamma_d$ are symmetric and therefore can be treated as such, the variation of $\chi^2[\Delta\Gamma_d/\Gamma_d]$ around its minimum is examined. Figure 9.11 shows the distribution of $\chi^2[\Delta\Gamma_d/\Gamma_d]$ near the minimum. The distribution is fitted with a second order polynomial, shown as a solid line. The constant defining the dashed line is equal to the minimum χ^2 value of the parabola plus one. The points where this line intersects the χ^2 parabola give estimates of the asymmetric statistical uncertainties, σ_- and σ_+, of the measurement of $\Delta\Gamma_d/\Gamma_d$. Since the χ^2 parabola is approximately symmetric, $\sigma_- \approx \sigma_+$, which demonstrates that the uncertainties are indeed symmetric.

9.3 Systematic uncertainties

The relative B^0 width difference is extracted from the ratio of the $L^B_{\rm prop}$ distributions in the two B^0 decay modes, which are obtained using a similar procedure, the same type of information and in the same production en-

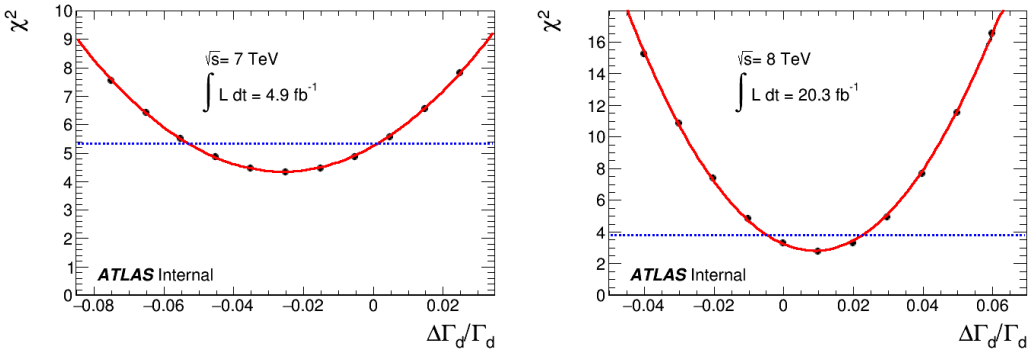

Figure 9.11: The χ^2 minimum distribution for the fit of $R_{cor}(L^B_{\text{prop}})$ for (a) the 2011 data sample and (b) the 2012 data sample. The solid red line shows the fit to the distribution by a second order polynomial. The dashed blue line shows minimum χ^2 value of the parabola plus one. The points where the two lines intersect indicate the values of the asymmetric statistical uncertainties of the measurement of $\Delta\Gamma_d/\Gamma_d$.

vironment. Therefore, the impact of many systematic uncertainties, such as the trigger selection, decay-time resolution or B^0 production properties, is negligible. However, some differences between the $B^0 \to J/\psi K_S$ and $B^0 \to J/\psi K^{*0}$ channels cannot be eliminated and the inaccuracy of their simulation results in systematic uncertainties, which are estimated in this section.

The mean proper decay length of the K_S meson is 26.8 mm. Since the transverse momentum of the K_S meson can be high, some K_s mesons decay outside the inner detector and are lost. The probability of losing a K_S meson is higher for large B^0 decay length due to the reduction of the fiducial volume of the K_S decay. Thus, the displaced vertex of the K_S decay and the absence of such a vertex in the $K^{*0} \to K^+\pi^-$ decay results in an L^B_{prop} dependence of the distribution of $R_{i,\text{eff}}$ defined in Eq. (6.8). Applying the correction given by Eq. (9.1) to $R_{i,\text{uncor}}$ takes into account this dependence.

The simulated K_S reconstruction is tested by comparing the distribution of the K_S decay length in data and simulation. This dedicated study shows that there is a residual difference between data and MC simulation in the distribution of the laboratory decay length of reconstructed K_S mesons

projected along the K_S momentum in the transverse plane, $L_{xy}(K_S)$. The distributions of $L_{xy}(K_S)$ in data and MC are shown in Fig. 9.12(a). Figure 9.12(b) shows the measured values of $\Delta\Gamma_d/\Gamma_d$ in four non-overlapping samples of $L_{xy}(K_S)$, fitted by a constant. The $\chi^2/n.d.f.$ of this fit is 5.63/3, which demonstrates that the difference in $L_{xy}(K_S)$ between data and simulation does not introduce any bias in the measurement of $\Delta\Gamma_d/\Gamma_d$. To correct for this difference, an additional weight is applied to the MC events to make the distribution of $L_{xy}(K_S)$ in Monte Carlo the same as in data. This results in a change in the value of $\Delta\Gamma_d/\Gamma_d$ of $\delta(\Delta\Gamma_d/\Gamma_d) = -0.21 \times 10^{-2}$ for the 2011 data sample and $\delta(\Delta\Gamma_d/\Gamma_d) = -0.16 \times 10^{-2}$ for the 2012 data sample. This difference is taken as the systematic uncertainty due to modelling of the $L_{xy}(K_S)$ dependence of the K_S reconstruction.

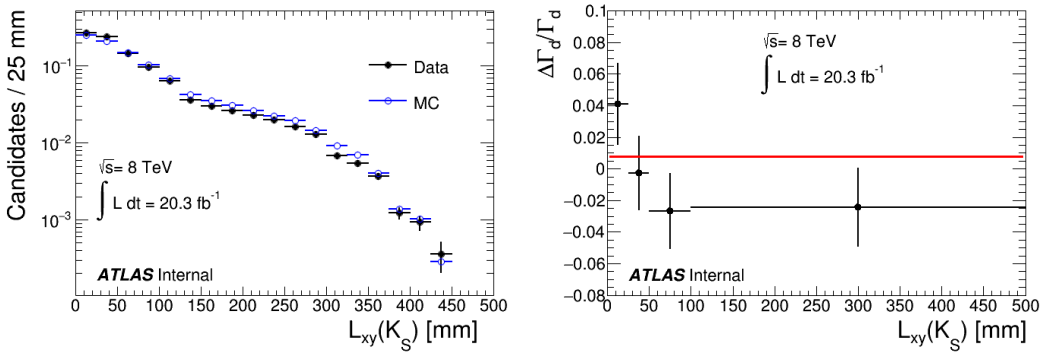

(a) (b)

Figure 9.12: (a) Comparison of the $L_{xy}(K_{S)}$ distribution in data and MC and (b) Measurement of $\Delta\Gamma_d/\Gamma_d$ in four non-overlapping samples of $B^0 \to J/\psi K_S$ candidates defined according to $L_{xy}(K_S)$ at $\sqrt{s} = 8$ TeV.

A further test of the K_S reconstruction in MC is conducted by applying the procedure used for $L_{xy}(K_S)$ to the pseudorapidity distribution of the K_S meson, $\eta(K_S)$. Figure 9.13(a) shows the distributions of $\eta(K_S)$ in data and MC. Measurements of $\Delta\Gamma_d/\Gamma_d$ in four non-overlapping samples of $\eta(K_S)$, fitted by a constant, are shown in Fig. 9.13(b). The fit has $\chi^2/n.d.f. = 4.86/3$ which indicates that the residual discrepancy in $\eta(K_S)$ between data and MC does not cause any bias in the measured value of $\Delta\Gamma_d/\Gamma_d$. The systematic uncertainty due to modelling of the $|\eta(K_S)|$ dependence of the K_S reconstruction is estimated by re-weighting the MC

events to make the $|\eta(K_S)|$ distribution the same as in data. The observed changes are $\delta(\Delta\Gamma_d/\Gamma_d) = +0.14 \times 10^{-2}$ for the 2011 data set and $\delta(\Delta\Gamma_d/\Gamma_d) = -0.01 \times 10^{-2}$ for the 2012 data set.

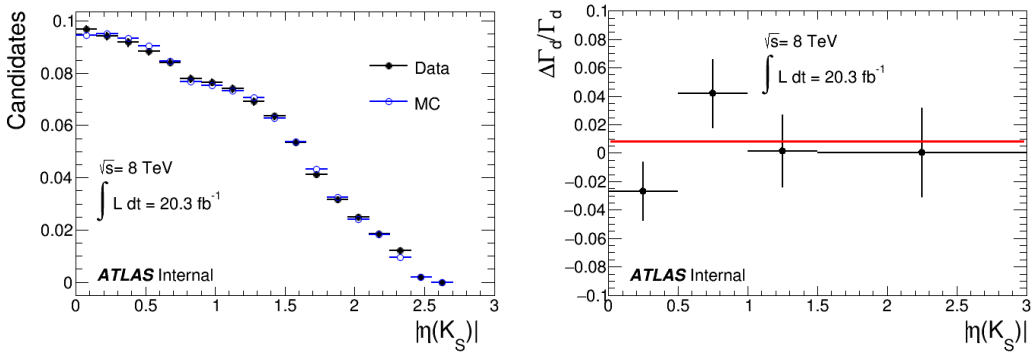

(a) (b)

Figure 9.13: (a) Comparison of the $|\eta(K_S)|$ distribution in data and MC and (b) Measurement of $\Delta\Gamma_d/\Gamma_d$ in four non-overlapping samples $B^0 \to J/\psi K_S$ candidates defined according to $|\eta(K_S)|$ at $\sqrt{s} = 8$ TeV.

The systematic uncertainty due to the choices made in the model used to fit the mass distributions can be estimated by considering different variations of the fit model. The range over which the $B^0 \to J/\psi K_S$ and $B^0 \to J/\psi K^{*0}$ mass fits are applied is varied and the measurement of $\Delta\Gamma_d/\Gamma_d$ is repeated for each variation. The systematic uncertainty is estimated by taking the difference between the values of $\Delta\Gamma_d/\Gamma_d$ obtained from the default fit and each of the varied fits. Variations $\delta(\Delta\Gamma_d/\Gamma_d) = -0.47\times10^{-2}$ and -0.30×10^{-2} are obtained for the 2011 data set in the $J/\psi K_S$ and $J/\psi K^{*0}$ channels, respectively. The changes for the 2012 data set are $\delta(\Delta\Gamma_d/\Gamma_d) = -0.59\times10^{-2}$ and -0.15×10^{-2} in the $J/\psi K_S$ and $J/\psi K^{*0}$ channels, respectively. These values are included as the systematic uncertainty from this source.

Additionally, the background function is changed from an exponential to a fourth-order polynomial and the systematic uncertainty due to the choice of background function is estimated from the difference between the value of $\Delta\Gamma_d/\Gamma_d$ from the default fit and the value from the fit using the polynomial background function. A change $\delta(\Delta\Gamma_d/\Gamma_d) = -0.16\times10^{-2}$ is obtained for the 2011 data set. The change for the 2012 data set is $\delta(\Delta\Gamma_d/\Gamma_d) = +0.09\times10^{-2}$.

In the fit of the number of $B^0 \to J/\psi K_S$ decays the contribution from

the $B_s^0 \to J/\psi K_S$ is a free parameter of the fit. As a systematic uncertainty cross-check, the ratio of the yields of these two decays is fixed to be the same as that measured by the LHCb Collaboration [60]. The resulting change in the $\Delta\Gamma_d/\Gamma_d$ value is $\delta(\Delta\Gamma_d/\Gamma_d) = -0.11 \times 10^{-2}$ for the 2011 data set and $\delta(\Delta\Gamma_d/\Gamma_d) = +0.08 \times 10^{-2}$ for the 2012 data set and is included as an additional source of systematic uncertainty.

The systematic uncertainty due to the resolution of $L^B_{\rm prop}$ is also considered. The function that describes the resolution for the $B^0 \to J/\psi K_S$ and $B^0 \to J/\psi K^{*0}$ decay modes is given in Eq. (7.2). The values of f, σ_1 and σ_2 for the two channels in 2011 and 2012 are given in Table 7.1. To test the sensitivity to the resolution, the measurement of $\Delta\Gamma_d/\Gamma_d$ is repeated by using the resolution of $J/\psi K^{*0}$ for both channels. A change in the value of $\Delta\Gamma_d/\Gamma_d$ of $\delta(\Delta\Gamma_d/\Gamma_d) = -0.29 \times 10^{-2}$ is obtained and is used as the systematic uncertainty from this source. It is found to be the same for the 2011 and 2012 data samples.

A toy MC sample is employed to identify any possible bias in the fitting procedure. In this toy MC sample, the expected number of $J/\psi K_S$ candidates is determined according to the analytic function given by Eq. (2.48). The expected number of $J/\psi K^{*0}$ candidates is determined from the sum of Eqs. 2.50 and 2.53. A value of $\Delta\Gamma_d/\Gamma_d = 0.42 \times 10^{-2}$ corresponding to the SM expectation given in Eq. (6.4) is used. Using the expected numbers of candidates as the mean values, the number of candidates in both channels is randomly generated in each $L^B_{\rm prop}$ bin with an uncertainty corresponding to that obtained in data. The ratio of the obtained distributions is then fitted using the method described in Section 9.2. This procedure is repeated 10 000 times and the pull value from each fit is obtained. The pull value is defined as $(V - V_{SM})/\sigma$ where V is the value of $\Delta\Gamma_d/\Gamma_d$ obtained from the fit, σ is its uncertainty and V_{SM} is the SM expectation value. The distribution of the pull values is shown in Fig. 9.14. The fit to this distribution using a Gaussian gives a mean of -0.049 ± 0.010 and a standard deviation of 1.007 ± 0.008. The residual bias is due to the non-symmetric uncertainties of the ratio of the two decay rates used in the analysis. The resulting bias in the mean fitted value of $\Delta\Gamma_d/\Gamma_d$ is $\delta(\Delta\Gamma_d/\Gamma_d) = +0.07 \times 10^{-2}$. This value is used as the systematic uncertainty due to the fitting procedure and it is taken to be

the same for the 2011 and 2012 data sets.

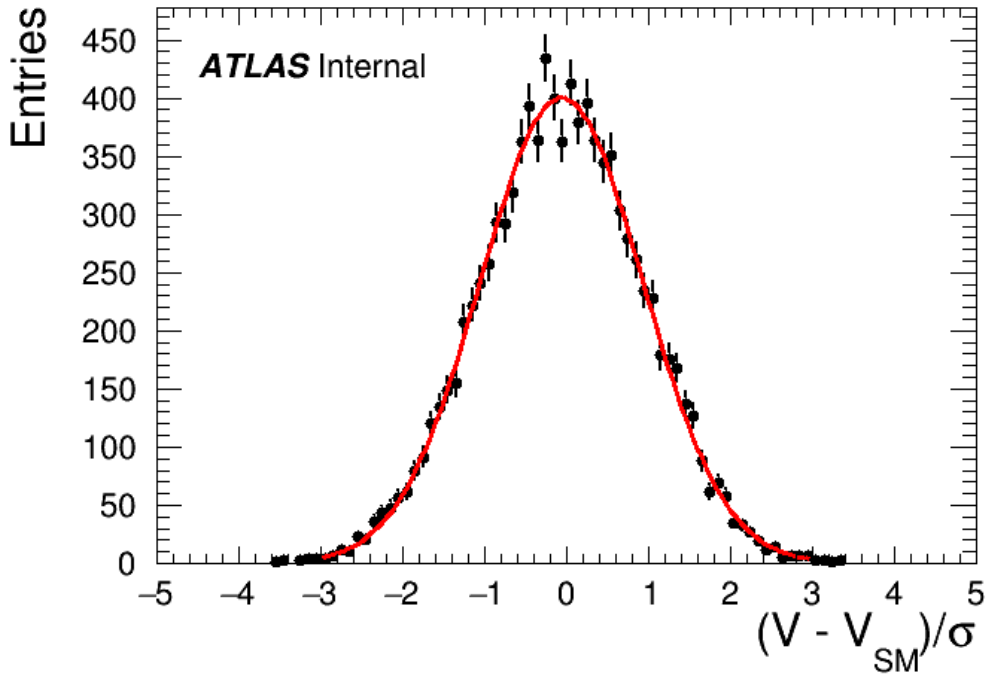

Figure 9.14: Distribution of pull values from the toy MC. The line shows the fit to the distribution by a Gaussian.

The uncertainty of the production asymmetry of B^0 mesons is propagated through the analysis. The impact of this uncertainty is $\delta(\Delta\Gamma_d/\Gamma_d) = 0.01 \times 10^{-2}$ for both the 2011 and 2012 data samples.

The systematic uncertainty from the number of events in the MC samples corresponds to an uncertainty of $\delta(\Delta\Gamma_d/\Gamma_d) = 1.54 \times 10^{-2}$ for the 2011 data set and $\delta(\Delta\Gamma_d/\Gamma_d) = 0.45 \times 10^{-2}$ for the 2012 data set.

Table 9.1 gives a summary of the estimated systematic uncertainties. All of the quantified systematic uncertainties are symmetrized.

9.3.1 Consistency cross-checks

In addition to the estimate of the systematic uncertainty, several cross-checks are performed. Some of the selection cuts described in Section 6 are modified and the corresponding changes in the $\Delta\Gamma_d/\Gamma_d$ value are assessed. In particular, the transverse momenta of the charged pions from the K_S decay and the charged pion from the K^{*0} decay are required to be greater than 500 MeV,

Source	$\delta(\Delta\Gamma_d/\Gamma_d)$, 2011	$\delta(\Delta\Gamma_d/\Gamma_d)$, 2012
K_S decay length	0.21×10^{-2}	0.16×10^{-2}
K_S pseudorapidity	0.14×10^{-2}	0.01×10^{-2}
$B^0 \to J/\psi K_S$ mass range	0.47×10^{-2}	0.59×10^{-2}
$B^0 \to J/\psi K^{*0}$ mass range	0.30×10^{-2}	0.15×10^{-2}
Background description	0.16×10^{-2}	0.09×10^{-2}
$B_s^0 \to J/\psi K_S$ contribution	0.11×10^{-2}	0.08×10^{-2}
L_{prop}^B resolution	0.29×10^{-2}	0.29×10^{-2}
Fit bias (Toy MC)	0.07×10^{-2}	0.07×10^{-2}
B^0 production asymmetry	0.01×10^{-2}	0.01×10^{-2}
MC sample	1.54×10^{-2}	0.45×10^{-2}
Total uncertainty	1.69×10^{-2}	0.84×10^{-2}

Table 9.1: Sources of systematic uncertainty in the $\Delta\Gamma_d/\Gamma_d$ measurement and their values for the 2011 and 2012 data sets.

rather than 400 MeV. Also, the transverse momentum of the charged kaon from the K^{*0} is required to be greater than 1 GeV, rather than 800 MeV. Additionally, the transverse momentum of the B^0 meson is required to be less than 60 GeV. In all cases, the change of the measured value of $\Delta\Gamma_d$ is consistent with fluctuations due to the reduced number of events.

Furthermore, a number of consistency checks related to the description of the experimental conditions in simulation are performed. Figure 9.15 shows the distribution of the primary vertex z position in data and Monte Carlo. The Monte Carlo events are re-weighted by the ratio of the distributions and the corresponding change in the value of $\Delta\Gamma_d/\Gamma_d$ is $\delta(\Delta\Gamma_d/\Gamma_d) = 0.62 \times 10^{-2}$ for the 2011 data sample and $\delta(\Delta\Gamma_d/\Gamma_d) = 0.02 \times 10^{-2}$ for the 2012 data sample. This change is much smaller than the statistical uncertainty and therefore does not impact the measured value of $\Delta\Gamma_d/\Gamma_d$.

Most of the Monte Carlo samples used in this analysis were produced with flat angular distributions for the $B^0 \to J/\psi K_S$ and $B^0 \to J/\psi K^{*0}$ decays. To assess the effect of this, two 7 TeV $B^0 \to J/\psi K^{*0}$ MC samples are compared, of which one was generated with a flat angular distribution and the other with angular distribution taken from the CDF angular analysis of the $B^0 \to J/\psi K^{*0}$ decay [61]. The angular analysis performed by CDF has now been superseded by a more precise analysis performed by LHCb [62], but this study was not available at the time that the MC samples were

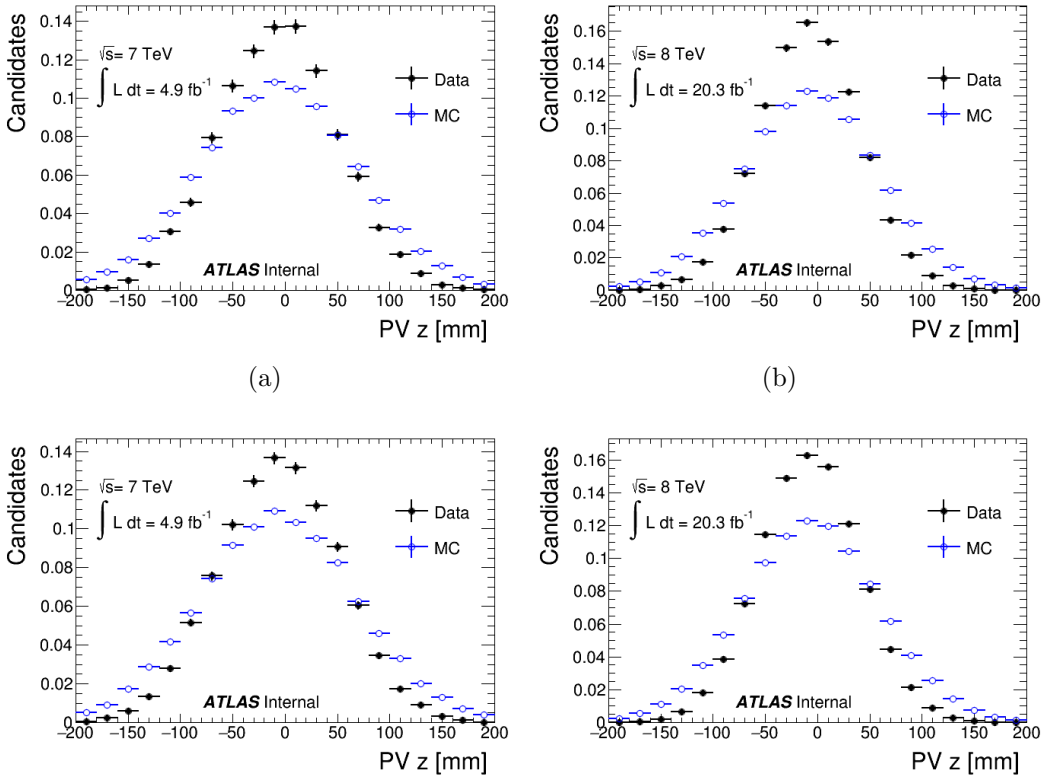

Figure 9.15: Number of B^0 candidates in data and in MC as a function of the z position of the primary vertex for (a,b) $B^0 \to J/\psi K_S$ and (c,d) $B^0 \to J/\psi K^{*0}$ decays.

generated. The distributions of $R_{i,\text{eff}}$ obtained from these two samples and their ratio are shown in Fig. 9.16. The fit to the ratio by a first order polynomial has $\chi^2/n.d.f. = 2.50/7$ and a slope of $(-1.10 \pm 1.90) \times 10^{-2}$. The difference between the angular distributions in the MC samples is therefore negligible and does not affect the measurement of $\Delta\Gamma_d/\Gamma_d$.

The final cross-check involved re-weighting the Monte Carlo events selected with the trigger that shows the largest discrepancy between data and MC, EF_2mu4T_Jpsimumu_L2StarB, to make the selection rate correspond to that in data. No impact on the measured value of $\Delta\Gamma_d/\Gamma_d$ was found.

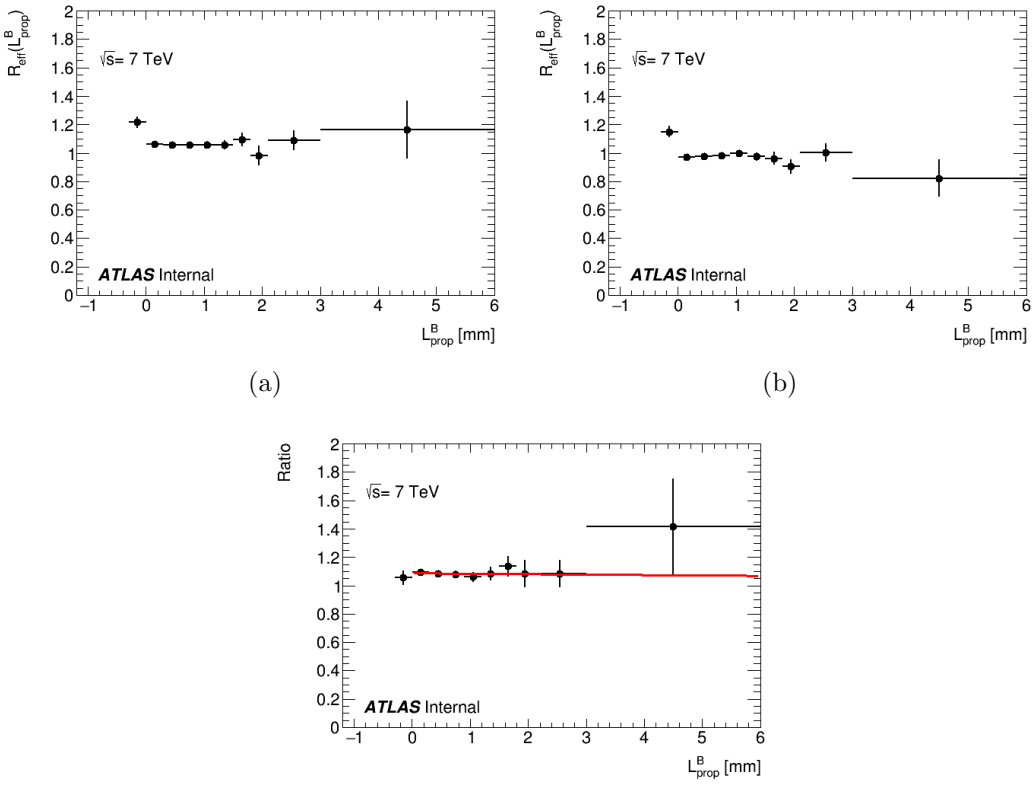

Figure 9.16: Distributions of $R_{i,\text{eff}}$ obtained from MC with (a) a flat angular distribution and (b) an angular distribution corresponding to the CDF measurement of the $B^0 \to J/\psi K^{*0}$ decay. [61]. The ratio of the two distributions is shown in (c).

9.4 Results

Using the measurements of $\Delta\Gamma_d/\Gamma_d$ given in Eqs. (9.6) and (9.7) and the study of systematic uncertainties presented in Section 9.3, the following measurements are obtained:

$$\begin{aligned} \Delta\Gamma_d/\Gamma_d &= (-2.8 \pm 2.2\ (\text{stat.}) \pm 1.7\ (\text{syst.})) \times 10^{-2} \quad (2011), \\ \Delta\Gamma_d/\Gamma_d &= (+0.8 \pm 1.3\ (\text{stat.}) \pm 0.8\ (\text{syst.})) \times 10^{-2} \quad (2012). \end{aligned}$$

These measurements are consistent and are combined, taking into account the correlations of different sources of systematic uncertainty between the two

years. The combination is done by averaging the correlated measurements using the following method. The covariance matrix V_{ij} is constructed as:

$$V_{ij} = \sum_{k=0}^{10} \sigma_i^k \sigma_j^k \rho_{ij}^k; \qquad i,j = 1,2 \tag{9.8}$$

The indices $i,j = 1$ correspond to the 2011 measurement and $i,j = 2$ correspond the 2012 measurement. The value σ_i^0 is the statistical uncertainty of measurement i and σ_i^k for $k > 0$ corresponds to the systematic uncertainty from source k, given in Table 9.1. The quantity ρ_{ij}^k is the correlation coefficient of the source k between the 2011 and 2012 data samples. The statistical uncertainties are not correlated ($\rho_{12}^0 = 0$). The systematic uncertainties due to the background description, the $B_s^0 \to J/\psi K_S$ contribution, and the limited MC statistics are assumed to be uncorrelated ($\rho_{12}^5 = \rho_{12}^6 = \rho_{12}^{10} = 0$). All other sources of systematic uncertainty are taken to be fully correlated ($\rho_{12}^k = 1$ for $k \neq 5,6,10$). Additionally, $\rho_{11}^k = \rho_{22}^k = 1$ for all k. The combined value of $\Delta\Gamma_d/\Gamma_d$ is obtained from the minimization of the following expression:

$$\chi^2[\bar{x}] = \sum_{i,j=1}^{2} (x_i - \bar{x})(x_j - \bar{x}) V_{ij}^{-1}. \tag{9.9}$$

Here x_i represent the individual measurements given by Eqs. (9.8) and (9.8) and $\bar{x}$ is the mean value of $\Delta\Gamma_d/\Gamma_d$.

The combined measurement of $\Delta\Gamma_d/\Gamma_d$ using the data collected by the ATLAS experiment in Run 1 of the LHC is:

$$\Delta\Gamma_d/\Gamma_d = (-0.1 \pm 1.1\ (\text{stat.}) \pm 0.9\ (\text{syst.})) \times 10^{-2}.$$

This is currently the most precise single measurement of this quantity. It agrees well with the SM prediction [49] and is consistent with other measurements of this quantity [7, 8, 55]. It also agrees with the indirect measurement by the D0 Collaboration [63].

Chapter 10

Flavour tagging

10.1 Introduction

This chapter describes the development of the flavour tagging methods used for the study of CP violation in the $B_s^0 \to J/\psi\phi$ decay. The description is based on the analyses of the $B_s^0 \to J/\psi\phi$ decay made by the ATLAS collaboration using data collected during Run 1 of the LHC [64, 65], to which the author of this thesis made a significant contribution.

The physics of a neutral B meson decaying to CP eigenstate are explained in Section 2.5. Since the final state f is the same for both $B_{(s)}^0$ and $\bar{B}_{(s)}^0$, CP violation can occur due to interference between direct decays and decays with $B_{(s)}^0 - \bar{B}_{(s)}^0$ mixing. The CP asymmetry is represented by the weak phase difference $\phi_{(s)} = \phi_M - 2\phi_f$ between the $B_{(s)}^0 - \bar{B}_{(s)}^0$ mixing amplitude and the $b \to c\bar{c}s$ decay amplitude as given in Eq. (2.44).

One channel for which there has been keen interest, due to possible new physics contributions in CP violation, is $B_s^0 \to J/\psi\phi$. The Standard Model prediction of the weak phase difference in the B_s^0 system is [66]:

$$\phi_s \approx -2\beta_s = 2\arg\left(-\frac{V_{ts}V_{tb}^*}{V_{cs}V_{cb}^*}\right) = -0.0363^{+0.0016}_{-0.0015}\ \text{rad}. \tag{10.1}$$

Precise measurements of ϕ_s performed by LHC experiments [64, 65, 67, 68] have constrained the potential new physics contribution, but more precision is still needed.

Since the measured CP violating effect is due to $B_s^0 - \bar{B}_s^0$ mixing, it is important to measure the initial flavour of the B_s^0 or $\bar{B}_s^0$ meson. Flavour tagging is the name of the method by which the flavour of B^0 and B_s^0 mesons is determined at the time of their production. In ATLAS, opposite side flavour tagging is used. This approach takes advantage of the fact that bottom quarks are produced in $b\bar{b}$ pairs, which allows the initial flavour of the B^0 or B_s^0 being studied to be determined from the flavour of the other B hadron in the event.

10.2 Data sample

The opposite side tagging methods are analysed using $B^\pm \to J/\psi K^\pm$ events. The charge of the kaon indicates the charge of the produced B meson. This decay channel is therefore ideal for studying flavour tagging because the known flavour of the $B^\pm$ meson provides a tag of the flavour of opposite side B hadron, which allows the flavour tagging algorithms to be calibrated.

10.2.1 2011 data sample

The first flavour tagging study in ATLAS [64] was made with 4.9 fb^{-1} of integrated luminosity taken in 2011 at $\sqrt{s} = 7$ TeV. The $B^\pm \to J/\psi K^\pm$ events used for the flavour tagging calibration are required to pass the EF_2mu4(T)_Jpsimumu trigger, demanding two oppositely charged muons forming a J/ψ candidate. Each muon must have a transverse momentum greater than 4 GeV and a pseudorapidity less than 2.5. The invariant mass of the dimuon candidate must be between 2.8 and 3.4 GeV. A $B^\pm$ candidate is formed by combining the dimuon candidate with an additional charged track from the event, which is required to have $p_T > 1$ GeV and $|\eta| < 2.5$. The combination is made using a vertex fit in which the dimuon mass is constrained to be between 3.1 and 3.2 GeV. The χ^2 of the vertex fit must be less than 10 for the one degree of freedom. The resulting $B^\pm$ candidate must have $\eta < 2.5$ and $5.0 < m(B^\pm) < 5.6$ GeV. Additionally, the laboratory transverse decay length (L_{xy}) of the $B^\pm$ candidate is required to be greater than 0.1 mm. This lifetime cut is designed to reduce the prompt component of the combinatorial background and does not introduce any bias because this

study is concerned only with determining the initial flavour of the opposite B meson. The invariant mass distribution of the selected $B^{\pm} \to J/\psi K^{\pm}$ candidates is shown in Fig. 10.1.

The function used to fit the invariant mass distribution is defined in the following way. The $B^{\pm} \to J/\psi K^{\pm}$ signal peak is represented by a Gaussian function. The combinatorial background is modelled by an exponential. The contribution in the low mass region due to partially reconstructed B decays is represented by a hyperbolic tangent function. The $B^{\pm} \to J/\psi \pi^{\pm}$ contribution is given by a Gaussian function. From this fit, a total of $194\,000 \pm 1\,000$ signal $B^{\pm}$ candidates are reconstructed, of which $98\,000 \pm 1\,000$ are B^{+} and $96\,000 \pm 1\,000$ are B^{-}. The uncertainties are the statistical only, from the fit. The number of significant figures given in these values is consistent with the ATLAS internal analysis note.

10.2.2 2012 data sample

The flavour tagging study made with the 2012 data sample used 19.5 fb^{-1} of integrated luminosity taken at $\sqrt{s} = 8$ TeV. The $B^{\pm} \to J/\psi K^{\pm}$ events are required to pass any trigger from the suite of single and dimuon triggers defined in Table 10.1. The fraction of events in the final sample selected by each trigger is also given. All other selection criteria were the same as those for the 2011 data sample.

Figure 10.1 shows the invariant mass distribution of the selected $B^{\pm} \to J/\psi K^{\pm}$ candidates. The function used to fit the invariant mass distribution is the same as that used for the 2011 data sample. From the fit, a total of $1\,116\,000 \pm 3\,000$ signal $B^{\pm}$ candidates are reconstructed, of which $563\,000 \pm 2\,000$ are B^{+} and $553\,000 \pm 2\,000$ are B^{-}. The uncertainties are the statistical only, from the fit. The number of significant figures given in these values is consistent with the ATLAS internal analysis note.

Trigger	Fraction (%)
EF_2mu4T_Bmumux	71.08
EF_2mu4T_Jpsimumu	69.57
EF_mu4Tmu6_Bmumux	65.64
EF_mu4Tmu6_Jpsimumu	63.35
EF_2mu4T_Jpsimumu_L2StarB	57.62
EF_2mu4T_Bmumux_v2	51.34
EF_2mu4T_Bmumux_Barrel	50.05
EF_mu4Tmu6_Jpsimumu_L2StarB	49.60
EF_2mu4T_Jpsimumu_Barrel	48.91
EF_2mu4T_Bmumux_v2_L2StarB	47.12
EF_2mu4T_Bmumux_BarrelOnly	46.21
EF_mu4Tmu6_Bmumux_v2	45.91
EF_2mu4T_Jpsimumu_BarrelOnly	45.01
EF_mu4Tmu6_Bmumux_v2_L2StarB	41.33
EF_2mu4T_Jpsimumu_Barrel_L2StarB	38.92
EF_mu4Tmu6_Bmumux_Barrel	37.73
EF_2mu4T_Jpsimumu_BarrelOnly_L2StarB	36.70
EF_mu4Tmu6_Jpsimumu_Barrel	36.35
EF_2mu4T_Bmumux_Barrel_v2_L2StarB	33.69
EF_2mu4T_Bmumux_BarrelOnly_v2_L2StarB	31.68
EF_mu4Tmu6_Jpsimumu_Barrel_L2StarB	28.14
EF_2mu6_Bmumux	26.77
EF_2mu6_Jpsimumu	24.86
EF_mu4Tmu6_Bmumux_Barrel_v2_L2StarB	23.67
EF_2mu6_Jpsimumu_L2StarB	18.58
EF_2mu6_Bmumux_v2	18.29
EF_2mu6_Bmumux_v2_L2StarB	16.19

Table 10.1: Triggers and respective fractions for $B^{\pm} \to J/\psi K^{\pm}$ events in 2012.

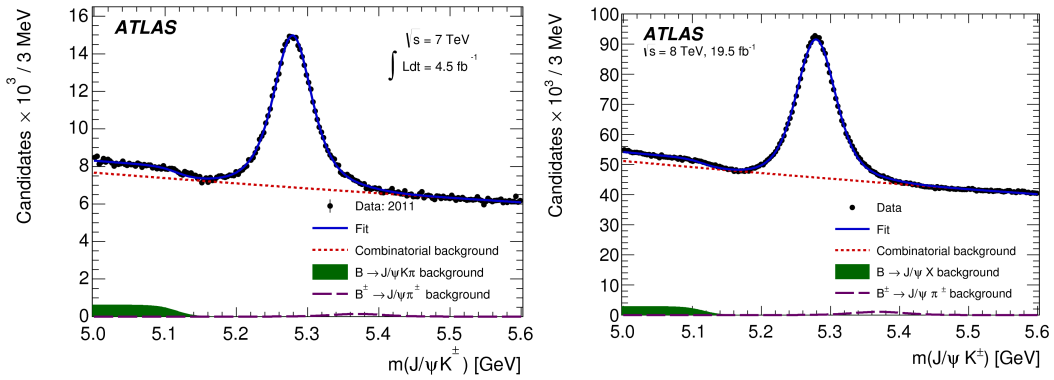

(a) (b)

Figure 10.1: The invariant mass distribution of $B^{\pm} \to J/\psi K^{\pm}$ candidates for (a) the 2011 data sample [64] and (b) the 2012 data sample [65]. The full line shows the fit by the function described in the text. The dotted line shows the combinatorial background contribution. The shaded area is the contribution from partially reconstructed B decays. The dashed line shows the background from $B^{\pm} \to J/\psi\pi^{\pm}$ decays, due to the misassignment of the kaon mass to a pion.

10.2.3 Pseudorapidity regions

To take into account the variation of the inner detector momentum resolution with $|\eta|$, the selected $B^{\pm}$ candidates are separated into five regions of absolute rapidity, where rapidity is defined as:

$$y = \frac{1}{2} \ln \frac{E + p_z}{E - p_z} \tag{10.2}$$

where E is the energy of the $B^{\pm}$ and p_z is the component of its momentum in the direction of the beam axis. Table 10.2 defines the rapidity regions and gives the number of $B^{\pm}$ candidates obtained from separate fits to the invariant mass distribution in each region.

$\|y(B^{\pm}\|$ region	Number of $B^{\pm}$ candidates ($\times 10^3$)	
	2011	2012
$0 - 0.5$	56.9 ± 0.4	332 ± 1
$0.5 - 1.0$	52.7 ± 0.5	308 ± 1
$1.0 - 1.5$	39.6 ± 0.5	234 ± 1
$1.5 - 2.0$	42.1 ± 0.7	223 ± 1
$2.0 - 2.5$	11.0 ± 0.5	58 ± 2

Table 10.2: Number of signal $B^{\pm}$ candidates in the rapidity regions.

10.2.4 Sideband subtraction

Since the flavour tagging study requires only signal $B^{\pm} \to J/\psi K^{\pm}$ candidates, the background contribution must be removed. This is done by applying sideband subtraction. This method uses the assumption that the background under the signal peak can be approximated by the background contributions away from the peak region, known as sidebands. The background in the signal region can therefore be removed by subtracting an equivalent number of sideband events from the events under the signal peak.

The signal region is defined as ± 2 standard deviations (σ) from the mean (μ) of the signal Gaussian. Two sidebands are defined: the low-mass sideband and the high-mass sideband. The low-mass sideband begins 1σ below the lower edge of the signal region and is 2σ wide. The high-mass sideband begins 1σ above the upper edge of the signal region and is also 2σ wide. The background contributions in the two sidebands are summed and normalized to the background in the signal region. It is important to note that the low-mass sideband contains non-combinatorial background and is therefore somewhat different from the background under the peak, but this is found to have a negligible effect on the flavour tagging results. Based on Monte Carlo simulation, approximately 90% of the signal events are retained after the sideband subtraction is applied.

10.3 Tagging methods

10.3.1 Opposite side muon tagging

The flavour of the opposite side b quark can be determined using several different methods. The most prominent method used in ATLAS involves measuring the charge of a muon from the semileptonic decay of the opposite side B hadron. This approach provides considerable tagging power through the use of the muon detection system, which is already used in the identification of $J/\psi \to \mu^+\mu^-$ decays. One disadvantage of this method is that $b \to \mu$ transitions are diluted by transitions involving neutral B meson oscillations and cascade decays of the form $b \to c \to \mu$. These undesirable transitions produce muons with a charge opposite to those from direct $b \to \mu$ transitions, potentially contaminating the flavour measurement.

The tagging power of muon based tagging can be improved by considering additional tracks in a cone around the muon. These tracks are very likely to have come from the b quark jet and therefore provide additional information regarding the flavour of the b quark. A weighted sum of the charges of these tracks is made in the following way:

$$Q_\mu = \frac{\sum_i q^i (p_T^i)^k}{\sum_i (p_T^i)^k}. \tag{10.3}$$

where q^i and p_T^i are, respectively, the charge and transverse momentum of track i and the parameter $k = 1.1$. This value was chosen to optimize the tagging power of the algorithm. The sum is over all reconstructed tracks within a cone of $\Delta R = \sqrt{\Delta\phi^2 + \Delta\eta^2} < 0.5$ around the muon track, including the muon track itself. The signal decay products are explicitly excluded from the sum. The muon, which must be exclusive from the muons from the J/ψ decay, is required to have a transverse momentum greater than 2.5 GeV and a pseudorapidity less than 2.5. The distance δz of the point of closest approach of the muon trajectory to the primary vertex in the xy plane must be less than 5 mm. The muons are categorized based on their reconstruction classification. If the hits in the inner detector and muon spectrometer can be combined to form the muon track, the muon is classified as a "combined" muon. If the inner detector and muon spectrometer hits cannot be combined

but are matched, the muon is classified as a "segment tagged" muon. The two different muon categories are treated as separate flavour tagging methods. In the case where multiple muons are available for tagging, the one with the highest transverse momentum is used. Figures 10.2 and 10.3 shows the distribution of the opposite side muon cone charge for combined and segment tagged muons respectively in the 2011 and 2012 data samples for $B^{\pm}$ signal decays.

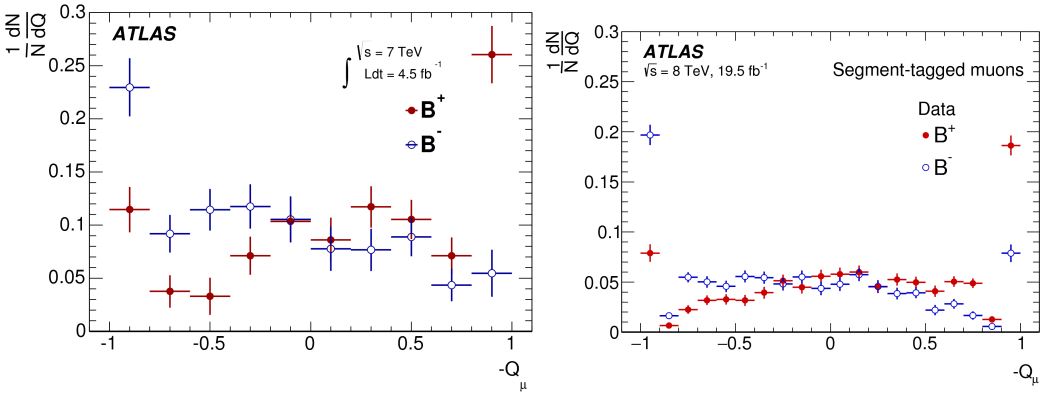

(a) (b)

Figure 10.2: Opposite side muon cone charge for segment tagged muons in (a) the 2011 data sample [64] and (b) the 2012 data sample [65].

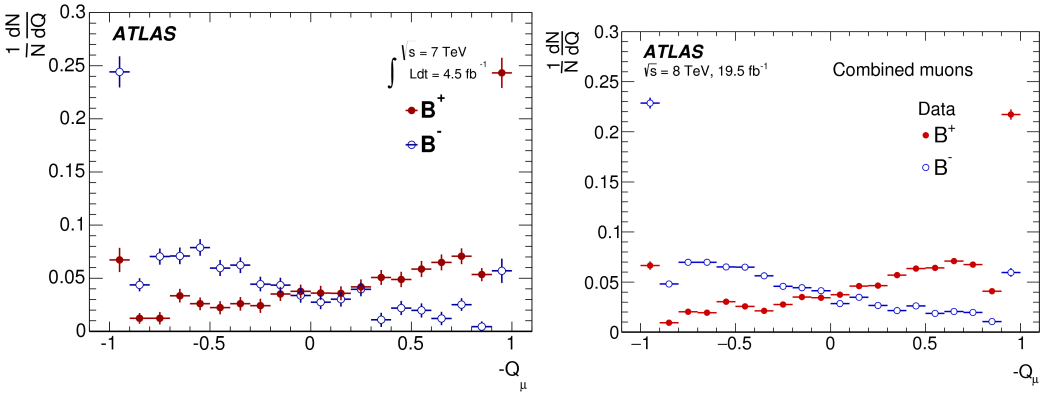

(a) (b)

Figure 10.3: Opposite side muon cone charge for combined muons in (a) the 2011 data sample [64] and (b) the 2012 data sample [65].

10.3.2 Opposite side electron tagging

In a similar way to the opposite side muon approach, the charge of an electron from the semileptonic decay of the opposite side B hadron ($b \to e$) can be utilized to identify the flavour of the signal B meson. The opposite side electron method also has the disadvantage of neutral B meson oscillations and $b \to c \to e$ cascade decays contaminating the flavour measurement with electrons of opposite charge to those from direct $b \to e$ transitions.

The variable used for opposite side electron tagging is again a weighted sum of the charges of the tracks in a cone of $\Delta R < 0.5$ around the electron, including the electron track itself:

$$Q_e = \frac{\sum_i q^i (p_T^i)^k}{\sum_i (p_T^i)^k}. \tag{10.4}$$

In this case, the value of the parameter k that maximizes the tagging power is 1.0. As for muon tagging, the decay products of the signal B meson are explicitly excluded from the sum.

To be used for tagging, the electron must have hits in both the inner detector and the EM calorimeter. It must pass the tight electron selection criteria defined in Ref. [69]. The electron track is required to have a transverse momentum greater than 0.5 GeV and a pseudorapidity less than 2.5. The distance δz of the point of closest approach of the electron trajectory to the primary vertex in the xy plane must be less than 5 mm. The electron trajectory must not be near the trajectory of the signal B meson. To this end, a requirement of $\cos \eta_b > 0.98$ is imposed, where η_b is the angle between the signal B meson and the electron in the laboratory frame. Additionally, the electron must be outside of a cone of $\Delta R = 0.4$ around the signal B meson. If more than one electron is available for tagging, the electron with the highest transverse momentum is used.

The distribution of the opposite side electron cone charge in the 2012 data sample for $B^{\pm}$ signal decays is shown in Fig. 10.4. The opposite side electron tagging method was developed for the analysis of the data taken in 2012 and was not available for the 2011 data sample.

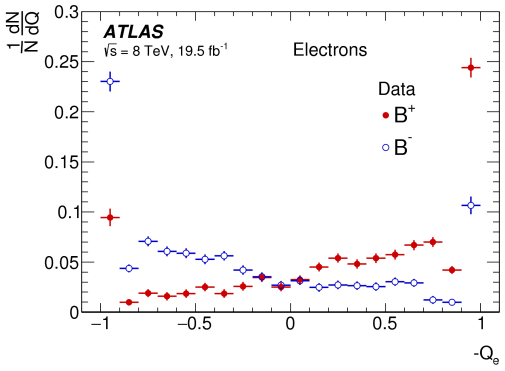

(a)

Figure 10.4: Opposite side electron cone charge in the 2012 data sample [65].

10.3.3 Jet charge tagging

In the case where no muon or electron is available for tagging, a jet produced by the opposite side b quark can be used. This type of jet is identified using several multivariate algorithms [70], and is then known as a "b-tagged jet". Each algorithm uses a likelihood ratio method for identifying b jets. For each track in the jet, a track weight W_t is produced:

$$W_t = \frac{b(S_i)}{u(S_i)}. \tag{10.5}$$

Here, $b(S_i)$ and $u(S_i)$ are probability density functions produced using hypotheses that the jet originated from, respectively, a b quark or a light quark (u, d or s). A separate function $c(S_i)$ exists for jets originating from c quarks. The b-tagged jet weight W_{Jet} is then computed by summing the logarithms of the track weights:

$$W_{Jet} = \sum_{t=1}^{N} \ln W_t \tag{10.6}$$

where N is the number of tracks in the jet. The value of W_{Jet} therefore quantifies the probability that a given jet originated from a b quark. In the analysis of the 2011 data sample, the b-tagged jet weight is required to be greater than -0.5. The requirement in the 2012 analysis is $W_{Jet} > 0.7$. These values are chosen to maximize the tagging power of the jet charge tagging

algorithm in the $B^{\pm}$ calibration sample.

The jets are reconstructed using the anti-k_T algorithm [71]. To be used for tagging, a jet must have $p_T > 500$ MeV and a cone size of $\Delta R < 0.8$. Additionally, the jet must be outside of a cone of $\Delta R = 0.5$ around the signal B meson. The jet must also be associated with the primary vertex of the signal B meson. If more than one jet passes the selection criteria, the jet with the highest value of w is used.

As for the opposite side lepton tagging methods, the variable used for jet charge tagging is a momentum weighted charge:

$$Q_J = \frac{\sum_i q^i (p_T^i)^k}{\sum_i (p_T^i)^k}. \tag{10.7}$$

where q^i is the charge of track i in the jet and p_T^i is its transverse momentum. For jet charge tagging, the total momentum p^ior the longitudinal momentum p_L^i could be used in place of p_T^i. The transverse momentum is used simply because it provides the greatest tagging power. The parameter $k = 1.1$ and this value is chosen to maximize the tagging power of the jet charge algorithm. The sum is over the tracks associated with the jet and explicitly excludes the decay products of the $B^{\pm}$ meson. This distribution of Q_J for $B^{\pm}$ signal candidates in the 2011 and 2012 data samples is shown in Fig. 10.5.

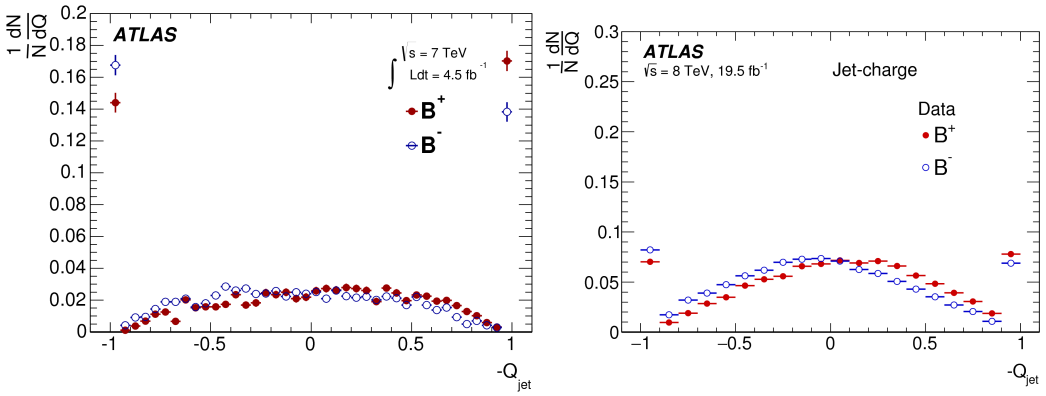

(a) (b)

Figure 10.5: Opposite side jet charge in (a) the 2011 data sample [64] and (b) the 2012 data sample [65].

10.4 Tagging performance

The performance of a given flavour tagging algorithm is quantified by the tagging power $T = \epsilon\mathcal{D}^2$, defining the effective statistical fraction of the selected data sample for which the initial flavour of the signal B meson is correctly determined. The quantity ϵ represents the efficiency, which is the fraction of the sample that has been tagged by the given algorithm. The variable $\mathcal{D}$ represents the dilution, which is the difference between the fraction of events that have been tagged correctly and the fraction that have been tagged incorrectly.

This study of the calibration sample allows the probability that the discriminating variable Q has a given value for a B^+ event or a B^- event to be determined. These probabilities are represented by $P(Q|B^+)$ and $P(Q|B^-)$ respectively. The probability that a given signal decay is tagged as containing a $\bar{b}$ quark for a specifiec value of Q is then:

$$P(B|Q) = \frac{P(Q|B^+)}{P(Q|B^+) + P(Q|B^-)}. \tag{10.8}$$

The probability that a given event is tagged as containing a B quark is:

$$P(\bar{B}|Q) = \frac{P(Q|B^-)}{P(Q|B^+) + P(Q|B^-)} = 1 - P(B|Q). \tag{10.9}$$

Using these probabilities, the tagging power of a tagging algorithm can be determined as:

$$T = \epsilon\mathcal{D}^2 = \sum_i \epsilon_i (P_i(B|Q_i) - P_i(\bar{B}|Q_i))^2 = \sum_i \epsilon_i (2P_i(B|Q_i) - 1)^2. \tag{10.10}$$

where the sum is over the bins of the probability distribution as a function of Q. The quantity ϵ_i is the number of events in bin i divided by the total number of events in the data sample. An effective value of the dilution $\mathcal{D}$ is determined from the measured efficiency and tagging power. The efficiency, dilution and tagging power of each tagging method in the 2011 and 2012 data samples are given in Tables 10.3 and 10.3 respectively.

The flavour tagging method used for a given signal B meson is chosen based on the information available in the event. The jet charge method

is defined in such a way that jet charge tagged events and events tagged leptonically do not overlap. Approximately 0.4% of events in the 2012 data sample have both muon and electron tagging available. In these events, where more than one tagging method is possible, the method with the highest tagging power is used. Events where none of the flavour tagging methods are available are assigned a probability of 0.5.

Tagging method	Efficiency [%]	Dilution [%]	Tagging power [%]
Combined muon	3.37 ± 0.04	50.6 ± 0.5	0.86 ± 0.04
Segment tagged muon	1.08 ± 0.02	36.7 ± 0.7	0.15 ± 0.02
Jet charge	27.7 ± 0.1	12.68 ± 0.06	0.45 ± 0.03
Total	32.1 ± 0.1	$21,3 \pm 0.08$	1.45 ± 0.05

Table 10.3: Tagging performance of the tagging methods used for the 2011 data sample [64]. The uncertainties are statistical only.

Tagging method	Efficiency [%]	Dilution [%]	Tagging power [%]
Combined muon	4.12 ± 0.02	47.4 ± 0.2	0.92 ± 0.02
Electron	1.19 ± 0.01	49.2 ± 0.3	0.29 ± 0.01
Segment tagged muon	1.20 ± 0.01	28.6 ± 0.2	0.10 ± 0.01
Jet charge	13.15 ± 0.03	11.85 ± 0.3	0.19 ± 0.01
Total	19.66 ± 0.04	27.56 ± 0.06	1.49 ± 0.02

Table 10.4: Tagging performance of the tagging methods used for the 2012 data sample [65]. The uncertainties are statistical only.

Chapter 11

Conclusions

The measurement of the relative width difference $\Delta\Gamma_d/\Gamma_d$ of the $B^0 - \bar{B}^0$ system is performed using data from $p-p$ collisions collected by the ATLAS experiment at $\sqrt{s} = 7$ TeV and $\sqrt{s} = 8$ TeV during Run 1 of the LHC, corresponding to an integrated luminosity of 25.2 fb^{-1}. The result is:

$$\Delta\Gamma_d/\Gamma_d = (-0.1 \pm 1.1\ (\text{stat.}) \pm 0.9\ (\text{syst.})) \times 10^{-2}.$$

This is currently the world's most precise measurement of $\Delta\Gamma_d/\Gamma_d$. It is in good agreement with the SM prediction [49] and measurements by other experiments [7, 8, 55] It is also consistent with the indirect measurement made by the D0 Collaboration [63].

The impact of the B^0 production asymmetry A_{P} on the measurement of $\Delta\Gamma_d/\Gamma_d$ is found to be negligible. This conclusion is influenced mainly by the smallness of A_{P} and the good precision of its determination, which was not necessarily evident before the measurement. The obtained value of the production asymmetry of the B^0 meson in the range $|\eta(B^0)| < 2.5$ is:

$$A_{\text{P}}(B^0) = (+0.25 \pm 0.48 \pm 0.05)\% \tag{11.1}$$

This measurement is an important by-product of this analysis. The measured value is consistent with the measurement of the LHCb collaboration [59] performed in the $2.5 < \eta(B^0) < 4.0$ range.

The technique used to measure $\Delta\Gamma_d/\Gamma_d$ developed during LHC Run 1 will form the foundation for a subsequent measurement by the ATLAS collabora-

tion using the much larger data sample expected in Run 2. This prospective measurement is anticipated to be more precise than the current world average [6] and should place constraints on possible new physics in $\Delta\Gamma_d$, such as current-current and $(\bar{d}b)(\bar{\tau}\tau)$ operators [3].

In addition to the measurement of $\Delta\Gamma_d/\Gamma_d$, the opposite side tagging methods developed primarily for use in the measurement of CP violation in $B_s^0 \to J/\psi\phi$ decays are presented. The flavour tagging algorithms were designed and calibrated using $B^\pm \to J/\psi K^\pm$ events collected by the ATLAS experiment from $p-p$ collisions during Run 1 of the LHC at $\sqrt{s} = 7$ TeV and $\sqrt{s} = 8$ TeV, which provided integrated luminosities of 4.9 fb^{-1} and 19.5 fb^{-1}, respectively. The total tagging power is measured to be $T = (1.45 \pm 0.5)\%$ at $\sqrt{s} = 7$ TeV and $T = (1.49 \pm 0.2)\%$ at $\sqrt{s} = 8$ TeV.

The $B_s^0 \to J/\psi\phi$ analysis will be continued using the data in LHC Run 2 and flavour tagging will again be required. The algorithms developed in Run 1 will provide the basis for flavour tagging in Run 2, with possible improvements coming from multi-variate analysis, which could potentially yield a significant tagging power increase.

The measurements presented in this thesis further the understanding of the properties of neutral B mesons and provide the possibility of discovering new physics phenomena involving b quarks. Although the results do not currently constrain any potential new physics, the additional data collected in future running of the LHC should provide the precision necessary to confirm of refute the Standard Model predictions.

Bibliography

[1] G. Aad *et al.* [ATLAS Collaboration], "The ATLAS Experiment at the CERN Large Hadron Collider," JINST **3** (2008) S08003. doi:10.1088/1748-0221/3/08/S08003 x, xxi, 1, 26, 28, 31, 32

[2] K. A. Olive *et al.* [Particle Data Group Collaboration], "Review of Particle Physics," Chin. Phys. C **38** (2014) 090001. ix, xxi, 2, 4, 5, 6, 9, 10, 33, 34, 49, 54, 55, 56, 62, 65, 90, 105

[3] C. Bobeth, U. Haisch, A. Lenz, B. Pecjak and G. Tetlalmatzi-Xolocotzi, "On new physics in $\Delta\Gamma_d$," JHEP **1406** (2014) 040 doi:10.1007/JHEP06(2014)040 [arXiv:1404.2531 [hep-ph]]. 2, 131

[4] T. Gershon, "$\Delta\Gamma_d$: A Forgotten Null Test of the Standard Model," J. Phys. G **38** (2011) 015007 doi:10.1088/0954-3899/38/1/015007, 10.1088/0954-3899/38/1/015007, 10.1088/0954-3899/42/11/119501 [arXiv:1007.5135 [hep-ph]]. 2

[5] V. Khachatryan *et al.* [CMS and LHCb Collaborations], "Observation of the rare $B_s^0 \to \mu^+\mu^-$ decay from the combined analysis of CMS and LHCb data," Nature **522** (2015) 68 doi:10.1038/nature14474 [arXiv:1411.4413 [hep-ex]]. 2

[6] Y. Amhis *et al.* [Heavy Flavor Averaging Group (HFAG) Collaboration], "Averages of b-hadron, c-hadron, and τ-lepton properties as of summer 2014," arXiv:1412.7515 [hep-ex]. ix, xxi, 2, 11, 49, 65, 93, 131

[7] T. Higuchi *et al.*, "Search for Time-Dependent CPT Violation in Hadronic and Semileptonic B Decays," Phys. Rev. D **85** (2012) 071105 doi:10.1103/PhysRevD.85.071105 [arXiv:1203.0930 [hep-ex]]. xxi, 2, 48, 49, 115, 130

[8] R. Aaij *et al.* [LHCb Collaboration], "Measurements of the B^+, B^0, B_s^0 meson and Λ_b^0 baryon lifetimes," JHEP **1404** (2014) 114 doi:10.1007/JHEP04(2014)114 [arXiv:1402.2554 [hep-ex]]. xxi, 2, 48, 49, 115, 130

[9] M. Aaboud *et al.* [ATLAS Collaboration], "Measurement of the relative width difference of the B^0-$\bar{B}^0$ system with the ATLAS detector," JHEP **1606** (2016) 081 doi:10.1007/JHEP06(2016)081 [arXiv:1605.07485 [hep-ex]]. 2, 48

[10] M. Skinner, "Lifetime, mixing and CPV in ATLAS", in proceedings of "16th International Conference on B-Physics at Frontier Machines" PoS(BEAUTY2016)006. 2

[11] R. Aaij *et al.* [LHCb Collaboration], "Observation of the resonant character of the $Z(4430)^-$ state," Phys. Rev. Lett. **112** (2014) no.22, 222002 doi:10.1103/PhysRevLett.112.222002 [arXiv:1404.1903 i[hep-ex]]. 4

[12] R. Aaij *et al.* [LHCb Collaboration], "Observation of $J/\psi p$ Resonances Consistent with Pentaquark States in $\Lambda_b^0 \to J/\psi K^- p$ Decays," Phys. Rev. Lett. **115** (2015) 072001 doi:10.1103/PhysRevLett.115.072001 [arXiv:1507.03414 [hep-ex]]. 4

[13] P. W. Higgs, "Broken symmetries, massless particles and gauge fields," Phys. Lett. **12** (1964) 132. doi:10.1016/0031-9163(64)91136-9. 6

[14] P. W. Higgs, "Spontaneous Symmetry Breakdown without Massless Bosons," Phys. Rev. **145** (1966) 1156. doi:10.1103/PhysRev.145.1156. 6

[15] G. Aad *et al.* [ATLAS Collaboration], "Observation of a new particle in the search for the Standard Model Higgs boson with the ATLAS detector at the LHC," Phys. Lett. B **716** (2012) 1 doi:10.1016/j.physletb.2012.08.020 [arXiv:1207.7214 [hep-ex]]. 6

[16] S. Chatrchyan *et al.* [CMS Collaboration], "Observation of a new boson at a mass of 125 GeV with the CMS experiment at the LHC," Phys. Lett. B **716** (2012) 30 doi:10.1016/j.physletb.2012.08.021 [arXiv:1207.7235 [hep-ex]]. 6

[17] T. D. Lee and C. N. Yang, "Question of Parity Conservation in Weak Interactions," Phys. Rev. **104** (1956) 254. doi:10.1103/PhysRev.104.254. 6

[18] L. D. Landau, "On the conservation laws for weak interactions," Nucl. Phys. **3** (1957) 127. doi:10.1016/0029-5582(57)90061-5. 7

[19] J. H. Christenson, J. W. Cronin, V. L. Fitch and R. Turlay, "Evidence for the 2 pi Decay of the k(2)0 Meson," Phys. Rev. Lett. **13** (1964) 138. doi:10.1103/PhysRevLett.13.138. 7

[20] B. Aubert *et al.* [BaBar Collaboration], "Observation of CP violation in the B^0 meson system," Phys. Rev. Lett. **87** (2001) 091801 doi:10.1103/PhysRevLett.87.091801 [hep-ex/0107013]. 7

[21] K. Abe *et al.* [Belle Collaboration], "Observation of large CP violation in the neutral B meson system," Phys. Rev. Lett. **87** (2001) 091802 doi:10.1103/PhysRevLett.87.091802 [hep-ex/0107061]. 7

[22] N. Cabibbo, "Unitary Symmetry and Leptonic Decays," Phys. Rev. Lett. **10** (1963) 531. doi:10.1103/PhysRevLett.10.531. 7

[23] M. Kobayashi and T. Maskawa, "CP Violation in the Renormalizable Theory of Weak Interaction," Prog. Theor. Phys. **49** (1973) 652. doi:10.1143/PTP.49.652. 7

[24] A. Pich, "The Standard Model of Electroweak Interactions," arXiv:1201.0537 [hep-ph]. ix, 8

[25] L. Wolfenstein, "Parametrization of the Kobayashi-Maskawa Matrix," Phys. Rev. Lett. **51** (1983) 1945. doi:10.1103/PhysRevLett.51.1945. 8

[26] R. Fleischer, "Flavour Physics and CP Violation: Expecting the LHC," arXiv:0802.2882 [hep-ph]. ix, 12, 17, 18

[27] I. Dunietz, R. Fleischer and U. Nierste, "In pursuit of new physics with B_s decays," Phys. Rev. D **63** (2001) 114015 doi:10.1103/PhysRevD.63.114015 [hep-ph/0012219]. 17

[28] O. S. Bruning, P. Collier, P. Lebrun, S. Myers, R. Ostojic, J. Poole and P. Proudlock, "LHC Design Report Vol.1: The LHC Main Ring," CERN-2004-003-V1, CERN-2004-003, CERN-2004-003-V-1. 20, 21

[29] L. Evans and P. Bryant, "LHC Machine," JINST **3** (2008) S08001. doi:10.1088/1748-0221/3/08/S08001. 20, 21

[30] S. Catani, "Qcd," In *Geneva 1999, Standard model physics (and more) at the LHC* 1-115 [hep-ph/0005025]. ix, 24

[31] K. Grimm*et al.*, "Reconstruction of primary vertices at the ATLAS experiment in Run 1 proton-proton collisions at the LHC," ATL-COM-PHYS-2016-263 CERN, Geneva, 2016. xxi, 25

[32] The official ATLAS public photographs and images website, ix, x, 21, 22, 27, 30, 33, 35
http://atlas.ch/photos/index.html.

[33] ATLAS luminosity public results, ix, 23
https://twiki.cern.ch/twiki/bin/view/AtlasPublic/LuminosityPublicResults.

[34] A. Airapetian *et al.* [ATLAS Collaboration], "ATLAS: Detector and physics performance technical design report. Volume 1," CERN-LHCC-99-14, ATLAS-TDR-14. x, 37

[35] G. Duckeck *et al.* [ATLAS Collaboration], "ATLAS computing: Technical design report," CERN-LHCC-2005-022, ATLAS-TRD-017. 39

[36] I. Foster, C. Kesselman "Computational Grids," *Chapter 2 of "The Grid: Blueprint for a New Computing Infrastructure"*, Morgan-Kaufman, 1999. 39

[37] R. Brun and F. Rademakers, "ROOT: An object oriented data analysis framework," Nucl. Instrum. Meth. A **389** (1997) 81. doi:10.1016/S0168-9002(97)00048-X. 40

[38] M. Branco *et al.* [ATLAS Collaboration], "Managing ATLAS data on a petabyte-scale with DQ2," J. Phys. Conf. Ser. **119** (2008) 062017. doi:10.1088/1742-6596/119/6/062017. 41

[39] The official Rucio documentation. 41
rucio.cern.ch.

[40] F. Brochu *et al.* "Ganga: a tool for computational-task management and easy access to Grid resources," arXiv:0902.2685 [hep-ph] doi:10.1016/j.cpc.2009.06.016. 42

[41] A. Klimentov, P. Nevski, M. Potekhin and T. Wenaus, "The ATLAS PanDA monitoring system and its evolution," J. Phys. Conf. Ser. **331** (2011) 072058. doi:10.1088/1742-6596/331/7/072058. 42

[42] G. Aad *et al.* [ATLAS Collaboration], "The ATLAS Simulation Infrastructure," Eur. Phys. J. C **70** (2010) 823 doi:10.1140/epjc/s10052-010-1429-9 [arXiv:1005.4568 [physics.ins-det]]. x, 42

[43] G. Barrand *et al.*, "GAUDI - A software architecture and framework for building HEP data processing applications," Comput. Phys. Commun. **140** (2001) 45. doi:10.1016/S0010-4655(01)00254-5. 43

[44] T. Sjostrand, S. Mrenna and P. Z. Skands, "PYTHIA 6.4 Physics and Manual," JHEP **0605** (2006) 026 doi:10.1088/1126-6708/2006/05/026 [hep-ph/0603175]. 43

[45] M. Smizanska, "PythiaB an interface to Pythia6 dedicated to simulation of beauty events," ATL-COM-PHYS-2003-038, CERN, Geneva, 2003. 44

[46] T. Sjostrand, S. Mrenna and P. Z. Skands, "A Brief Introduction to PYTHIA 8.1," Comput. Phys. Commun. **178** (2008) 852 doi:10.1016/j.cpc.2008.01.036 [arXiv:0710.3820 [hep-ph]]. 44

[47] S. Agostinelli *et al.* [GEANT4 Collaboration], "GEANT4: A Simulation toolkit," Nucl. Instrum. Meth. A **506** (2003) 250. doi:10.1016/S0168-9002(03)01368-8. 44

[48] C. Anastopoulos *et al.* "Physics analysis tools for beauty physics in ATLAS," Journal of Physics: Conference Series **119** (2008) 032003. doi:10.1016/S0168-9002(97)00048-X. 46

[49] A. Lenz and U. Nierste, "Numerical Updates of Lifetimes and Mixing Parameters of B Mesons," arXiv:1102.4274 [hep-ph]. 48, 115, 130

[50] M. Ciuchini, E. Franco, V. Lubicz, F. Mescia and C. Tarantino, "Lifetime differences and CP violation parameters of neutral B mesons at the next-to-leading order in QCD," JHEP **0308** (2003) 031 doi:10.1088/1126-6708/2003/08/031 [hep-ph/0308029]. 48

[51] M. Beneke, G. Buchalla, A. Lenz and U. Nierste, "CP asymmetry in flavor specific B decays beyond leading logarithms," Phys. Lett. B **576** (2003) 173 doi:10.1016/j.physletb.2003.09.089 [hep-ph/0307344]. 48

[52] A. Lenz and U. Nierste, "Theoretical update of $B_s - \bar{B}_s$ mixing," JHEP **0706** (2007) 072 doi:10.1088/1126-6708/2007/06/072 [hep-ph/0612167]. 48

[53] B. Aubert *et al.* [BaBar Collaboration], "Limits on the decay rate difference of neutral$-B$ mesons and on CP, T, and CPT violation in $B^0\overline{B}^0$ oscillations," Phys. Rev. D **70** (2004) 012007 doi:10.1103/PhysRevD.70.012007 [hep-ex/0403002]. xxi, 49

[54] B. Aubert *et al.* [BaBar Collaboration], "Study of $B \to D_{sJ}^{(*)+}\bar{D}^{(*)}$ decays," Phys. Rev. Lett. **93** (2004) 181801 doi:10.1103/PhysRevLett.93.181801 [hep-ex/0408041]. 49

[55] B. Aubert *et al.* [BaBar Collaboration], "Limits on the decay rate difference of neutral$-B$ mesons and on CP, T, and CPT violation in $B^0\overline{B}^0$ oscillations," Phys. Rev. D **70** (2004) 012007 doi:10.1103/PhysRevD.70.012007 [hep-ex/0403002]. 49, 115, 130

[56] V. Kostyukhin *et al.*, "VKalVrt - package for vertex reconstruction in ATLAS," ATL-PHYS-2003-031 CERN, Geneva, 2003. 53

[57] E. Norrbin and R. Vogt, "Bottom production asymmetries at the LHC," hep-ph/0003056. 89

[58] E. Norrbin and T. Sjostrand, "Production and hadronization of heavy quarks," Eur. Phys. J. C **17** (2000) 137 doi:10.1007/s100520000460 [hep-ph/0005110]. 89

[59] R. Aaij *et al.* [LHCb Collaboration], "Measurement of the $\bar{B}^0 - B^0$ and $\bar{B}_s^0 - B_s^0$ production asymmetries in pp collisions at $\sqrt{s} = 7$ TeV," Phys. Lett. B **739** (2014) 218 doi:10.1016/j.physletb.2014.10.005 [arXiv:1408.0275 [hep-ex]]. 89, 93, 130

[60] R. Aaij *et al.* [LHCb Collaboration], "Measurement of the effective $B_s^0 \to J/\psi K_S^0$ lifetime," Nucl. Phys. B **873** (2013) 275 doi:10.1016/j.nuclphysb.2013.04.021 [arXiv:1304.4500 [hep-ex]]. 110

[61] D. Acosta *et al.* [CDF Collaboration], "Measurement of the lifetime difference between B_s mass eigenstates," Phys. Rev. Lett. **94** (2005) 101803 doi:10.1103/PhysRevLett.94.101803 [hep-ex/0412057]. xix, 112, 114

[62] R. Aaij *et al.* [LHCb Collaboration], "Measurement of the polarization amplitudes in $B^0 \to J/\psi K^*(892)^0$ decays," Phys. Rev. D **88** (2013) 052002 doi:10.1103/PhysRevD.88.052002 [arXiv:1307.2782 [hep-ex]]. 112

[63] V. M. Abazov *et al.* [D0 Collaboration], "Study of CP -violating charge asymmetries of single muons and like-sign dimuons in pp collisions," Phys. Rev. D **89** (2014) no.1, 012002 doi:10.1103/PhysRevD.89.012002 [arXiv:1310.0447 [hep-ex]]. 115, 130

[64] G. Aad *et al.* [ATLAS Collaboration], "Flavor tagged time-dependent angular analysis of the $B_s \to J/\psi\phi$ decay and extraction of $\Delta\Gamma$s and the weak phase ϕ_s in ATLAS," Phys. Rev. D **90** (2014) no.5, 052007 doi:10.1103/PhysRevD.90.052007 [arXiv:1407.1796 [hep-ex]]. xix, xx, xxiii, 116, 117, 120, 123, 126, 129

[65] G. Aad *et al.* [ATLAS Collaboration], "Measurement of the CP-violating phase ϕ_s and the B_s^0 meson decay width difference with $B_s^0 \to J/\psi\phi$ decays in ATLAS," arXiv:1601.03297 [hep-ex]. xix, xx, xxiii, 116, 120, 123, 125, 126, 129

[66] J. Charles *et al.*, "Predictions of selected flavour observables within the Standard Model," Phys. Rev. D **84** (2011) 033005 doi:10.1103/PhysRevD.84.033005 [arXiv:1106.4041 [hep-ph]]. 116

[67] R. Aaij *et al.* [LHCb Collaboration], "Precision measurement of CP violation in $B_s^0 \to J/\psi K^+K^-$ decays," Phys. Rev. Lett. **114** (2015) no.4, 041801 doi:10.1103/PhysRevLett.114.041801 [arXiv:1411.3104 [hep-ex]]. 116

[68] V. Khachatryan *et al.* [CMS Collaboration], "Measurement of the CP-violating weak phase ϕ_s and the decay width difference $\Delta\Gamma_s$ using the $\mathrm{B}_s^0 \to J/\psi\phi(1020)$ decay channel in pp collisions at $\sqrt{s} = 8$ TeV," Phys. Lett. B **757** (2016) 97 doi:10.1016/j.physletb.2016.03.046 [arXiv:1507.07527 [hep-ex]]. 116

[69] G. Aad *et al.* [ATLAS Collaboration], "Electron performance measurements with the ATLAS detector using the 2010 LHC proton-proton collision

data," Eur. Phys. J. C **72** (2012) 1909 doi:10.1140/epjc/s10052-012-1909-1 [arXiv:1110.3174 [hep-ex]]. 124

[70] G. Aad *et al.* [ATLAS Collaboration], "Expected Performance of the ATLAS Experiment - Detector, Trigger and Physics," arXiv:0901.0512 [hep-ex]. 125

[71] M. Cacciari, G. P. Salam and G. Soyez, "The Anti-k(t) jet clustering algorithm," JHEP **0804** (2008) 063 doi:10.1088/1126-6708/2008/04/063 [arXiv:0802.1189 [hep-ph]]. 126

Appendices

Appendix A

Data sets used for the measurement of $\Delta\Gamma_d/\Gamma_d$

The data sets used in the analysis are

```
data11_7TeV.period%.physics_Muons.PhysCont.DAOD_ONIAMUMU.pro10_v01
data12_8TeV.periodB.physics_Bphysics.PhysCont.DAOD_JPSIMUMU.grp14_v03_p1425
data12_8TeV.periodC.physics_Bphysics.PhysCont.DAOD_JPSIMUMU.grp14_v04_p1425
data12_8TeV.periodD.physics_Bphysics.PhysCont.DAOD_JPSIMUMU.grp14_v04_p1425
data12_8TeV.periodE.physics_Bphysics.PhysCont.DAOD_JPSIMUMU.grp14_v03_p1425
data12_8TeV.periodG.physics_Bphysics.PhysCont.DAOD_JPSIMUMU.grp14_v03_p1425
data12_8TeV.periodH.physics_Bphysics.PhysCont.DAOD_JPSIMUMU.grp14_v04_p1425
data12_8TeV.periodI.physics_Bphysics.PhysCont.DAOD_JPSIMUMU.grp14_v03_p1425
data12_8TeV.periodJ.physics_Bphysics.PhysCont.DAOD_JPSIMUMU.grp14_v03_p1425
data12_8TeV.periodL.physics_Bphysics.PhysCont.DAOD_JPSIMUMU.grp14_v03_p1425
```

The Good Run Lists for the two data periods are

```
data11_7TeV.periodAllYear_DetStatus-v60-pro10-02_DQDefects-00-01-00_PHYS_CombinedPerf_Muon_Muon.xml
data12_8TeV.periodAllYear_DetStatus-v61-pro14-02_DQDefects-00-01-00_PHYS_StandardGRL_All_Good.xml
```

The Good Run Lists define the luminosity blocks, which typically correspond to about two minutes of data taking, that are considered "good" for physics analysis. There are a number of reasons why a particular luminosity block may considered not to be "good" such as:

- The LHC not being in stable-beam mode.
- The ATLAS magnet system being off or ramping up.
- One or more of the sub-detectors being off.
- Too many noisy cells in the detector.

The Monte Carlo samples used in this analysis are summarised in Table A.1.

MC campaign	Sample	Dataset number	Tag	No. of events
MC11	$B^0 \to J/\psi K^{*0}$	108524	e1039_a131_s1353_a178_r2993	500 k
	$B^0 \to J/\psi K^{*0}$	108570	e1131_a131_s1353_a178_r2993	500 k
	$B^0 \to J/\psi K_S$	108508	e1108_a131_s1353_a178_r2993	1 M
	$B^0 \to J/\psi K_S$	108509	e995_a131_s1353_a178_r2993	500 k
MC12	$B^0 \to J/\psi K^{*0}$	208417	e2376_a159_a180_r3549	12 M
	$\bar{B}^0 \to J/\psi \bar{K}^{*0}$	208444	e3793_a188_a272_r4516	12 M
	$B^0 \to J/\psi K_S$	208412	e2324_a159_a180_r3549	20 M

Table A.1: MC samples used in the analysis.

Appendix B

Data sets used for flavour tagging

The data sets used in the 2011 analysis are:

```
data11_7TeV.periodB2.physics_Muons.PhysCont.DAOD_ONIAMUMU.repro09_v01
data11_7TeV.periodD.physics_Muons.PhysCont.DAOD_ONIAMUMU.repro09_v01
data11_7TeV.periodE.physics_Muons.PhysCont.DAOD_ONIAMUMU.repro09_v01
data11_7TeV.periodF2.physics_Muons.PhysCont.DAOD_ONIAMUMU.repro09_v01
data11_7TeV.periodF3.physics_Muons.PhysCont.DAOD_ONIAMUMU.repro09_v01
data11_7TeV.periodG.physics_Muons.PhysCont.DAOD_ONIAMUMU.repro09_v01
data11_7TeV.periodH.physics_Muons.PhysCont.DAOD_ONIAMUMU.repro09_v01
data11_7TeV.periodI.physics_Muons.PhysCont.DAOD_ONIAMUMU.repro09_v01
data11_7TeV.periodJ.physics_Muons.PhysCont.DAOD_ONIAMUMU.repro09_v01
data11_7TeV.periodK1.physics_Muons.PhysCont.DAOD_ONIAMUMU.repro09_v01
data11_7TeV.periodK2.physics_Muons.PhysCont.DAOD_ONIAMUMU.repro09_v01
data11_7TeV.periodK3.physics_Muons.PhysCont.DAOD_ONIAMUMU.repro09_v01
data11_7TeV.periodK4.physics_Muons.PhysCont.DAOD_ONIAMUMU.repro09_v01
data11_7TeV.periodL.physics_Muons.PhysCont.DAOD_ONIAMUMU.t0pro09_v01
data11_7TeV.periodM2.physics_Muons.PhysCont.DAOD_ONIAMUMU.t0pro09_v01
data11_7TeV.periodM4.physics_Muons.PhysCont.DAOD_ONIAMUMU.t0pro09_v01
data11_7TeV.periodM5.physics_Muons.PhysCont.AOD.t0pro09_v01
data11_7TeV.periodM6.physics_Muons.PhysCont.DAOD_ONIAMUMU.t0pro09_v01
data11_7TeV.periodM8.physics_Muons.PhysCont.AOD.t0pro09_v01
data11_7TeV.periodM10.physics_Muons.PhysCont.AOD.t0pro09_v01
```

The data sets used in the 2012 analysis are:

```
data12_8TeV.periodB.physics_Bphysics.PhysCont.DAOD_JPSIMUMU.grp14_v03_p1425
data12_8TeV.periodC.physics_Bphysics.PhysCont.DAOD_JPSIMUMU.grp14_v04_p1425
data12_8TeV.periodE.physics_Bphysics.PhysCont.DAOD_JPSIMUMU.grp14_v03_p1425
data12_8TeV.periodF.physics_Bphysics.PhysCont.DAOD_JPSIMUMU.grp14_v03_p1425
data12_8TeV.periodG.physics_Bphysics.PhysCont.DAOD_JPSIMUMU.grp14_v03_p1425
data12_8TeV.periodH.physics_Bphysics.PhysCont.DAOD_JPSIMUMU.grp14_v04_p1425
data12_8TeV.periodI.physics_Bphysics.PhysCont.DAOD_JPSIMUMU.grp14_v03_p1425
data12_8TeV.periodJ.physics_Bphysics.PhysCont.DAOD_JPSIMUMU.grp14_v03_p1425
data12_8TeV.periodL.physics_Bphysics.PhysCont.DAOD_JPSIMUMU.grp14_v03_p1425
```

The Good Run List applied to this data sample was:

`data12_8TeV.periodAllYear_DetStatus-v61-pro14-02_DQDefects-503-00-01-00_PHYS_StandardGRL_All_Good.xml`